

Roman Zvahelskyi

On In-situ Imaging for 3D Laser Microprinting

**2024
Dissertation**

ON IN-SITU IMAGING FOR 3D LASER MICROPRINTING

Zur Erlangung des akademischen Grades eines
DOKTORS DER NATURWISSENSCHAFTEN (Dr. rer. nat.)
von der KIT-Fakultät für Physik des
Karlsruher Instituts für Technologie (KIT)

genehmigte

DISSERTATION

von

MSc. Roman Zvahelskyi
geboren in Simferopol

Tag der mündlichen Prüfung: 05.07.2024

Referent: Prof. Dr. Martin Wegener

Korreferent: Prof. Dr. Carsten Rockstuhl

CONTENTS

PUBLICATIONS	1
1 INTRODUCTION	3
2 FUNDAMENTALS OF 3D LASER MICROPRINTING	7
2.1 Concept of 3D laser Microprinting	8
2.1.1 Principle	8
2.1.2 Feature Size	9
2.1.3 Threshold and Accumulation Models	10
2.1.4 Important Properties of Photoresists and Polymers	13
2.2 Printing Strategies	14
2.3 Experimental Printing Setup	15
3 IN-SITU IMAGING METHODS FOR 3D LASER MICROPRINTING	19
3.1 Typical Characterization of Printed Samples	20
3.2 In-situ Imaging and Possible Solutions	21
3.3 Optical Coherence Tomography	22
3.3.1 Applicability	22
3.3.2 Principle	23
3.3.3 Interference Signal	25
3.4 Bright-field Optical Microscopy	28
3.5 Quantitative Phase Imaging	30
3.5.1 Phase Imaging	30
3.5.2 Digital Holographic Microscopy	31
3.5.3 Transport-of-intensity Equation	33
3.5.4 Optical Diffraction Tomography	35
4 IN-SITU OPTICAL COHERENCE TOMOGRAPHY (OCT)	39
4.1 Experimental Setup	40
4.1.1 Design and Description	40
4.1.2 Workflow	43

4.1.3	Validation	44
4.2	Inspection of Plain Photoresist	46
4.3	Inspection of Planar Surfaces	47
4.3.1	Polymer-substrate Interface	48
4.3.2	Polymer-photoresist Interface	50
4.3.3	In-situ Thickness Calculation	55
4.3.4	Shrinkage measurements	56
4.4	Inspection of 3D-printed Geometries	57
4.5	Conclusion	62
5	IN-SITU QUANTITATIVE PHASE IMAGING (QPI)	65
5.1	QPI Integration Principle	66
5.1.1	Introduction	66
5.1.2	QPI Modification of the Laser Printer	66
5.1.3	Phase Retrieval Algorithm	67
5.1.4	Workflow	69
5.2	Refractive Index and Shrinkage Determination	70
5.2.1	Determination Procedure	71
5.2.2	Cuboid Array	72
5.3	Topography of Printed Micro-optics	75
5.3.1	Micro-lens	75
5.3.2	Diffraction Optical Elements	77
5.3.3	Phase Plate	79
5.4	Conclusion	80
6	IN-SITU TOMOGRAPHIC RECONSTRUCTION VIA DEEP LEARNING	83
6.1	Inverse Problem for In-situ Imaging	84
6.2	End-to-end Deep Learning Approach	85
6.3	Ground Truth Simulations	87
6.3.1	3D Object Generation	87
6.3.2	Refractive Index Assignment	89
6.3.3	Intensity Simulations	90
6.3.4	Post-processing	93
6.4	3D U-Net Training and Testing	94
6.4.1	Training	94
6.4.2	Testing	96

6.5	Experimental Validation	99
6.5.1	Image Capture	99
6.5.2	Image Processing	100
6.5.3	Experimental Reconstructions	101
6.6	Stability and Robustness	103
6.7	Conclusion	106
7	CONCLUSIONS AND OUTLOOK	109
A	APPENDIX	115
A.1	Generation of a Batch Group Consisting of 8 Batches	115
A.2	Simulation of Intensities Using Modified Multi-slice Beam Propagation Model (m-MSBPM)	116
A.3	3D U-Net Architecture	117
	BIBLIOGRAPHY	119
	ACKNOWLEDGMENTS	133

PUBLICATIONS

PARTS OF THIS THESIS HAVE ALREADY BEEN PUBLISHED . . .

. . . in scientific journals:

- R. Zvagelsky, F. Mayer, D. Beutel, C. Rockstuhl, G. Gomard, and M. Wegener, “Towards in-situ diagnostics of multi-photon 3d laser printing using optical coherence tomography”, *Light: Advanced Manufacturing* **3**, 466–480 (2022)
- R. Zvagelsky, P. Kiefer, J. Weinacker, and M. Wegener, “In-situ quantitative phase imaging during multi-photon laser printing”, *ACS Photonics* **10**, 2901–2908 (2023)
- R. Zvagelsky, T. Alletzhäusser, S. Kalt, and M. Wegener, “In-situ optical tomographic reconstruction during 3d laser microprinting using deep learning”, *Nature Communications* (under review)

. . . in patent applications:

- G. Gomard, B. Borrmann, M. Hillenbrand, T. Michael, R. Zvahelskyi, F. Mayer, and M. Wegener, “3d printing apparatus and 3d printing method for manufacturing a workpiece”, European pat. WO2023165774A1 (Sept. 7, 2023)

. . . at scientific conferences (only own presentations):

- R. Zvahelskyi, F. Mayer, D. Beutel, C. Rockstuhl, G. Gomard, and M. Wegener, “Optical coherence tomography for multi-photon 3d laser printing: towards in-situ imaging and quality control”, oral talk, SPIE Photonics West (San Francisco, California, USA), Jan. 31, 2023
- R. Zvahelskyi, T. Alletzhäusser, P. Kiefer, J. Weinacker, and M. Wegener, “In-situ shape monitoring during multi-photon 3d laser printing”, invited talk, SPIE Photonics West (San Francisco, California, USA), Jan. 30, 2024

ADDITIONAL RELATED WORK HAS ALREADY BEEN PUBLISHED . . .

. . . in scientific journals:

- T. Li, M. Kahnt, T. L. Sheppard, R. Yang, K. V. Falch, R. Zvagelsky, P. Villanueva-Perez, M. Wegener, and M. Lyubomirskiy, "X-ray multibeam ptychography at up to 20 keV: nano-lithography enhances x-ray nano-imaging", *Advanced Science*, 2310075 (2024)
- S. Braun, R. Zvagelsky, T. Messer, M. Holsten, P. Kollenz, O. Tverskoy, A. De la Cruz Garcia, C. Selhuber-Unkel, M. Mastalerz, F. Rominger, J. Freudenberg, M. Wegener, and U. Bunz, "Vinylcyclopropane polymerization by 3D laser nanoprinting: low shrinkage resins with low cytotoxicity", *Macromolecules* (under review)

1 INTRODUCTION

What do Galileo's discovery of Jupiter's moons, Darwin's theory of natural selection, and Newton's demonstration of dispersion have in common?

They were all achieved through in-situ observations. In-situ observation, which involves examining phenomena in their natural or original context, enables the study of systems without altering their original state. Galileo's telescopic observations reshaped our understanding of space. Darwin's meticulous observations aboard the HMS Beagle provided critical evidence for natural selection, revolutionizing biology. Similarly, Newton's prism experiments deepened our comprehension of light and color, laying the foundational principles of optics. These milestones highlight how in-situ observation and exploration can advance knowledge and challenge existing ideas.

Today, traditional in-situ observations have evolved into advanced digital in-situ imaging and reconstruction techniques, providing valuable information across numerous fields. In medicine, sophisticated imaging techniques such as magnetic resonance imaging (MRI) and X-ray computed tomography scans offer detailed visualizations of internal structures, significantly enhancing diagnosis and treatment [1–4]. Environmental science uses sensors and drones to gather real-time data on air and water quality, wildlife, and vegetation, which is crucial for understanding ecosystems and addressing climate change [5–8]. Similarly, in computer science, techniques such as machine vision and image recognition are key for advancements in fields like autonomous vehicles and robotics, enabling machines to interpret and respond to visual data on the fly [9, 10].

In-situ imaging and reconstruction play a crucial role in additive manufacturing [11]. Accessing the morphology and properties of the fabricated structure online, during the fabrication process, or immediately after, enables much faster optimization of the specimen's shape and significantly facilitates the entire manufacturing process. For example, NASA engineers routinely use thermal nondestructive evaluation during a deposition for in-situ characterization of fabricated parts for

aerospace applications [12]. In biofabrication, particularly in tissue engineering, in-situ imaging and reconstruction are essential for monitoring the growth and development of engineered tissues. By employing different microscopic techniques, researchers can observe cellular behavior and tissue formation in real time [13, 14].

This thesis explores possibilities of the implementation of in-situ imaging techniques specifically in 3D laser microprinting. Since its development in the 1990s, laser printing has become a leading technique in 3D micro- and nanofabrication [15]. However, printing results are typically characterized in an ex-situ manner, meaning the sample has to be removed from the printing device, developed, and inspected using a separate imaging instrument. The lack of in-situ imaging, which could allow users to access printed parts during or immediately after printing, makes the printing process virtually blind. Ex-situ imaging of printed specimens significantly slows the further advancement of 3D laser printing technology and hinders industrial adoption due to the need for quality control at all stages.

Along these lines, I present three developed methods for in-situ monitoring during and immediately after 3D laser microprinting:

- Optical coherence tomography (OCT) for in-situ detection of back-scattering properties of 3D-printed specimens.
- Quantitative phase imaging (QPI) for measuring in-situ topography maps of printed micro-optics and 2.5D structures.
- End-to-end deep learning approach for in-situ optical reconstruction of 3D-printed samples.

Both OCT and QPI are well-known imaging techniques that are widely used, especially in bioimaging applications [16, 17]. These methods were adapted for in-situ imaging and reconstruction of laser-printed specimens. Particularly, the OCT experimental setup, mimicking in-situ imaging conditions was designed and assembled from scratch. The QPI method was directly integrated into a 3D laser printer enabling rapid in-situ phase retrieval of printed specimens. The proposed deep learning reconstruction approach is uniquely developed to solve the specific inverse scattering problem arising in in-situ microscopic imaging.

OUTLINE OF THIS THESIS

In [chapter 2](#), I will describe the essential aspects of 3D laser microprinting necessary for understanding this work. This includes the main principles and workflow of the printing process as well as threshold and accumulation models for explaining the photochemistry of photoresists. I will also discuss the primary printing

strategies and the experimental printing setup used throughout this work.

[chapter 3](#) describes typical ex-situ characterization methods for 3D-printed specimens and introduces the definitions and main criteria for in-situ imaging in 3D laser microprinting. I will then discuss the theory behind the main methods developed in this work and those realized by other authors. For each method, I will provide information on its applicability to in-situ imaging

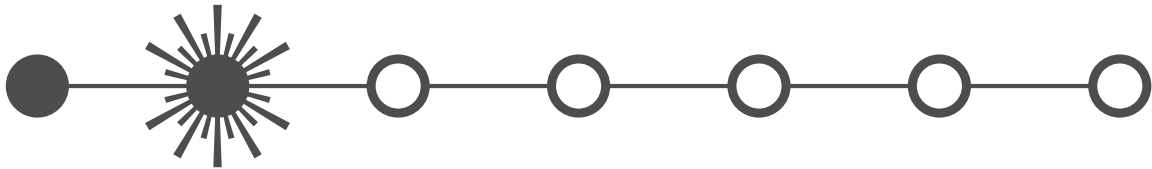
[chapter 4](#) presents the concept and experimental realization of in-situ optical coherence tomography. I will begin by describing the experimental setup that simulates in-situ imaging conditions for measuring 3D-printed laser specimens. I will then present the experimental results, which include inspecting photoresist inhomogeneity before printing, determining refractive index and shrinkage dependencies on writing parameters, exploring the scattering properties of printed specimens, and reconstructing 3D-printed samples based on their scattering imperfections.

[chapter 5](#) details the integration of in-situ quantitative phase imaging into a commercial laser printer. This integration will be achieved using the well-known transport-of-intensity equation, which retrieves the phase information of printed structures from their in-situ defocused optical microscopy images. Through in-situ phase imaging, accurate topography maps of printed micro-optical elements will be obtained and analyzed.

In [chapter 6](#), I will describe the combination of bright-field optical microscopy with advanced deep learning techniques to solve the inverse scattering problem and reconstruct the binarized refractive index of 3D-printed samples. The experimental validation of the developed 3D reconstruction approach and its robustness and stability will be discussed at the end of this chapter.

Finally, I will summarize the results of this thesis and give an outlook on future developments in [chapter 7](#).

2 FUNDAMENTALS OF 3D LASER MICROPRINTING



In this chapter, I will explain the principles of 3D laser microprinting. I will present the threshold and accumulation models that are typically used to understand the photopolymerization processes occurring in 3D laser microprinting. Subsequently, I will detail the important properties of the applied photoresists and the resulting polymer structures. At the end of the chapter, the typical printing strategies and experimental printing setup will be described.

2.1 CONCEPT OF 3D LASER MICROPRINTING

3D laser microprinting is the primary optical technology capable of fabricating three-dimensional micro- and submicron-structures down to the 100 nm scale [18]. Emerging in the 1990s [19, 20], this technology has advanced significantly, evolving into a versatile high-resolution 3D fabrication tool for a wide range of applications across various fields. Among its numerous applications are free-form designed micro-lenses [21–23] and diffractive optical elements [24–26] for any kind of beam shaping, micro-robots capable of controlled swimming and cargo transport [27, 28], 3D interconnections that function as photonic wires and couplers [29, 30], and microstructures that control and guide cellular systems [31, 32].

In the following, important aspects of 3D laser microprinting necessary for the scope of this work, will be discussed. These include the main principle, minimum feature size and resolution, the photochemistry of photoresists as well as the properties of photoresists and polymerized structures.

2.1.1 Principle

3D laser microprinting operates on the principles of multi-photon polymerization, where focused, typically femtosecond-pulsed, laser radiation induces localized polymerization reactions in photosensitive resins, known as photoresists [15]. The necessity of using multi-photon processes is crucial for high-resolution 3D printing and will be further discussed from the accumulation model perspective in [subsection 2.1.3](#).

The principle of 3D laser microprinting is depicted in [Figure 2.1](#). Laser radiation is focused through a high-numerical-aperture objective lens into a photoresist volume, a droplet of which was previously deposited on the substrate. In the vicinity of the laser focus, a photochemical reaction of polymerization is initiated, producing a confined polymer volumetric element in the shape of an ellipsoid, typically referred to as the printing voxel. By steering the laser beam, more voxels at different positions are introduced, and polymerized lines are fabricated. If a user moves the laser beam in the axial direction by, e.g., adjusting a motorized z-stage, complex 3D trajectories can be produced. Typically, 3D structures are printed in a slice-by-slice manner, where a specimen is fabricated starting from the substrate-photoresist interface. After the structure is printed, the liquid photoresist is washed away during the development process using, for example, acetone, leaving only the solid polymerized parts.

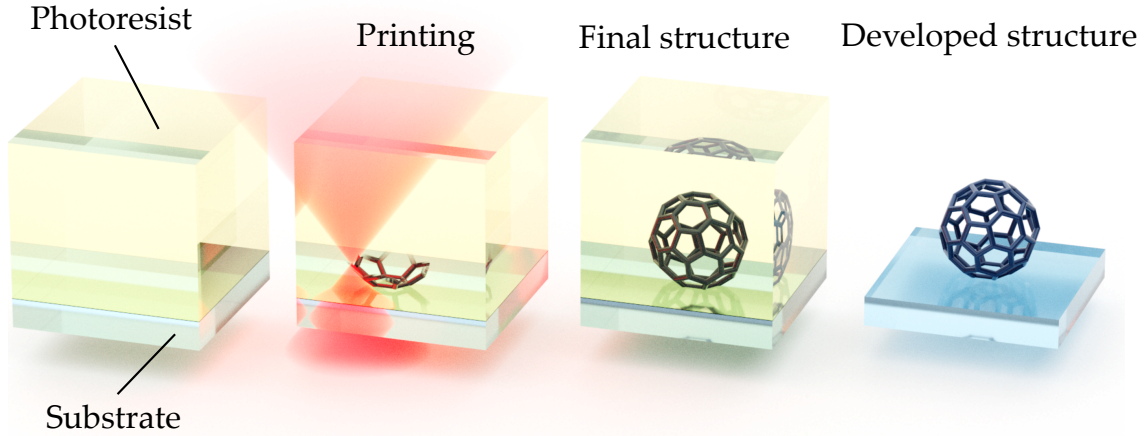


Figure 2.1: 3D laser microprinting principle. A droplet of a photoresist is applied to the substrate. Subsequently, the printing process starts from the substrate-photoresist interface. Printing proceeds in a slice-by-slice manner until the final 3D structure is fabricated. The liquid photoresist is washed out during development and the solid polymer structure is produced. Adapted from [33].

2.1.2 Feature Size

The resolution of laser printing is not defined in the same manner as it usually is in microscopy and is not constrained by the diffraction limit. and is not constrained by the diffraction limit. Moreover, the two terms "minimum feature size" and "printing resolution" are often confused or not clearly distinguished. To understand the main difference between these values, one should consider the laser printing concept from two perspectives.

The first perspective involves the focusing of the laser beam by an objective lens with a numerical aperture (NA). The focused laser beam, with the wavelength λ , produces a diffraction-limited spot, defined by Abbe's resolution limit as

$$a_{xy} \geq \frac{\lambda}{2NA}. \quad (2.1)$$

This well-known formula was derived from Fraunhofer diffraction, considering the imaging case as the transmission type of grating. In the same manner, considering multiple laser beams generating a 3D interference pattern, the minimum axial grating period can be estimated as [34]

$$a_z \geq \frac{\lambda}{n - \sqrt{n^2 - NA^2}}. \quad (2.2)$$

Equation 2.1 and Equation 2.2 are considered appropriate approximations for determining the minimum feature size in routine printing procedures. When

calculating the feature size, for example, with $n = 1.5$, $\lambda = 780$ nm, and $\text{NA} = 1.4$, parameters that are similar to real conditions, the resulting voxel size will be approximately 280 nm in the lateral direction and 800 nm in the axial direction. These estimations indicate that the voxel indeed has an ellipsoidal shape and is axially elongated, with typical ratios ranging from 2.5 to 7, mainly depending on the objective's NA.

2.1.3 Threshold and Accumulation Models

However, another perspective that should also be considered is the photochemistry of photoresists. Generally, accurately describing all the processes that occur in photoresists after photoinitiation is a complex task that requires solving corresponding differential equations. Nevertheless, proper estimations and phenomenological understanding can be provided by two simple models: threshold and accumulation.

In the threshold model [35], a photoresist molecule can be polymerized only if a certain energy dose, D_{th} , transferred to the molecule by optical absorption, is exceeded. In other words, the experimentally transferred energy dose from the laser radiation should be larger than the certain threshold dose of the photoresist or $D > D_{\text{th}}$. In volume elements, where $D < D_{\text{th}}$, the photoresist remains liquid, and the potentially introduced cross-linking is not strong enough to later withstand the development process. The deposited energy dose for the exposure time t_{exp} is described as the photochemical response of the photoresist as

$$D(\mathbf{r}) \propto t_{\text{exp}} I(\mathbf{r})^N, \quad (2.3)$$

where $I \propto P$ is the optical intensity, proportional to the laser power P , and N is the non-linearity factor, which scales with the underlying photochemical process. Thus, one-photon absorption ($N = 1$) affects the dose linearly, whereas most processes in 3D laser microprinting follow two-photon polymerization, which is a quadratic process ($N = 2$). Two- and one-photon dose distributions, calculated from a Gaussian beam with a beam waist of $w_0 = \lambda/2$ are presented in [Figure 2.2a](#) and [b](#). These distributions demonstrate how voxel sizes vary depending on the ratio of the exposure dose D to the threshold dose D_{th} . For instance, if the deposited dose exceeds the threshold dose by three times, the resulting voxel size in the z -direction will be approximately four times larger than at the threshold dose. Moreover, it is evident that the non-linearity of this process plays a crucial role in restricting the voxel size, particularly when the deposited dose significantly exceeds the threshold value.

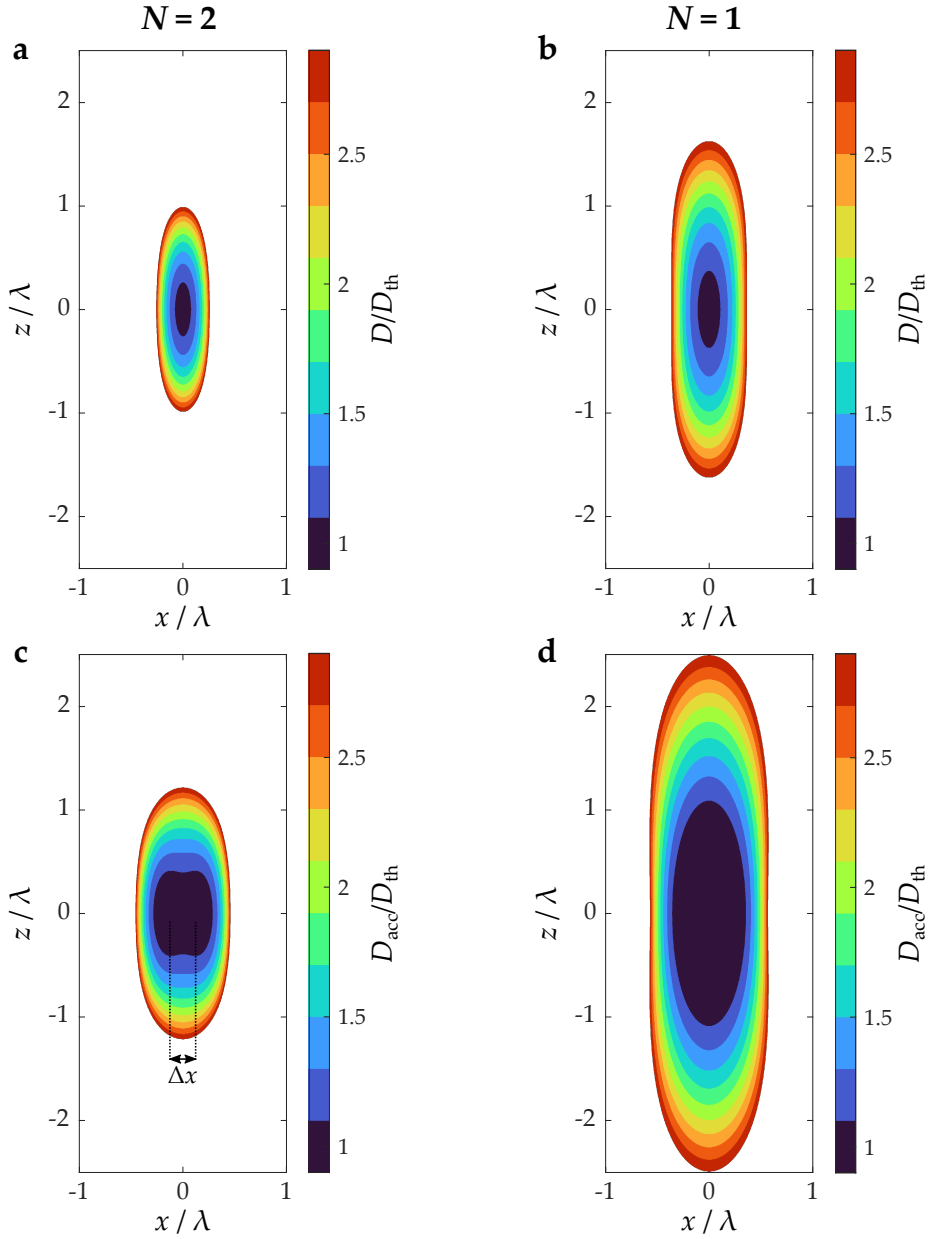


Figure 2.2: Dose simulations of the Gaussian beam with a waist of $w_0 = \lambda/2$ and refractive index $n = 1.5$. **a** Demonstration of the threshold model for the two-photon dose, calculated as the squared intensity of the Gaussian beam. The closer the deposited dose is to the threshold dose D_{th} , the smaller the resulting voxel. **b** The same calculations applied to the one-photon dose, calculated as the intensity of the Gaussian beam. **c** Demonstration of the accumulation model for the two-photon dose. Two doses were deposited with a spacing of $\Delta x = 0.4\lambda$. The minimum spacing corresponds to the resolution limit, which is calculated using Sparrow's criterion (Equation 2.6 and Equation 2.7). **d** The same demonstration for two one-photon doses deposited with the same spacing of $\Delta x = 0.4\lambda$, showing a huge dose accumulation effect.

Theoretically, it is possible to deposit a dose infinitely close to the threshold value, thereby producing arbitrarily small structures and thus producing features smaller than the minimum feature size described by Equation 2.1 and Equation 2.2. Using this strategy, structures as small as 10 nm have been previously produced [36]. However, this represents an extreme case that is unsuitable for reproducible results.

To further understand how polymerization facilitates the printing of lines and how the resolution limit can be defined, the accumulation model is introduced. This model assumes that the photoresist remembers all spatially and temporally transferred doses. The final dose is then obtained by linearly adding the doses from all exposures [35]. This principle can be expressed in the form of equation

$$D_{\text{acc}}(\mathbf{r}) \propto \sum_{i=1}^T t_{\text{exp}_i} I(\mathbf{r}, t)^N, \quad (2.4)$$

where T is the total number of all exposures.

To illustrate the accumulation effect, simulations were performed on the same two- and one-photon dose distributions from Figure 2.2a and b. The doses were deposited twice with the spacing of 0.4λ in the x -direction. The resulting accumulated doses for both cases, calculated as the sum of the two spatially separated doses, are depicted in Figure 2.2c and d. Based on this example, several important observations can be made.

First, there is a critical dose value above which two deposited doses become indistinguishable and merge into a single polymerized part. In Figure 2.2c, for values $D_{\text{acc}} > 1.1D_{\text{th}}$, two separate voxels combine into one. By continuously repeating the voxel deposition in one direction with the focus speed of $v \propto \frac{1}{t_{\text{exp}}}$, it is possible to print a single homogeneous line. In this regime, the dose also becomes inversely proportional to the focusing speed, i.e.,

$$D_{\text{line}} \propto \frac{I^N}{v}. \quad (2.5)$$

Therefore, to achieve high printing speeds while maintaining the same dose value, one must also increase the intensity and, hence, the printing laser power. Modern laser printers can reach printing speeds of up to meters per second, enabling meso- and even macro-scale fabrication [37].

Second, at lower doses near the threshold, one can determine the minimum spacing between two voxels or neighboring lines that remain separated by only a shallow minimum. Further reducing the distance between the voxels will lead to them becoming indistinguishable, and thus, unresolved. This minimal spacing defines the resolution limit in 3D laser printing. In Figure 2.2c, this distance in the

x -direction is highlighted and denoted as Δx . For a diffraction-limited focused beam, Δx is the resolution limit in the x -direction. Its value can be estimated using Sparrow's criterion. According to this criterion, the minimum lateral and axial distances can be approximated by two specific equations [34]

$$\Delta x = \frac{\lambda}{2\sqrt{N} \cdot \text{NA}}, \quad (2.6)$$

$$\Delta z = \text{AR} \cdot \Delta x, \quad (2.7)$$

where AR denotes the aspect ratio between axial and lateral voxel size. Thus, the resolution of canonical two-photon polymerization is approximately 1.4 times smaller than the typical feature size derived from Abbe's resolution limit.

Finally, if the experimental dose significantly exceeds the threshold value or if voxels are deposited in very close proximity, a substantial dose accumulation can occur, leading to the growth of polymerized structures. This phenomenon is commonly referred to in the literature as the "proximity effect" [35]. Notably, the proximity effect is particularly evident in the one-photon process, as depicted in Figure 2.2d. In this case, two voxels cannot be resolved at the simulation spacing distance, and the accumulated voxel is more than twice as large as that in two-photon polymerization. This observation underscores the necessity of non-linearity for achieving the precision required to print arbitrarily small 3D structures. It is worth mentioning that the proximity effect can sometimes be intentionally applied for smoothing printed shapes, especially in micro-optics applications [38].

2.1.4 Important Properties of Photoresists and Polymers

3D laser microprinting relies on multi-photon polymerization, which requires that photoresists have sufficient multi-photon absorption cross-sections to initiate the polymerization reaction. Furthermore, the photoresists need to be transparent to the laser emission wavelength. The absence of linear absorption around the laser wavelength is crucial to ensure effective printing while preventing the photoresist from heating and undergoing uncontrolled one-photon excitation. Thus, photoresists are typically considered transparent at wavelengths far from the one-photon absorption peak, generally in the range from 550 nm to 1100 nm, until vibrational overtones occur [39].

After photoinitiation, a molecule of liquid photoresist solidifies through the polymerization reaction, causing the refractive index of the photoresist to increase to a higher value. Typically, photoresists have a refractive index similar to that of fused silica glass, approximately 1.5. In this work, two commercial photoresists will be used:

1. Nanoscribe IP-S (hereafter referred to as IP-S) with a refractive index of $n_{\text{IP-S}} = 1.483$ and a refractive index change after polymerization of $\Delta n_{\text{IP-S}} \approx 0.026$ [39, 40].
2. Nanoscribe IP-Dip (hereafter referred to as IP-Dip) with a refractive index of $n_{\text{IP-Dip}} = 1.518$ and a refractive index change after polymerization of $\Delta n_{\text{IP-Dip}} \approx 0.030$ [39, 41]. All refractive index values are provided for a wavelength of 630 nm. Refractive index differences are provided for UV-polymerized volumes.

However, the refractive index of printed material depends on the degree of cross-linking and reaches its maximum for fully polymerized volumes, for example, after UV-polymerization [42]. Therefore, although maximum refractive index differences are given, the intermediate values for 3D printed parts often remain undetermined due to variations in the degree of cross-linking, which is influenced by the energy dose deposited into the photoresist [43]. The relationship between the refractive index and the writing parameters will be further explored in subsequent chapters.

Lastly, it is important to address the polymer shrinkage that occurs after both polymerization and development. During polymerization, the polymerized material becomes denser at the molecular level than the unpolymerized liquid volume. As a result, this increased density at the macroscopic level leads to slight shrinkage and deformations of the polymerized parts [44]. However, the most significant effect of polymer shrinkage happens during the development of the printed parts, when unpolymerized oligomers and unreacted initiators are washed out [45, 46]. If the values of a sample's height before development h_{before} and after development h_{after} are known, the resulting axial post-development shrinkage S can be calculated as

$$S = 1 - h_{\text{after}}/h_{\text{before}} (\times 100\%). \quad (2.8)$$

Typical post-development shrinkage values range from 5 to 30%, also depending on the cross-linking degree and, consequently, on the printing parameters [47]. The deduced dependencies of shrinkage on the laser power will be studied in [section 5.2](#).

2.2 PRINTING STRATEGIES

To print a 3D micro-structure, one should implement controllable two-photon polymerization in three dimensions, both on the software and hardware sides. Modern 3D laser printers provide software where users can upload the intended 3D model, typically in a triangulated stereolithography (STL) file. In this software, the model is recalculated to the printer coordinates, sliced in the z -direction with a slicing distance between adjacent layers of Δz , and hatched (divided into lines for

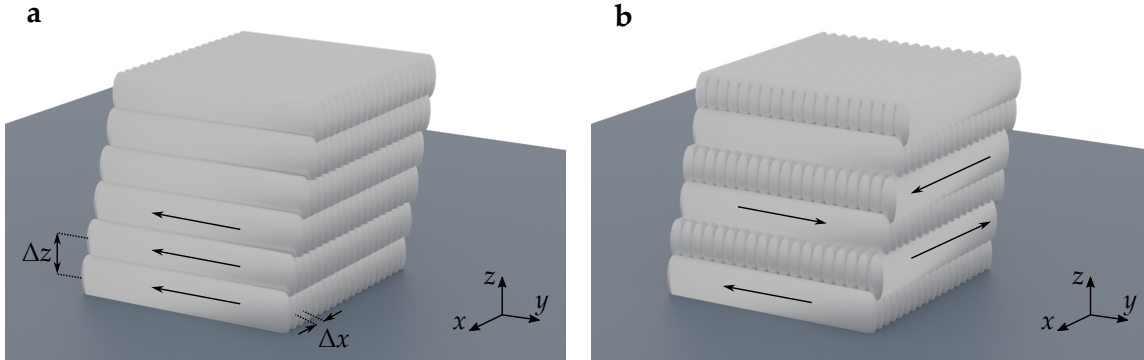


Figure 2.3: Illustration of printing strategies. Structures are printed in a slice-by-slice manner with a slicing distance of Δz and a hatching distance of Δx , starting from the substrate-photoresist interface. **a** A structure printed with uni-directional hatching, where every slicing layer is printed in the same direction (marked by black arrows) **b** A structure printed with cross-directional hatching, where the hatching direction changes by 90 degrees with each slice.

each z -plane) with a hatching distance of Δx (Δy) in the xy -direction. Additionally, users might choose certain advanced printing strategies, such as printing contours or changing the slicing direction with each slice. The latest concept will be used in [section 4.4](#). [Figure 2.3](#) illustrates the structure printed using uni- and cross-directional hatching strategies. Panel **a** showcases uni-directional hatching, where each slice is printed in the same direction, as depicted by the black arrow. Panel **b** depicts cross-directional hatching, where the hatching direction changes by 90 degrees with each slice.

After preparing the set of coordinates, the laser printer hardware uses them to print along pre-programmed trajectories. This usually involves galvo-mirrors or piezo stages for controlling the xy -direction and motorized (often microscopic or piezo) stages for controllable z -positioning. Two-photon polymerization is achieved through femtosecond-pulsed laser radiation, which is focused by a high-NA objective lens. Notably, recent research has demonstrated that an alternative two-step absorption process, utilizing a single continuous-wave laser diode and a specialized photoresist system, can yield results comparable to those achieved with two-photon absorption [48].

2.3 EXPERIMENTAL PRINTING SETUP

Commercial laser printer Nanoscribe Photonic Professional GT (PPGT) was used for 3D laser printing of microstructures throughout this work. The scheme of

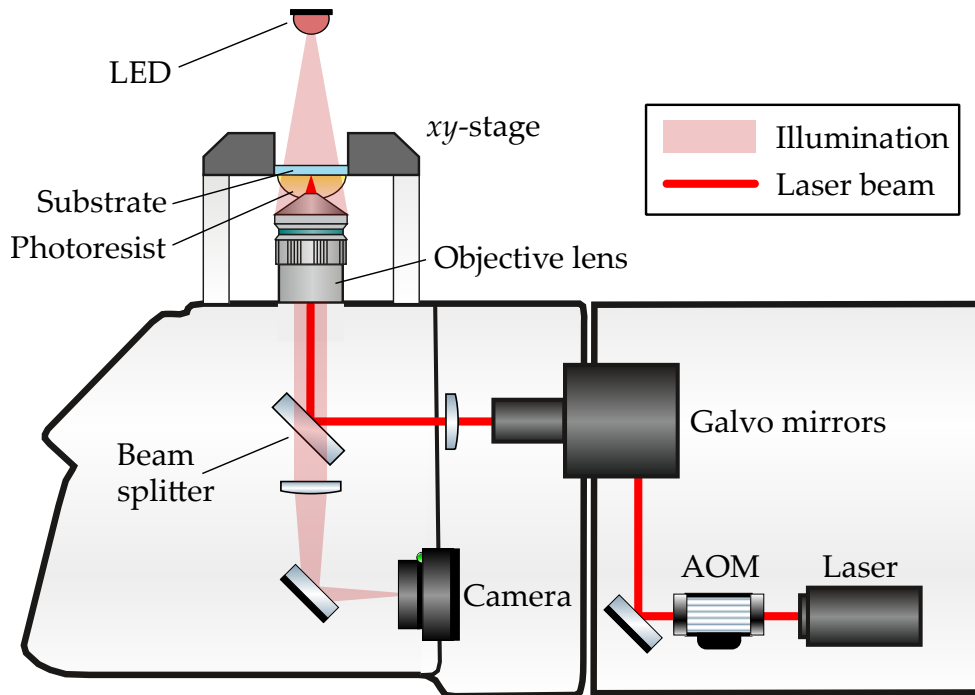


Figure 2.4: Scheme of the commercial laser printer (Nanoscribe PPGT) used throughout this work. The printing system consists of two parts. The laser part consists of a femtosecond laser, acousto-optic modulator (AOM), and galvo mirrors. The microscope part comprises an objective lens that focuses the laser radiation onto the substrate within the volume of the photoresist, xy -stage, light-emitting diode (LED) for illumination, and camera for recording wide-field images. Reworked figure from [33, 49].

the device is presented in [Figure 2.4](#). The printing system consists of two parts. The first part comprises laser printing components such as an erbium fiber laser with a pulse width below 100 fs, a repetition rate of 80 MHz and an emission wavelength centered at 780 nm; acousto-optic modulator (AOM) for adjusting the laser power; and galvo mirrors to scan the laser radiation in the xy -direction. The second part, responsible for focusing and imaging, comprises a modified Zeiss Axio Observer microscope with an immersion objective lens and xy -stage for positioning the sample. A light-emitting diode (LED, Thorlabs M625L4) with a central illumination wavelength of 630 nm and a nominal bandwidth of 17 nm is used together with a 12-bit Zeiss AxioCam MRm camera for wide-field imaging purposes.

Notably, the used printing setup has a slight shift of $-24\ \mu\text{m}$ in the axial direction between the printing plane and the imaging focal plane, also referred to as the in-focus plane. This shift implies that if printing occurs directly on the substrate,

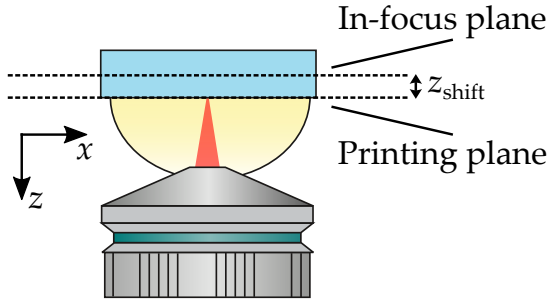


Figure 2.5: In-focus imaging plane shift. z -shift of the printing setup that additionally defocuses in-situ microscope images by $-24\ \mu\text{m}$ towards the substrate. All structures were printed in the dip-in mode.

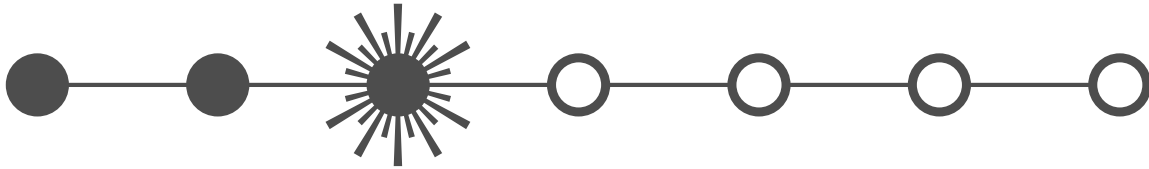
the printed layer will be out-of-focus for wide-field microscope imaging, and the actual imaging focal point will be shifted by $z_{\text{shift}} = -24\ \mu\text{m}$ (Figure 2.5). The minus denotes shifting towards the substrate. The nature of this shift is due to the misalignment of optical components within the microscope setup. Although this shift does not affect the performance of a wide-field microscope during routine in-situ observation, it becomes crucial to account for when simulating realistic images, as outlined in chapter 6.

All microstructures in this work were printed using the "dip-in" mode, where the photoresist is used directly as immersion liquid between the objective lens and the substrate. Transparent ITO-coated and fused silica glasses were used as substrates. Throughout this work, two printing regimes were used:

1. High-resolution regime with a Zeiss Plan-Apochromat $63\times$ NA = 1.4 (hereafter referred to as $63\times/\text{NA}1.4$) objective lens and the Nanoscribe IP-Dip photoresist. The resulting voxel size is estimated as the FWHM of the squared focus intensity profile to be 250 nm in the lateral direction and 600 nm in the axial direction. The corresponding imaging pixel size for this configuration is 160 nm.
2. Mesoscale regime with a Zeiss LCI Plan-Neofluar $25\times$ NA = 0.8 (hereafter referred to as $25\times/\text{NA}0.8$) objective lens and the Nanoscribe IP-S photoresist. The voxel size is estimated as 400 nm in the lateral direction and 2300 in the axial direction. The corresponding imaging pixel size for this configuration is 400 nm.

3 Chapter 3

IN-SITU IMAGING METHODS FOR 3D LASER MICROPRINTING



This chapter is dedicated to the concept of in-situ imaging for monitoring during 3D laser microprinting. First, I will explore the discrepancies between intended 3D models and actual printed structures, highlighting the importance of in-situ imaging for 3D laser microprinting. Subsequently, I will present the main definition and criteria of in-situ imaging for 3D laser microprinting. Following this, both potential and realized methods will be discussed. The theory and derivation of the equations behind the two main methods discussed in this work – optical coherence tomography and quantitative phase imaging – will also be provided.

3.1 TYPICAL CHARACTERIZATION OF PRINTED SAMPLES

Despite the versatility and high resolution offered by 3D laser microprinting technology, printed samples can still exhibit defects and issues that arise during the printing process and subsequent development. These problems often result in deviations between the printed structures and the original 3D models uploaded into the printer software. Issues such as the proximity effect, which leads to unintended polymerization due to dose accumulation, and polymer shrinkage occurring both after printing and development, have already been discussed in the previous chapter. Other common challenges include mechanical instability of the printed specimens [50], overexposure [51], and printing beneath the substrate.

As an example, a 3D buckyball was printed using the $25\times/\text{NA}0.8$ objective and the IP-S photoresist. After printing, the structure was developed and imaged using scanning electron microscopy (SEM). The comparison between the original 3D model and the resulting SEM image, as shown in Figure 3.1, reveals noticeable differences. The printed buckyball is missing a portion of its bottom due to unintentional printing below the substrate. Additionally, the rods significantly deformed due to shrinkage and deformations that occurred during the printing process.

Thus, shape deviations commonly occur during the printing process. These

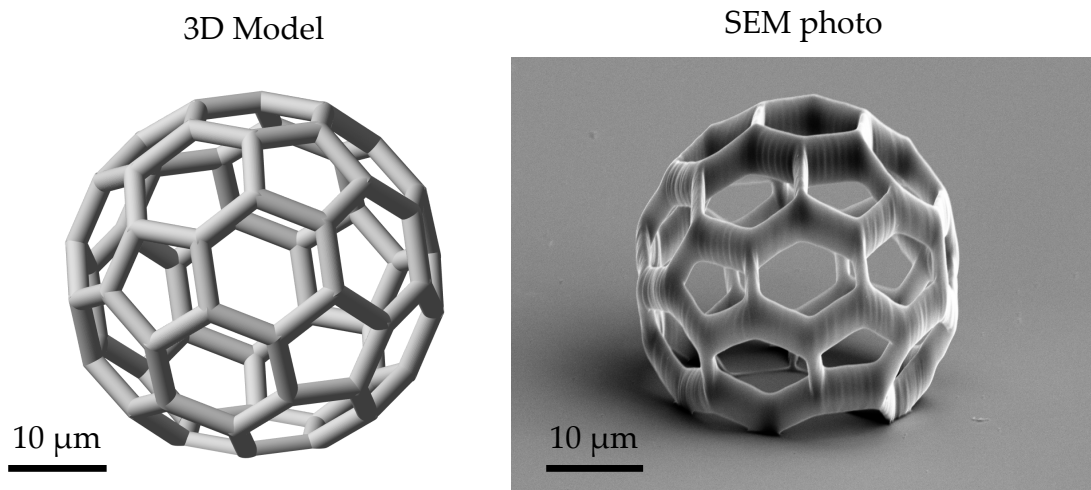


Figure 3.1: Comparison between a 3D buckyball model and the resulting printed structure. 3D stereolithography (STL) model uploaded into laser printer software for further printing (on the left) and the SEM photo of the printed and developed structure showing evident differences (on the right). The presented structure will be further used for in-situ reconstruction using a deep learning approach in [subsection 6.5.3](#).

deviations are particularly problematic in micro-optics, where even minor shape changes can drastically impact optical performance. Consequently, the 3D printing process often requires iterative optimization to accurately reproduce the targeted shape with the necessary quality and precision. To date, this optimization process has primarily utilized imaging techniques, including the previously mentioned SEM, as well as holographic tomography [52], X-ray tomography [53], confocal fluorescence microscopy [54], confocal laser profilometry [55], optical coherence microscopy [56], and atomic force microscopy [57].

All of these methods are performed on the finished and developed 3D-printed parts using separate imaging instruments. Because the structure must be removed from the laser printer and developed before analysis, these techniques are typically referred to as ex-situ methods. Such methods are time-consuming and unsuitable for rapid optimization procedures, as they do not provide real-time feedback.

In contrast, in-situ imaging offers substantial advantages for optimizing 3D printing processes in real time. An in-situ imaging modality can provide an online assessment of the quality and properties of 3D-printed microstructures without the need for additional steps in between.

3.2 IN-SITU IMAGING AND POSSIBLE SOLUTIONS

The in-situ imaging method implies assessing the polymer structure properties and shape in the volume of liquid and photosensitive resist during or immediately after laser printing. In this regard, three simultaneous demands should be met. The proper in-situ imaging modality should

- be fast with respect to the printing process
- have μm -resolution
- not influence the printing process, i.e., not introduce any polymerization or other unwanted chemical modifications to the photoresist.

The third demand significantly lowers the range of possible in-situ methods, excluding all UV- and X-ray-based tomographic approaches, as they would result in the polymerization of a photoresist volume. This leaves only optical tomographic reconstruction methods for consideration. It is also worth mentioning that 3D confocal microscopy, which reconstructs fluorescence 3D maps and is often used for characterizing printed samples ex situ, is unsuitable for in-situ imaging. This limitation arises because the common photoresists used in the printing process exhibit a significant amount of fluorescence, which cannot be distinguished from the fluorescence of the printed parts [39].

In the following sections, both potential and already implemented in-situ character-

ization methods applicable to 3D laser microprinting will be discussed. Included among these methods are interferometric techniques such as optical coherence tomography and digital holographic microscopy, as well as non-interferometric bright-field optical microscopy techniques that can be modified to capture the phase of printed samples.

3.3 OPTICAL COHERENCE TOMOGRAPHY

This section discusses the use of optical coherence tomography (OCT) as a method for in-situ imaging in 3D laser microprinting. It describes the applicability of this technology to laser printing, its operating principles, and the theory behind OCT interference signals. The OCT setup developed for mimicking in-situ imaging of laser-printed specimens and in-situ OCT experimental findings will be presented in [chapter 4](#).

3.3.1 Applicability

OCT is an imaging technique widely used in medicine [58, 59], particularly in ophthalmology [60–62], which non-invasively detects the back-scattered light by interferometric principle. In the context of 3D printing, the refractive index difference between polymer and photoresist is on the scale of $\Delta n \approx 10^{-2}$ and its absolute value is $n_{\text{pr}} \approx 1.5$ [39]. These values can be recalculated to the Fresnel reflection coefficient R expressed in decibels using the formula

$$R(\text{dB}) \approx 20 \cdot \log \left(\frac{\Delta n}{2n_{\text{pr}}} \right) \approx -50\text{dB}. \quad (3.1)$$

Despite the low level of back-reflection on the order of -50 dB, modern OCT systems, with sensitivities exceeding 100 dB [63], can effectively detect it. This capability makes OCT a valuable method for the 3D reconstruction of printed samples based on their back-scattering. Notably, the value of -50 dB was calculated for the specular Fresnel back-reflection. Diffuse scattering may result in even lower values.

Within the broader scope of 3D printing technologies, in-situ OCT has proven effective in various applications. For example, OCT has been demonstrated in combination with extrusion-based bioprinting [64, 65]. In metal additive manufacturing, several studies have employed OCT to monitor surface defects, layer roughness, and the time-dependent thickness of sintered metals [66–68]. Furthermore, OCT has been used to visualize the curing process in semi-transparent polymer droplets [69].

3.3.2 Principle

Experimentally, OCT is based on the Michelson interferometer configuration and utilizes broad bandwidth light sources. The latest provides the important advantage of OCT – low coherence length and hence high axial resolution, which is defined as [70]

$$\Delta z = \frac{2 \ln 2}{\pi n} \frac{\lambda_0^2}{\Delta \lambda}, \quad (3.2)$$

where λ_0 denotes the central wavelength of the illumination source, n is the refractive index of immersion, and $\Delta \lambda$ is the full width at half maximum (FWHM) of the source's emission spectrum.

The lateral OCT resolution is defined in the same manner as for confocal microscopy with the objective's numerical aperture NA [71]

$$\Delta x = \frac{\lambda_0}{2NA}. \quad (3.3)$$

In contrast to confocal microscopy, OCT typically does not utilize optical sectioning and employs low-NA objective lenses. Therefore, a single OCT scan (A-scan) captures all the back-scattering information in the axial direction, constrained only by the optical resolution of the spectrometer and the NA of the objective used. The estimation of the axial field of view (also known as "confocal gating") for an OCT system can be described similarly to the axial response in confocal microscopy as

$$\text{FOV}_{\text{axial}} \approx \frac{2n\lambda_0}{NA^2}. \quad (3.4)$$

Thus, OCT systems utilize low-NA objective lenses to increase the axial field of view up to millimeters of depth. Notably, OCT can also be operated using high-NA lenses that provide the same "confocal gate" regime as confocal microscopy and detect only small axial back-scattering portions of samples. This regime is called optical coherence microscopy [72] and will not be discussed in the scope of this work since it is much slower than common OCT and hence not suitable for fast 3D reconstructions.

Modern OCT systems are divided according to the operational principles into two types: Swept-source OCT (SS-OCT) and spectral-domain OCT (SD-OCT) [70]. SS-OCT is based on a tunable swept laser that sweeps across a broad range of wavelengths, typically between 1060 and 1310 nm, as a function of time. In contrast, SD-OCT utilizes superluminescent diodes (SLDs) centered around 800-900 nm, along with a spectrometer that captures the spectral interference signal simultaneously across the entire wavelength range. It has been shown that the

main characteristics of both OCT types are similar, and the main difference lies in the central wavelength [73]. Thus, SD-OCT typically shows better resolution. Moreover, SLD sources are completely safe for photosensitive resins since they are operated in a continuous-wave regime with milliwatts of power. Therefore, SD-OCT is more suitable for use as an in-situ imaging tool in 3D laser microprinting.

The principal scheme of an SD-OCT system is shown in Figure 3.2. The SLD illumination is divided by a beam splitter into two paths: the sample path, directed toward the sample, and the reference path, directed toward a reference mirror. When back-scattering from both paths recombines, interference occurs. The spectral interference is further detected by a spectrometer and recorded by a CMOS sensor. If one additionally scans the sample in the xy -direction by using, for example, a scanning mirror, the whole back-scattering volume of the sample can be eventually reconstructed.

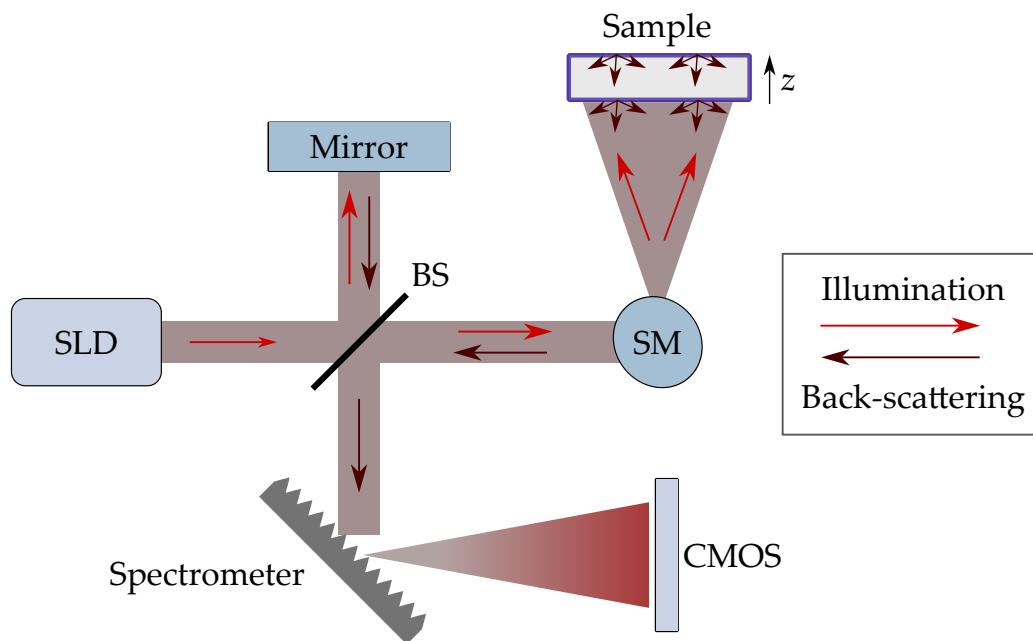


Figure 3.2: Spectral-domain OCT scheme. The light from a superluminescent diode (SLD) is emitted and split into the reference and sample paths by a beam splitter (BS). The sample in this example has two reflective surfaces. The back-scattered light from both paths is recombined at the spectrometer position and the interference signal is captured by a CMOS camera. The sample path can be additionally equipped with a scanning mirror (SM) to enable fast scanning of the whole sample volume. The illumination is marked by light red arrows, whereas back-scattered light is marked by dark red arrows.

3.3.3 Interference Signal

This subsection describes the formation of the interference OCT signal detected by a CMOS sensor. All derivations with little author corrections are taken from [70], Chapter 2.

To calculate the signal registered by a detector, one should consider electric fields on both paths of the interferometer. First, the incident electric field E_I emitted from the SLD can be defined as a polychromatic plane wave

$$E_I = \sum_l S_l \exp(i[k_l z - \omega_l t]), \quad (3.5)$$

where S_l is the complex amplitude of the monochromatic component at frequency ω_l and $k_l = 2\pi/\lambda_l$ is the free-space wavenumber. For the sake of simplicity, all wavenumbers and frequencies are considered in free space and should be rescaled using refractive index n to the real-space distances.

Next, considering a 50:50 beam splitter, the reference electric field E_R after reflecting on the reference mirror and propagating back to the beam splitter can be written as

$$E_R = \frac{E_I}{\sqrt{2}} r_R \exp(ik2z_R), \quad (3.6)$$

where r_R denotes the reflectivity of the reference mirror, z_R denotes the optical path length of the reference beam. The factor of two in the exponential function accounts for the light traveling both forward and backward through the beam splitter. In other words, if the reference mirror position is shifted by Δz , the resulting optical path length will change to $2\Delta z$.

In the same manner, one can write the electric field on the detector after back-scattering introduced by the sample's reflectivity $r_S(z)$

$$E_S = \frac{E_I}{\sqrt{2}} [r_S(z) * \exp(ik2z_S)]. \quad (3.7)$$

Here, $*$ denotes the convolution operation between the sample's reflectivity $r_S(z)$ and the exponential factor. Generally, the sample's reflectivity can be assumed as a finite sum of N single reflectors, then the respective electric field is expressed as

$$E_S = \frac{E_I}{\sqrt{2}} \sum_{m=1}^N r_{S_m} \exp(ik2z_{S_m}). \quad (3.8)$$

The photocurrent I , which is registered by the detector, is proportional to the intensity of interference and can be expressed as

$$I(k) = \frac{\rho}{2} \langle |E_R + E_S|^2 \rangle = \frac{\rho}{2} \langle (E_R + E_S)(E_R + E_S)^* \rangle, \quad (3.9)$$

where ρ is the responsivity of the detector or the coefficient between intensity and current (units amperes/watt), and the angular brackets show integration over the response time of the detector. The factor of two appears due to the second pass of each field through the beam splitter.

Since any detector response time would be much longer than the angular frequency oscillations, the temporal terms related to ω will be eliminated after integration. The resulting formula for the interference intensity after averaging over time is written as

$$I(k) = \frac{\rho}{4} S(k) \left| r_R \exp [ik2z_R] + \sum_{m=1}^N r_{S_m} \exp [ik2z_S] \right|^2, \quad (3.10)$$

where $S(k) = \langle |\sum_l S_l \exp (-i\omega_l t)|^2 \rangle$ is the power spectral dependence of the SLD. During the derivation of Equation 3.10, zero z -position was set at the detector location. This formula can be decomposed into three terms

$$I(k) = \frac{\rho}{4} (I_{DC} + I_{cc} + I_{ac}), \quad (3.11)$$

where I_{DC} is the digital current (DC) term, I_{cc} is the cross-correlation term, and I_{ac} is the auto-correlation term. These terms are calculated as

$$I_{DC}(k) = S(k) \cdot (R_R + R_{S_1} + R_{S_2} + \dots + R_{S_N}), \quad (3.12)$$

$$I_{cc}(k) = S(k) \sum_{m=1}^N \sqrt{R_R R_{S_m}} \left(\exp[2ik(z_R - z_{S_m})] + \exp[-2ik(z_R - z_{S_m})] \right), \quad (3.13)$$

$$I_{ac}(k) = S(k) \sum_{m \neq l=1}^N \sqrt{R_{S_m} R_{S_l}} \left(\exp[2ik(z_{S_m} - z_{S_l})] + \exp[-2ik(z_{S_m} - z_{S_l})] \right), \quad (3.14)$$

where $R = |r^2|$ is the power reflectivity value.

These terms are expressed in the frequency domain and can be rewritten to real space by applying the inverse Fourier transform to equations Equation 3.12 – Equation 3.14. As a result, multiplications will be replaced by convolution operations, and exponential functions will be substituted with Dirac delta functions. After applying the sifting property of the Dirac delta function, $f(z) * \delta(z + a) = f(z + a)$, the resulting formulas for terms in real space will take the following forms

$$i_{DC}(z) = \gamma(z) \cdot (R_R + R_{S_1} + R_{S_2} + \dots + R_{S_N}), \quad (3.15)$$

$$i_{cc}(z) = 2 \sum_{m=1}^N \sqrt{R_R R_{S_m}} \left(2\gamma(z + (z_R - z_{S_m})) + 2\gamma(z - (z_R - z_{S_m})) \right), \quad (3.16)$$

$$i_{ac}(z) = 2 \sum_{m \neq l=1}^N \sqrt{R_{S_m} R_{S_l}} \left(2\gamma(z + (z_{S_m} - z_{S_l})) + 2\gamma(z - (z_{S_m} - z_{S_l})) \right), \quad (3.17)$$

where $\gamma(z)$ is the Gaussian function, which describes the axial point spread function of the OCT system and can be expressed as

$$\gamma(z) \propto \exp\left(-\frac{z^2}{\Delta z^2}\right). \quad (3.18)$$

Here, Δz is calculated using [Equation 3.2](#).

Each of the three derived terms has its own physical meaning:

1. The DC term i_{DC} represents detector current and is independent on the path length. Thus, the DC term is the large artifactual signal centered at zero path length difference.
2. The cross-correlation terms i_{cc} represent actual interference signals between the reference mirror and sample's reflectors and depend on the optical path length difference. Identifying these terms is the main goal of OCT imaging. It is worth mentioning that these terms are proportional to the sample's reflectance. This fact will be further used for the refractive index derivation in [section 4.3](#).
3. The autocorrelation terms i_{ac} describe interference that occurs between reflectors of the sample and are typically considered as small noise artifacts located around the DC-term.

An SD-OCT system captures all spectral components of $I(k)$ simultaneously and retrieves the sample reflectivity profiles $R_S(z_s)$ in real space by applying the inverse Fourier transform. An example of an A-scan in real space, which includes all three terms and features two discrete sample reflectors, is shown in [Figure 3.3](#). As observed from the figure, the cross-correlation terms also have twin complex conjugate artifacts, which are always present in OCT scans.

To account for the sample's refractive index n and remove the scaling factor of two, the optical path length is usually recalculated into new coordinates $\hat{z} = z/2n$. In these recalibrated coordinates, the center-to-center distance between cross-correlation terms accurately corresponds to the actual distances between reflectors within the sample.

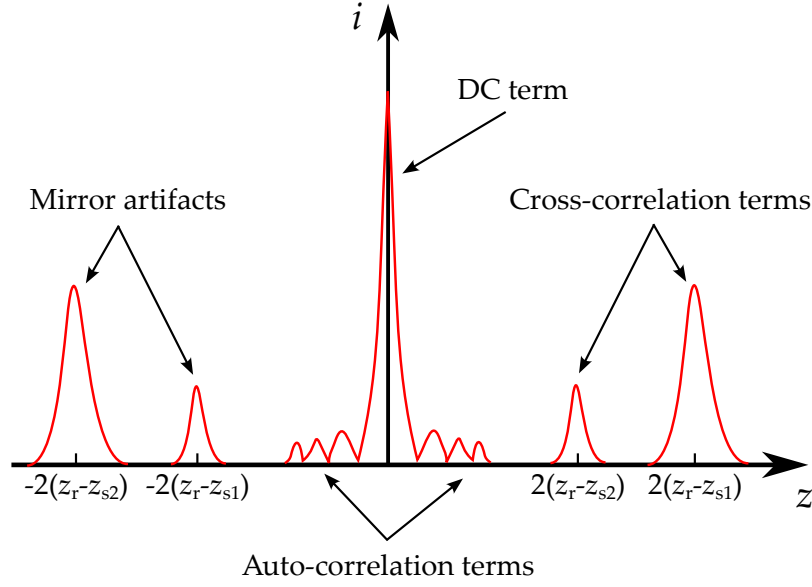


Figure 3.3: Typical OCT A-scan from two discrete sample reflectors. A-scan represents the inverse Fourier transform of the detected interference signal $i(z)$ and showcases all three types of terms, calculated using Equation 3.15 – Equation 3.17. Notably, the cross-correlation terms have mirror images or complex conjugate artifacts, located symmetrically opposite the zero path length position (the midpoint in the graph).

3.4 BRIGHT-FIELD OPTICAL MICROSCOPY

As depicted in Figure 2.4, the laser printing setup partially consists of an optical microscope. Thus, bright-field optical microscopy is the only in-situ inspection method routinely used in 3D laser microprinting.

Since photoresists exhibit almost zero absorption at the illumination wavelengths (as explained in subsection 2.1.4), the printed specimens also lack absorption and can be considered pure-phase objects, characterized by a complex transmission function $T \propto e^{i\Delta\phi}$. Here, $\Delta\phi$ is a phase shift (or optical path difference), which is related to the product of the sample's refractive index contrast $\Delta n(\mathbf{r})$ and height $h(\mathbf{r})$ as

$$\Delta\phi(\mathbf{r}) = \frac{2\pi\Delta n(\mathbf{r})h(\mathbf{r})}{\lambda}, \quad (3.19)$$

where $\mathbf{r} = (x, y)$ and λ is the wavelength of the illumination source. Given an incident plane wave illumination and an ideal imaging system, the sample field is replicated at the image plane with the image field amplitude A_i . The resulting microscopic intensity of the pure-phase object located in the in-focus plane will be

then expressed as [74]

$$I(\mathbf{r}) = |A_i e^{i\Delta\phi(\mathbf{r})}| = A_i^2. \quad (3.20)$$

Thus, a focused image of a thin printed object will typically show constant intensity in the x - and y - directions, making the object invisible under an optical microscope in the laser printer. However, if the object is defocused, meaning the in-focus plane (or image plane) is shifted, the intensity will no longer be described by Equation 3.20. To calculate defocused intensities, it is necessary to compute field propagation in the axial direction using either the Rayleigh-Sommerfeld diffraction theory or the angular propagation method [75]. More detailed information on optical field propagation will be provided in chapter 6.

The resulting defocused image will display diffraction patterns caused by scattering due to the refractive index differences between the polymerized and unpolymerized parts. Therefore, slight defocus is essential to visualize 3D-printed specimens. An experimental demonstration of this effect is shown in Figure 3.4. Here, a half-sphere with a radius of 15 μm was printed using the 25 \times /NA0.8 objective lens and IP-S photoresist. The left image shows an in-focus in-situ microscopic image with almost constant intensity contrast. However, when the sample is defocused by 50 μm in the z -direction, diffraction patterns become visible.

Typically, such microscopic images acquired during printing are utilized for defining the polymerization/overexposure thresholds for unknown photoresists [76]

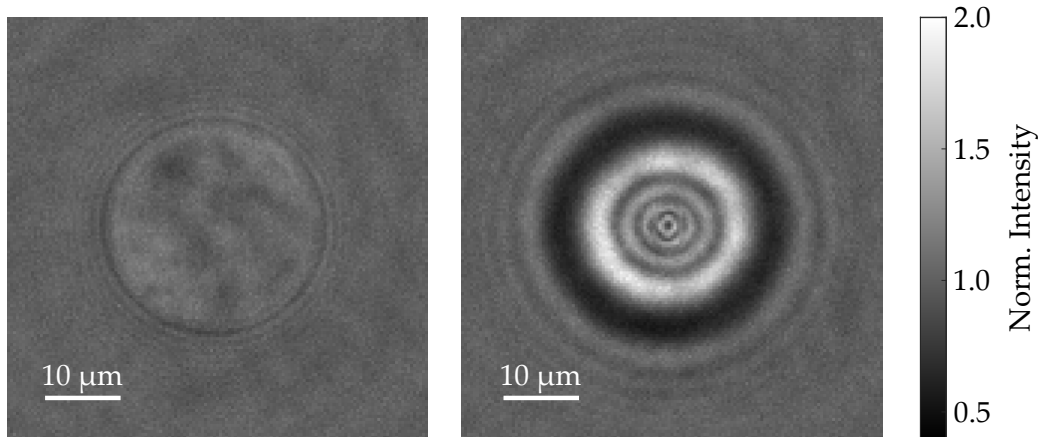


Figure 3.4: In-situ microscopic intensity images of a printed half-sphere. The in-focus image of a half-sphere with a radius of 15 μm on the left shows almost no intensity contrast. Slight visible patterns appear mainly due to the imperfection of the imaging system. When the sample is defocused, the out-of-focus image on the right reveals diffraction patterns. The intensities were normalized to the mean background level.

or for the detection of obvious deformations that may occur during the printing process [77]. However, beyond these specific applications, interpreting diffraction patterns to derive meaningful conclusions from such images is extremely challenging. Therefore, bright-field in-situ imaging alone cannot reconstruct or characterize printed specimens without supplementary methods. One such method, which involves extracting quantitative phase information about the sample, will be discussed in the next section. Another method involves solving the inverse scattering problem for intensity images taken during laser printing. The implementation of 3D refractive index reconstruction, using a deep learning approach to solve the inverse optical problem, will be detailed in [chapter 6](#).

3.5 QUANTITATIVE PHASE IMAGING

As shown in the previous section, the printed objects introduce phase shifts described by [Equation 3.19](#). These phase shifts encode valuable information about the refractive index difference and the height of the printed specimen. The set of techniques that measure sample's phase shifts is known as quantitative phase imaging (QPI). This section will present the two most common QPI techniques: interferometric digital holographic microscopy and non-interferometric phase measurement using the transport-of-intensity equation. Both methods will be discussed in the context of in-situ imaging for laser printing. Additionally, optical diffraction tomography which reconstructs refractive index differences from multiple-angle QPI measurements will be detailed at the end of this section.

3.5.1 Phase Imaging

Historically, the era of phase imaging began with Frits Zernike's invention of phase contrast microscopy. Zernike found that phase shifts in the light that occur from optical path difference as light propagates through a sample in bright-field microscopy $\Delta\phi$ could be converted into visible intensity contrast [78]. Phase-contrast microscopy employs phase plates that shift the unscattered light by $\pi/2$, creating constructive interference between the scattered and phase-shifted background light. The intensity of the resulting microscopic image then becomes proportional to $\Delta\phi$. However, quantitative phase extraction remained a challenge, as phase shifts are nonlinearly coupled with intensity, and cannot be directly determined numerically without additional manipulations.

Further exploration of phase role in imaging was advanced by Dennis Gabor with the invention of holography [79]. Holographic methods provided tools for recording both amplitude and phase information simultaneously. The in-line scheme of writing and reading holograms, originally proposed by Gabor, is

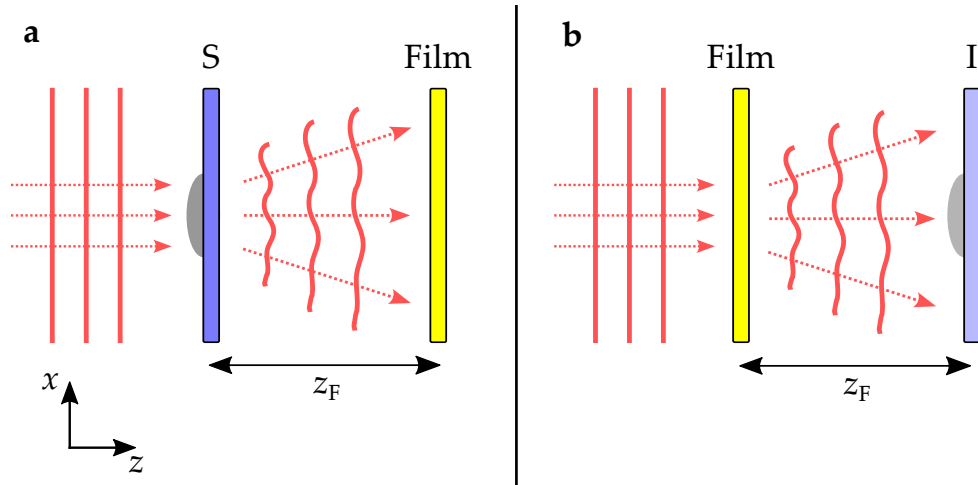


Figure 3.5: Principle of in-line holography. **a** The writing scheme involves a plane wave illuminating the sample (S), with its diffraction patterns recorded onto a photosensitive film. **b**. The reading scheme uses the same plane wave to illuminate the recorded film, reconstructing the image of the sample at the same Fresnel distance z_F used for recording.

presented in [Figure 3.5](#). The writing of the hologram (panel **a**) involves recording Fresnel diffraction patterns of the imaging sample onto a photosensitive film located at the distance z_F . The reading procedure (panel **b**) is the reverse process by which the hologram is illuminated with a plane wave, and the resulting image is observed from the same Fresnel distance z_F .

Both the inventions of phase microscopy by Zernike and holography by Gabor significantly pushed forward the field of light microscopy and laid the groundwork for the development of quantitative phase imaging and optical tomography methods. For their groundbreaking contributions, Zernike and Gabor were awarded Nobel Prizes in Physics in 1953 and 1971, respectively [78, 79].

3.5.2 Digital Holographic Microscopy

It is essential to note that the in-line scheme proposed by Gabor had a significant drawback: it produced a complex-conjugate virtual image at a distance of $-z_F$. To address this issue, Emmett Leith and Juris Upatnieks proposed the off-axis holography method [80]. The off-axis scheme, based on the Mach-Zender interferometer, became a universal tool for holographic imaging and, with the advancement of digital algorithms and sensitive CCD cameras, evolved into widely used digital holography and digital holographic microscopy [74, 81].

The scheme of off-axis digital holographic microscopy is presented in [Figure 3.6](#).

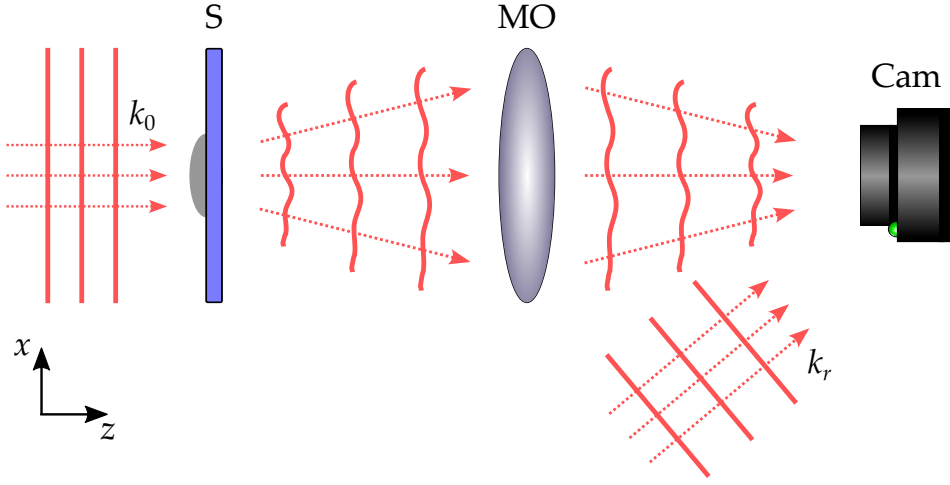


Figure 3.6: Principle of digital holographic microscopy. A coherent and monochromatic beam with a wavevector k_0 is transmitted through the sample (S) and focused by a microscope objective lens (MO). Additionally, an off-axis reference beam with a wavevector k_r is used to produce interference, which is registered by a camera (Cam). The phase of the sample is then reconstructed from the interference patterns in the frequency domain.

In this setup, off-axis interferometry occurs between the electric field transmitted through the sample (S) and microscope objective (MO), E_f , and angularly shifted reference field, E_r .

The resulting hologram, registered by a camera (Cam) is then written as [74]

$$\begin{aligned} I_h(\mathbf{r}) &= |E_f(\mathbf{r}) + E_r|^2 = \\ &= |E_f(\mathbf{r})|^2 + |E_r|^2 + E_f(\mathbf{r}) \cdot |E_r|e^{-k_{rx}x} + E_f^*(\mathbf{r}) \cdot |E_r|e^{k_{rx}x}, \end{aligned} \quad (3.21)$$

where \mathbf{r} is the 2D spatial vector, $k_{rx} = k_r \cdot \sin \theta$, and θ is the off-axis angle of the reference field. The digital reconstruction is further performed in the frequency domain. After the Fourier transform, the hologram can be written in three terms

$$i_h(\mathbf{k}) = i_0(\mathbf{k}) + i_{-1}(\mathbf{k}) + i_{+1}(\mathbf{k}), \quad (3.22)$$

where $\mathbf{k} = (k_x, k_y)$. Three terms correspond to the zeroth order and two diffraction orders of interest. After measuring one of the first-order terms, for example i_{+1} , which is expressed as

$$i_{+1}(\mathbf{k}) = |E_r| \cdot \widehat{E}_f(k_x - k_{rx}, k_y), \quad (3.23)$$

one can determine the field E_f . By further applying the deconvolution operation to propagate the field back to the sample, it is possible to derive the complex sample field E_s and hence the sample's phase shift $\Delta\phi$.

In the context of 3D printing, digital holography has been applied to extract the phase information of printed 2.5D gratings and calculate their refractive index [82]. Particularly, the authors skipped the development step and measured holographies of printed samples in the same photoresist volume that was used for printing. Although the authors did not use the term "in situ" directly, their approach can be considered as in-situ digital holographic microscopy.

Despite digital holography being the primary method for QPI, other interferometric techniques – such as phase shifting microscopy [83], optical quadrature microscopy [84], and Fourier phase microscopy [85] – can also be utilized for quantitative phase extraction.

3.5.3 Transport-of-intensity Equation

In in-situ imaging for 3D laser microprinting, non-interferometric methods are particularly noteworthy because they eliminate the need for highly complex optical setups. For instance, the basic non-interferometric QPI method via the transport-of-intensity equation (TIE) requires merely an optical microscope and a stage for movement in the z -direction [86].

The TIE for QPI was first introduced by Teague under the paraxial approximation in 1982 [87]. The derivation starts from the Helmholtz equation

$$(\nabla^2 + k^2)U(\mathbf{r}_{3D}) = 0, \quad (3.24)$$

where $\mathbf{r}_{3D} = (x, y, z)$ and $k = 2\pi n/\lambda$ is the wavenumber in the medium with the refractive index n . Considering a paraxial monochromatic coherent beam propagating along the z -direction, its complex amplitude is written as

$$U(\mathbf{r}_{3D}) \approx U(\mathbf{r}, z) \exp(ikz). \quad (3.25)$$

After substituting Equation 3.25 into Equation 3.24, one receives

$$\nabla^2 U(\mathbf{r}, z) + 2ik \frac{\partial U(\mathbf{r}, z)}{\partial z} = 0. \quad (3.26)$$

The equation Equation 3.26 describes the propagation law along the z -direction under the paraxial approximation. The phase representation of the beam propagating along the z -direction can be written as

$$U(\mathbf{r}, z) = \sqrt{I(\mathbf{r})} \exp(i\phi(\mathbf{r})), \quad (3.27)$$

where $\phi(\mathbf{r})$ is the phase of the beam. After substituting Equation 3.27 into Equation 3.26 and separating the real part, one can deduce the TIE [88, 89]

$$-k \frac{\partial I(\mathbf{r})}{\partial z} = \nabla[I(\mathbf{r})\nabla(\phi(\mathbf{r}))]. \quad (3.28)$$

The TIE describes the relationship between the axial intensity derivative and the phase of a coherent paraxial beam propagating along the z -axis. If the imaging object has no absorption and consists of a pure phase, such as laser-printed specimens, then Equation 3.28 can be rewritten as a standard Poisson equation [86]

$$-\frac{k}{I_0(\mathbf{r})} \frac{\partial I(\mathbf{r})}{\partial z} = \nabla^2 \phi(\mathbf{r}), \quad (3.29)$$

where $I_0(\mathbf{r})$ is the in-focus background intensity. This Poisson equation can be solved in the frequency space by applying the Fourier transform \mathcal{F} to both parts of Equation 3.29

$$\mathcal{F} \left[-\frac{k}{I_0(\mathbf{r})} \frac{\partial I(\mathbf{r})}{\partial z} \right] = C(\mathbf{u}) = -4\pi^2 |\mathbf{u}|^2 F[\phi(\mathbf{r})], \quad (3.30)$$

where $\mathbf{u} = (u_x, u_y)$ is the spatial frequency vector. Finally, the formula for the phase is obtained by applying the inverse Fourier transform \mathcal{F}^{-1}

$$\phi(\mathbf{r}) = \mathcal{F}^{-1} \left[-\frac{C(\mathbf{u})}{4\pi^2 |\mathbf{u}|^2} \right]. \quad (3.31)$$

The singularity at $(u_x, u_y) = (0, 0)$ can be avoided, for example, by predefining the Fourier transform of the phase at the frequency center $\mathcal{F}[\phi(0, 0)] = (0, 0)$. Equation 3.31 is typically solved computationally by applying the fast Fourier transform (FFT) [90].

From the experimental point of view, defining the phase of the object requires only the measurement of the axial intensity derivative $\frac{\partial I(\mathbf{r})}{\partial z}$. Thus, using a conventional optical microscope equipped with a motorized z -stage is sufficient. The principal scheme of TIE-QPI is shown in Figure 3.7. The sample is usually illuminated by a plane wave and registered by a microscope camera. By moving the sample in the z -direction and capturing images at the in-focus plane, denoted as z_0 , as well as both above (z_+) and below (z_-) this plane, one could accurately calculate the intensity derivative.

The lateral resolution of the measured phase is defined by the microscope objective lens NA and the illumination wavelength as indicated in Equation 3.3. The phase sensitivity of this method, which correlates with the minimum resolvable feature at a fixed refractive index, can vary based on the numerical algorithms used, the contrast in the refractive index, and the details of the imaging setups. Generally, it is accepted that TIE-QPI is a high-sensitive technique with a phase sensitivity

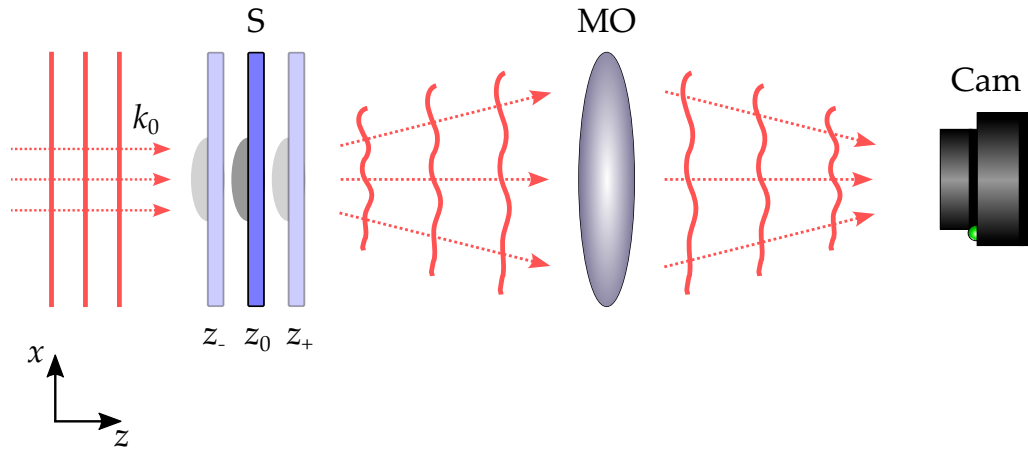


Figure 3.7: Experimental configuration of TIE-QPI. A coherent beam is transmitted through the sample (S), focused by a microscope objective (MO), and the resulting intensity image is recorded by a camera (Cam). The in-focus position of the sample is marked as z_0 . By recording intensity images at different z -positions of the sample (z_- denotes positions below the in-focus plane and z_+ denotes positions above the in-focus plane), one can extract the sample's phase from the TIE (Equation 3.28).

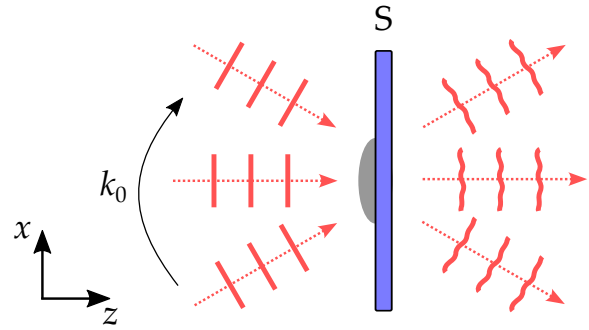
of up to 0.01 radians [91], which corresponds to the in-situ detection of printed features with a height of less than 100 nm.

By utilizing the simplicity of optical setup and high sensitivity, the TIE-QPI method has been efficiently employed in bioimaging and optical metrology. This includes measuring cellular dry mass [92], conducting dynamic cell imaging [93], and characterizing of microlenses and optical fibers [94, 95]. Application of TIE-QPI to phase extraction for 3D-laser printed specimens is discussed in chapter 5.

3.5.4 Optical Diffraction Tomography

Suppose an optical system capable of QPI, for example, a digital holographic microscope, is equipped with an additional xy -scanner to change the illumination direction as depicted in Figure 3.8. In that case, it can measure complex fields scattered from an object under illumination from multiple angles. If the imaging object is weakly scattering, i.e., $\Delta n \ll n$, the measured interferograms can be used to reconstruct the sample's complex 3D refractive index [96]. This method is typically called optical diffraction tomography (ODT). ODT utilizes first Born or Rytov approximations and iterative optimization algorithms to solve the inverse scattering problem and reconstruct the 3D refractive index [97, 98]. Nowadays, ODT is an established label-free microscopic technique widely used for 3D imaging

Figure 3.8: Principle of ODT. The sample (S) is scanned from different illumination directions. The detected scattering patterns from different illumination angles are further utilized to reconstruct the 3D refractive index of the sample by solving the inverse scattering problem.



of cells [99, 100].

In the context of 3D laser printing, ODT has been successfully applied for in-situ imaging purposes. For example, authors from [101], integrated the ODT system into the custom-made 3D laser printer for simultaneous imaging of 3D-printed specimens. An example image of their reconstruction is reprinted with Elsevier's permission and presented in Figure 3.9.

As observed from ODT reconstructions, especially in panel f, the retrieved refractive index suffers from artifacts. This issue is a recognized limitation of ODT, which stems from the limited illumination angle range dictated by the numerical aperture of the objective lens used. This problem, inherent to all tomographic methods with limited angle coverage, is known as the "missing cone artifacts". These artifacts lead to incomplete reconstruction due to missing information [102]. In other words, the underlying inverse problem is ill-posed and cannot be solved without introducing additional artifacts. The ill-posedness of the inverse problem scales with the height of the reconstructed samples. Therefore, attempts to reconstruct even larger volumes than those depicted in Figure 3.9a will result in further degraded reconstruction quality [103]. Specifically, the axial reconstruction error could reach the scale of micrometers or tens of micrometers, which is inadequate for precise in-situ imaging.

In another study focusing on the application of ODT for reconstructing 3D laser-printed samples [104], the authors successfully demonstrated the reconstruction of the refractive index under "quasi" in-situ conditions (using immersion oil instead of photoresist). However, the maximum height achieved in the reconstructions was 10 μm , and even at this scale, the reconstructions were significantly compromised by numerous artifacts.

Summarizing the described attempts, it is clear that in-situ ODT imaging is not feasible for printed specimens larger than 10 μm . To overcome this limitation, further advancements in numerical solvers are required. The application of deep learning to solve the inverse tomographic problem, similar to that encountered in ODT, but using only a single illumination direction, is discussed in chapter 6.

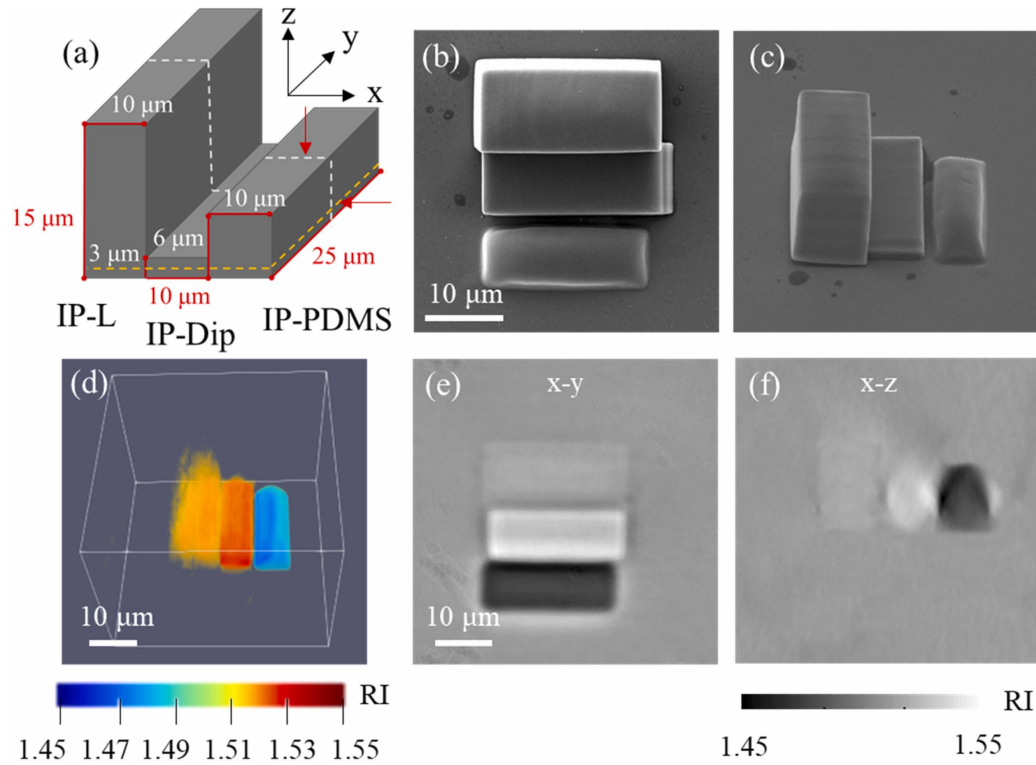


Figure 3.9: In-situ ODT measurements of laser-printed cuboids, reprinted from [101]. ODT experiments of 3D-printed cuboids from different photoresists. **a** Design of the structures. **b** and **c** SEM ex-situ images. **d** Reconstructed 3D refractive index. **e** and **f** different cross-sections of the retrieved refractive index showing artifacts of reconstructions. Reprinted Figure 4 from [101] with permission from Elsevier, license number 5765310917918.

4 Chapter 4

IN-SITU OPTICAL COHERENCE TOMOGRAPHY (OCT)



In this chapter, I will present OCT technology for the in-situ detection of back-scattering of printed samples based on their refractive index differences appearing after polymerization. I will begin by describing the custom-made spectral-domain OCT setup, specifically designed for high-resolution imaging of printed microstructures. This setup mimics in-situ imaging conditions and can be used immediately after printing without requiring sample development. The experimental results will be presented in increasing order of sample complexity: starting with OCT imaging of photoresist volumes before printing, followed by the study of simple geometries with planar surfaces, and concluding with the reconstruction of complex 3D architectures.

4.1 EXPERIMENTAL SETUP

The applicability and theory of OCT technology and its spectral-domain (SD) configuration for in-situ imaging in 3D laser printing were discussed in [section 3.3](#). For efficient in-situ imaging and further reconstruction of printed microstructures, the OCT setup must have the required parameters of resolution, speed, field of view, etc. Therefore, it was essential to develop a custom-made OCT setup tailored to the specific requirements and not rely on commercial OCT systems. This section details the developed experimental SD-OCT setup, beginning with an overview of its optical components, followed by the description of the algorithms employed, and concluding with the experimental validation of its crucial parameters.

4.1.1 Design and Description

The scheme of the developed SD-OCT system is presented in [Figure 4.1](#). The illumination source is a superluminescent diode (SLD, Exalos EXC250002-00) emitting low-coherence light with a central wavelength of $\lambda_0 = 845$ nm and a bandwidth, measured as a nominal FWHM, of $\Delta\lambda = 135$ nm. The spectrum of the SLD is shown in [Figure 4.2a](#) as the orange curve. The SLD bandwidth offers sufficient axial resolution for in-situ imaging, which is approximately 1.6 μm in the photoresist/immersion oil, as calculated using [Equation 3.2](#). The light path is then split into reference and sample arms using a 50:50 fiber coupler (FC). The reference arm (bottom) consists of a fiber collimator (CL), an optical relay, and a reference mirror (RM). To obtain the highest possible OCT dynamic range without saturating the spectrometer detector, a neutral density filter (NDF) is used to optimize the intensity of the reference arm with respect to that of the sample arm. The sample arm comprises the same fiber collimator, two-axes scanning MEMS mirror (Mirrorcle A5M24.2-2400AL), scanning optics (achromatic lenses L1 and L2), and the focusing immersion lens (Plan Apochromat $40\times$ NA1.4 DIC M27, Carl Zeiss).

The OCT setup was designed for standalone in-situ imaging, mimicking the real in-situ situation, with the possibility of potential integration into a laser printer. Therefore, the sample arm was configured to replicate real 3D printer optics and comprises the high-NA (NA = 1.4) objective lens, typically used in 3D laser printing. However, larger values of NA lead to significantly lower axial field of views down to a few micrometers, which can be estimated using [Equation 3.4](#). This limitation makes it challenging to image even small structures. One possible solution is to decrease the effective NA by under-illuminating the back aperture

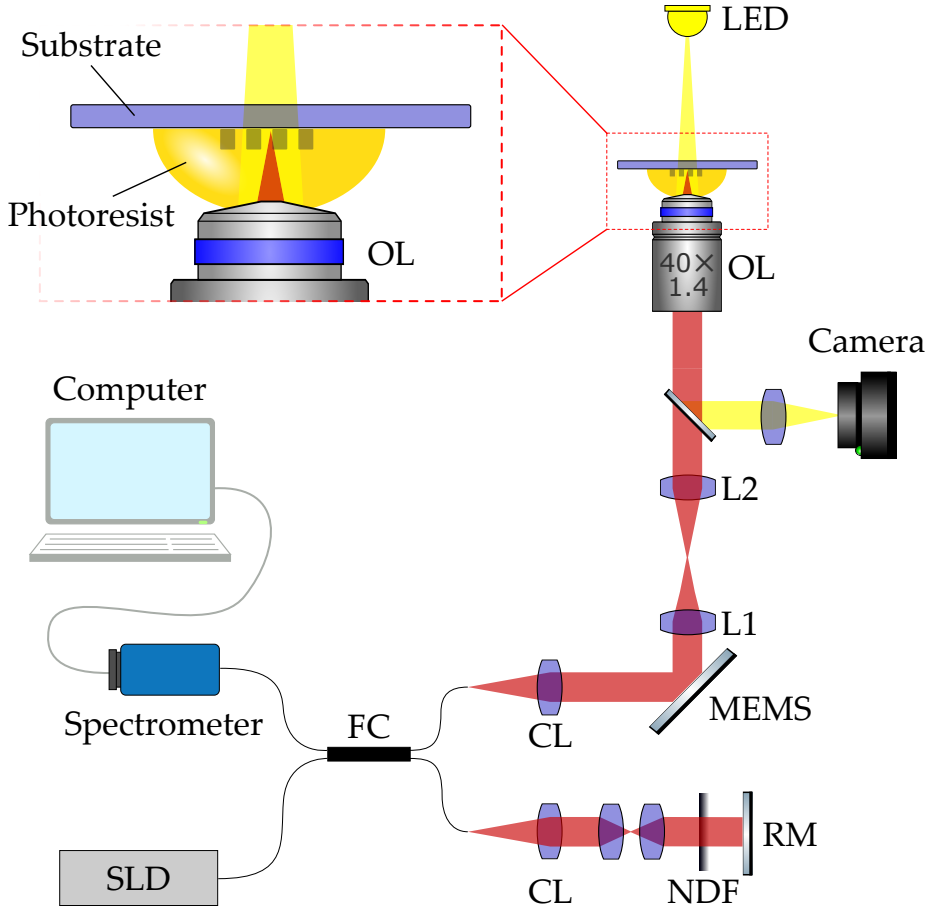


Figure 4.1: Experimental spectral-domain OCT setup. The near-infrared light is emitted from a superluminescent diode (SLD) and split into two arms by a 50:50 fiber coupler (FC). The reference arm (bottom) consists of a fiber collimator (CL), telescope, reference mirror (RM), and a neutral density filter (NDF) to equalize intensities between arms. The beam in the sample arm is scanned by a MEMS mirror, magnified by a telescope (lenses L1 and L2), and focused by a high-NA objective lens (OL) to the printed sample. The objective is immersed in a photoresist. Back-scattering from both arms is recombined and the resulting interference is analyzed and recorded by a spectrometer. The sample is additionally illuminated by an LED and imaged by a conventional microscope camera. Adapted from [105].

of the objective lens. The effective NA is defined as

$$\text{NA}_{\text{eff}} = \frac{dn}{2f}, \quad (4.1)$$

where $n \approx 1.5$ is the refractive index of a photoresist, $f = 4.125$ mm is the objective focal length, and d is the beam diameter. On the other hand, decreasing effective NA to very small numbers will cause pronounced deterioration in lateral

resolution, estimated as Abbe's diffraction limit (Equation 3.3). Thus, by adjusting the beam diameter d , one can find a trade-off between the axial field of view and lateral resolution. In this regard, the scanning optics (lenses L1 and L2) were specifically selected to expand the beam diameter to 1.2 mm, which resulted in $NA_{\text{eff}} = 0.22$. This value provided an extended axial field of view up to 1 mm. As a side effect, the theoretical lateral resolution was reduced to $\approx 1.9 \mu\text{m}$.

Finally, the resulting interferogram is recorded using a fiber-coupled spectrometer with a line-scan detector (Wasatch Photonics CS800-840/180) with an exposure time of $40 \mu\text{s}$ for one A-scan. Typical spectrometer measurements based on the reflection of a substrate-immersion oil interface are presented in Figure 4.2a as the blue curve. The orange curve is given as a demonstration of the signal without interference and consists only of back-reflection from the reference mirror. This signal corresponds to the spectrum of the SLD. The recorded fringes are further evaluated by applying inverse fast Fourier transform (FFT^{-1}) and recalculating wavelengths to z -coordinates by resampling and dividing by the refractive index of immersion. The exemplary evaluated spectrum of the fused silica interface is

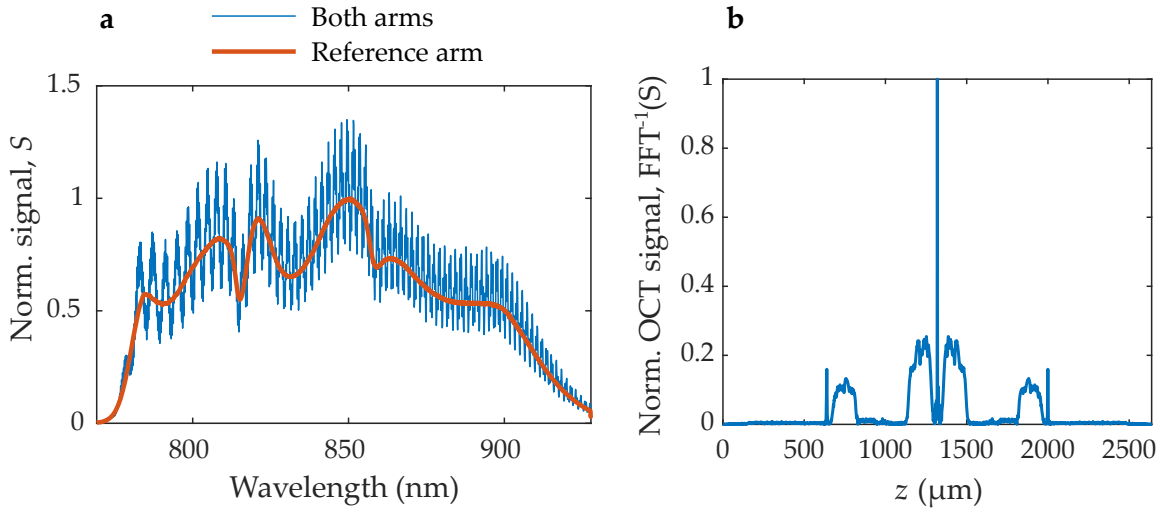


Figure 4.2: Spectrometer measurements of a fused silica substrate interface. **a** The spectrum of the SLD is represented by spectrometer measurements of the reference arm (orange curve) when the sample path is blocked. Interference patterns from the specular reflection coming from a substrate interface are shown in blue when both paths are used to produce the interference. Curves are normalized with respect to the maximum of the reference signal. **b** The resulting OCT signal, obtained as the Fourier transform of blue fringes in panel **a**. The obtained signal is similar to the description of Figure 3.3. The cross-correlation terms are broadened due to the dispersion mismatch. Later, the OCT signal is corrected for the dispersion mismatch using Equation 4.3.

presented in [Figure 4.2b](#). Notably, one can clearly see the same terms, which were derived in [subsection 3.3.3](#): DC-term in the middle, auto-correlation terms around the DC-term, and mirrored cross-correlation terms on the edges.

4.1.2 Workflow

The whole step-by-step in-situ OCT workflow is illustrated in [Figure 4.3](#). Initially, samples were printed using the Nanoscribe PPGT with the IP-Dip photoresist and the $63\times/\text{NA}1.4$ objective and then immediately transferred to the experimental OCT setup. At this stage, the samples were scanned in the x - and y -directions by the MEMS mirror. The measured 3D dataset was then processed according to the standard spectral-domain OCT evaluation algorithm [70], which includes resampling, windowing, dispersion correction, inverse Fourier transform, and recalculation into 3D intensities expressed in decibels.

While most procedures are straightforward, two operations – Hann windowing and dispersion correction – require further explanation.

Hann windowing [106] multiplies the interference spectra by a Hann window function $H(k)$, expressed as

$$H(k) = 0.5\left(1 - \cos\left(2\pi\frac{k}{N}\right)\right), \quad (4.2)$$

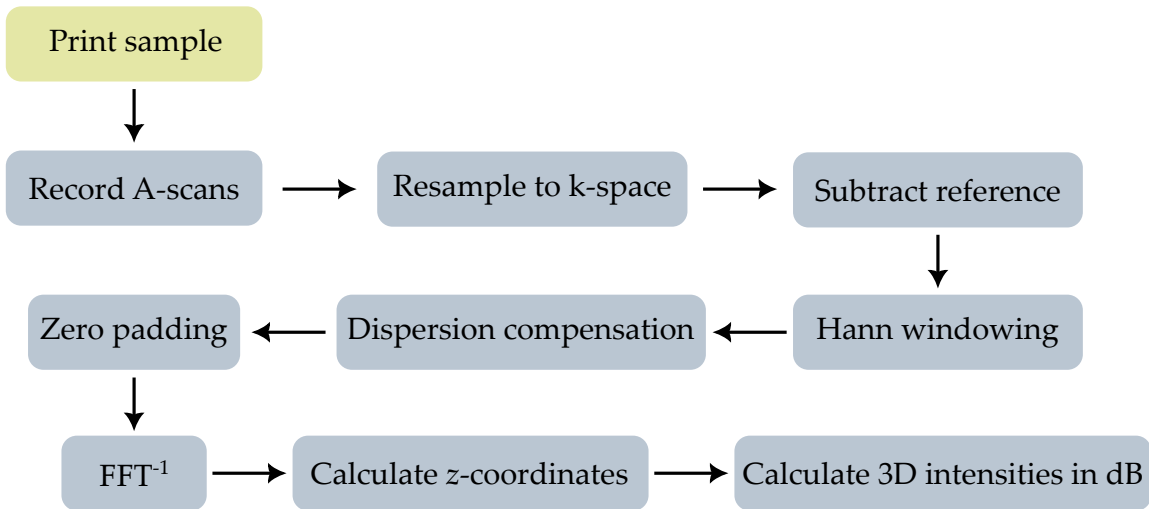


Figure 4.3: Workflow for in-situ OCT. 3D laser printing is performed by Nanoscribe PPGT (yellow block) while OCT imaging (gray blocks) is performed in the "in-situ mode" with a separate custom-made spectral-domain OCT system in the same volume of photoresist used for laser printing. FFT denotes Fast Fourier Transform. All processing operations are performed in a custom-built MATLAB software.

where N is the total number of pixels and $0 \leq k \leq N + 1$. This modification results in effective sidelobe suppression as will be shown in the further subsection.

Dispersion compensation is required to computationally correct for the dispersion mismatch between the two arms. This mismatch causes significant broadening of cross-correlation terms and is necessary for proper OCT evaluation. The dispersion compensation approach was implemented according to [107]. This approach corrects the recorded interference spectra $S(k)$ as $\hat{S}(k) = S(k)e^{i\Delta\phi}$. Here, $\Delta\phi$ is a dispersion correction term expressed as

$$\Delta\phi = a_3(k - k_0)^3 + a_2(k - k_0)^2, \quad (4.3)$$

where a_3 and a_2 are polynomial coefficients and k_0 is the central wavenumber. This polynomial form is chosen because the dispersion propagation constant can be expanded as a Taylor series. Thus, the coefficients a_3 and a_2 are responsible for third- and second-order dispersion mismatches, respectively. The values of these coefficients should be determined empirically, and automatic detection and correction for dispersion mismatch were implemented computationally.

It takes approximately 30 seconds for a regular computer to acquire (10 seconds) and process (20 seconds) the entire volumetric data with a size of 500×500 A-scans. This volume translates to real coordinates as $400 \mu\text{m} \times 400 \mu\text{m} \times 2.6$ mm. It is worth mentioning that the effective range of detection is smaller in the z-direction since the axial field of view is still limited by being less than 1 mm for the developed OCT system.

4.1.3 Validation

Understanding and effectively utilizing the OCT setup goes beyond mere theoretical estimations – it is crucial to also experimentally validate the setup's characteristics.

First, the axial resolution of the setup was experimentally measured by using a single reflector in the sample path and measuring a FWHM of the resulting reflection peak. For this experiment, a single fused silica substrate interface in immersion oil was used as the reflecting surface. The interference spectrum and the corresponding OCT signal from Figure 4.2 were obtained exactly from this surface. The resulting reflection peak after the whole evaluation procedure, including dispersion correction and Hann windowing operation, is illustrated in Figure 4.4a as the orange curve. Additionally, the OCT signal, evaluated without the window function, is plotted as the blue curve. The FWHM of this signal is approximately $2.1 \mu\text{m}$, closely matching the theoretical axial resolution. However, introducing the window operation significantly suppresses sidelobes, which is

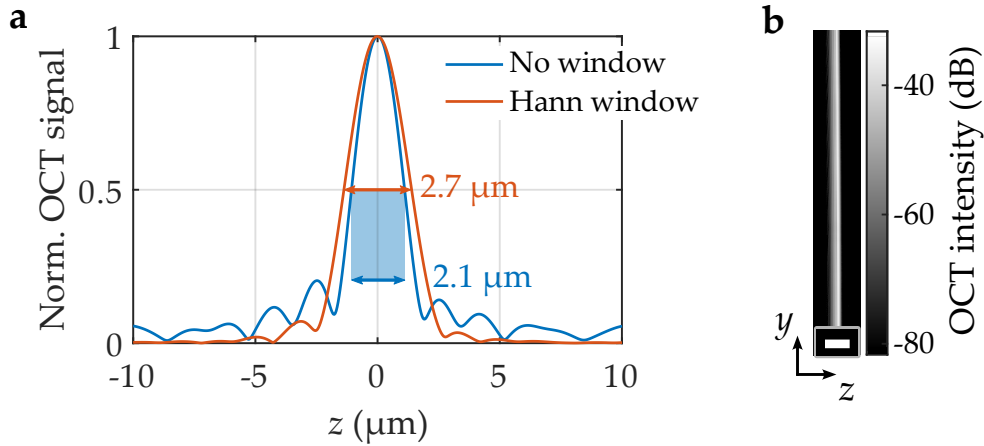


Figure 4.4: Validation of axial resolution based on reflection from the oil-substrate interface. **a** Evaluated OCT signal from the spectrum from Figure 4.2. The OCT signal evaluated without windowing function (blue curve) has a FWHM of $2.1 \mu\text{m}$, which matches the theoretical approximation for the axial resolution. The signal evaluated using the Hann window has fewer sidelobes but a larger FWHM of $2.7 \mu\text{m}$. **b** B-scan of the substrate-oil interface consisting of OCT intensity scanned through y -direction. The scale bar is $20 \mu\text{m}$. Adapted from [105].

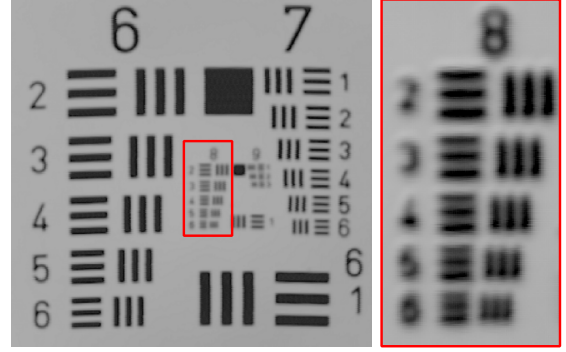
crucial for imaging surfaces with low back-scattering properties. Therefore, it was decided to sacrifice some axial resolution in favor of enhanced sensitivity. Additionally, the B-scan, representing the OCT intensity scanned through the y -direction of the studied substrate-oil interface, is depicted in Figure 4.4b.

Here and in the following results, the OCT signal denotes an absolute value of the inverse Fourier transform, whereas OCT intensity denotes a squared OCT signal. 0 dB corresponds to a 100% reflectivity for both the OCT signal and the OCT intensity.

To measure the experimental lateral resolution of the OCT system, one could use the standard USAF 1951 test target. An OCT *en face* image of the test chart is depicted in Figure 4.5. The elements of the eighth group remain resolved, as illustrated in the enlarged region, where the lowest element corresponds to a center-to-center line spacing of $2.2 \mu\text{m}$. Within the error bars, this measurement aligns with the lateral resolution of $1.9 \mu\text{m}$, derived from Abbe's diffraction limit with $\text{NA}_{\text{eff}} = 0.22$.

The final characteristic required to validate the setup's performance is its sensitivity. The sensitivity of OCT systems is typically defined by the signal-to-noise ratio (SNR), expressed in dB. A common method to assess SNR is by measuring the OCT intensity I using a specular surface with a known reflectivity R [108]. The

Figure 4.5: Validation of lateral resolution based on imaging of the USAF 1951 test target. Overview scan and the enlarged region of the target's eighth group. The center-to-center spacing of the lines of the lowest element (group 8, element 6) is $2.2 \mu\text{m}$, which matches the theoretical lateral resolution of the OCT system. Adapted from [105].



sensitivity is then calculated as

$$\text{SNR}_{\text{max}}(\text{dB}) = 20 \log \left(\frac{I}{\sigma_{\text{bg}}} \right) - 10 \log(R), \quad (4.4)$$

where σ_{bg} is the standard deviation of the background intensity away from the specular surface. The power reflection coefficient R of the interface between optical media with refractive indices n_1 and n_2 with the normal incidence is defined by the Fresnel equation as

$$R = \left(\frac{n_1 - n_2}{n_1 + n_2} \right)^2. \quad (4.5)$$

To evaluate sensitivity, the same fused silica substrate with a refractive index of $n_{\text{sub}} = 1.453$ [109] was immersed in immersion oil with $n_{\text{imm}} = 1.510$. The correspondent Fresnel reflectivity is $R_{\text{sub}} = 3.7 \times 10^{-4}$. The measured average sensitivity of the OCT setup was found to be 105 dB, which is sufficient to detect tiny refractive index differences of less than 10^{-4} .

4.2 INSPECTION OF PLAIN PHOTORESIST

Before examining 3D printed microstructures, OCT images of a droplet of the IP-Dip photoresist on a planar substrate were captured. Figure 4.6 demonstrates OCT reconstructions of volumes for both aged and fresh IP-Dip photoresists. Surprisingly, the aged photoresist exhibits a high density of refractive-index inhomogeneities compared to the fresh photoresist. These "blobs" are interpreted as oligomer groups formed through thermal activation over time.

Although these inhomogeneities were shown to have little effect on laser focusing during 3D laser printing [105], they are still undesirable for several reasons. Firstly, such oligomer conglomerates might serve as seeds for micro-explosions [110] with higher laser powers and potentially lower the over-exposure threshold.

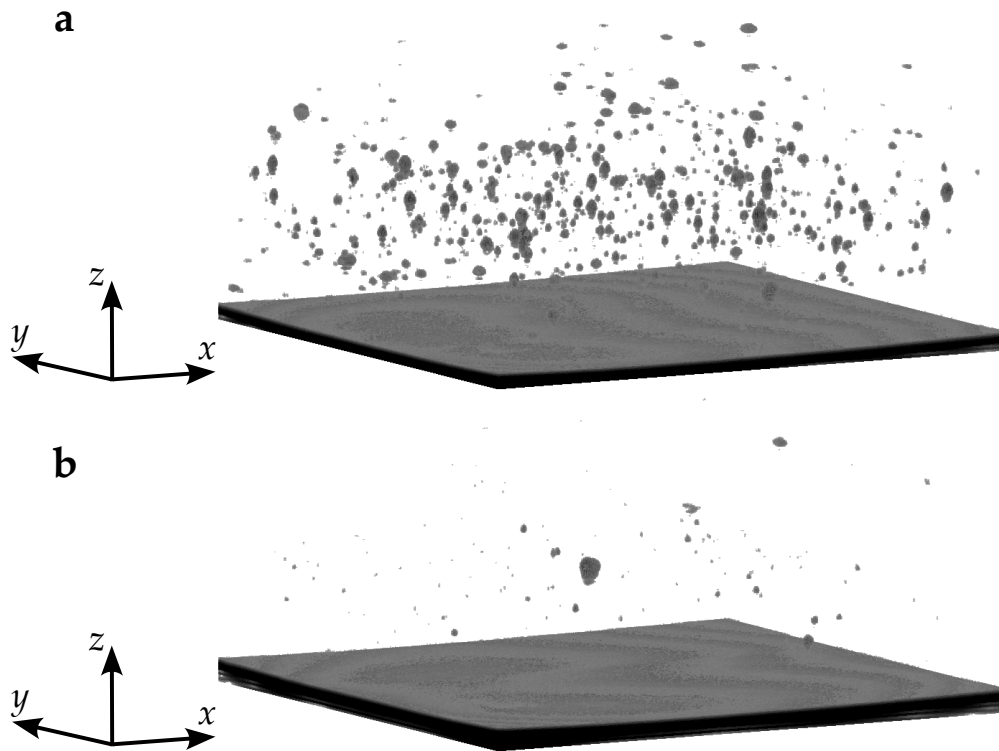


Figure 4.6: OCT reconstructions of plain photoresist volumes. **a** OCT reconstruction of a 5-year-old IP-Dip photoresist. **b** OCT reconstruction of a fresh IP-DIP photoresist. For both cases, the iso-surfaces of the OCT intensities are shown at -65 dB. The axis arrow bars correspond to $50\ \mu\text{m}$. Adapted from [105].

Secondly, these "blobs" might introduce additional artifacts during in-situ imaging and deteriorate the quality of in-situ reconstructions, potentially affecting other imaging methods too, as will be demonstrated in the following chapters. Finally, they might also introduce additional inhomogeneities into the cross-linking density after printing and may even remain after development and change the final properties of printed structures. Therefore, in-situ OCT can detect any undesirable particles and photoresist inhomogeneities before printing, effectively assessing the quality of the photoresist prior to the printing process.

4.3 INSPECTION OF PLANAR SURFACES

Next, simple printed microstructures with only planar surfaces were investigated. As a test sample, cubes with a side length of $30\ \mu\text{m}$ were printed onto a fused silica substrate. The scheme of the experiment is shown in [Figure 4.7a](#). The example of the OCT A-scan taken in the center of one of the printed cubes is presented

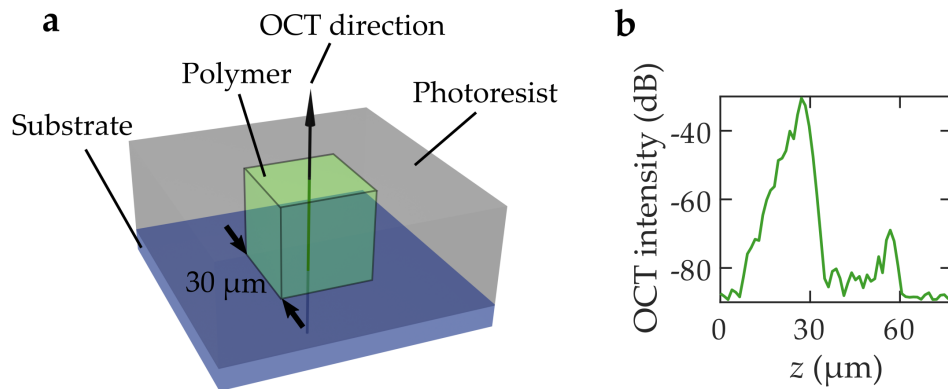


Figure 4.7: Measurements of printed cubes. **a** Scheme of the experiment. A printed polymer cube was immersed in a liquid photoresist and was located on a fused silica substrate. **b** Example OCT A-scan at the center of the cube (marked as an arrow on panel b). Two peaks correspond to two interfaces: substrate-polymer and polymer-photoresist. Reworked figure from [105].

in [Figure 4.7b](#). This A-scan exhibited two peaks corresponding to two interfaces: substrate-polymer (the largest peak) and polymer-photoresist (the smaller peak). Notably, scattering inside the cube is almost negligible and reaches only ≈ -80 dB. The absence of sufficient internal scattering signal hinders the 3D reconstruction of the cube. This problem will be further addressed in the next section.

Furthermore, a peculiarity in the temporal behavior of these two peaks was noted and presented in [Figure 4.8](#). The OCT intensity of the largest peak ([panel a](#)), associated with the substrate-polymer interface, remains stable over hours of measurements, with only minor fluctuations attributed to temperature perturbations. In contrast, the OCT intensity of the lower peak ([panel b](#)), associated with the polymer-photoresist interface, exhibits time instability. It begins at -76 dB, reaches a local maximum of -70 dB after 5 hours, and then decreases again. Both interfaces are examined in detail in the following subsections.

4.3.1 Polymer-substrate Interface

Given the stability of the OCT intensity of the polymer-substrate interface over time, the reflectivity of this interface can be treated in terms of the standard Fresnel reflection law with normal incidence ([Equation 4.5](#)).

As seen from [Equation 3.16](#), OCT intensity I is linearly proportional to the power

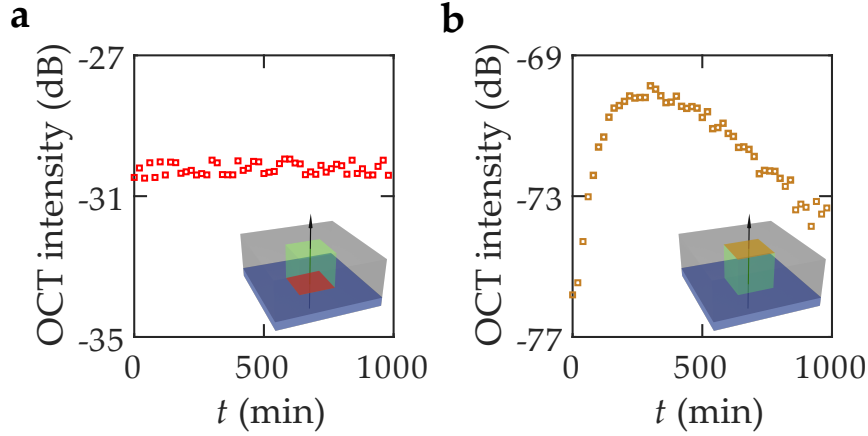


Figure 4.8: Temporal OCT measurements of cube interfaces. **a** Time-dependent OCT intensity of the substrate-polymer interface and **b** the polymer-photoresist interface. Adapted from [105].

reflection coefficient R , hence it can be written as

$$R \cdot k = I, \quad (4.6)$$

where k is a calibration coefficient that has to be calculated from any reference intensity with known reflectivity. As a reference interface, one could simply use the photoresist-substrate interface with measured OCT intensity $I_{\text{pr-sub}}$. Then the coefficient can be found as

$$k = I_{\text{pr-sub}} \left(\frac{n_{\text{pr}} + n_{\text{sub}}}{n_{\text{pr}} - n_{\text{sub}}} \right)^2, \quad (4.7)$$

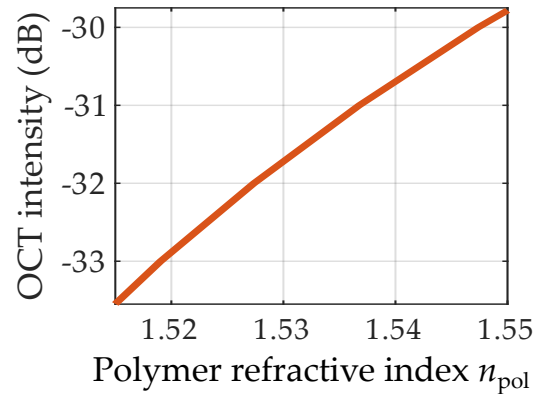
where $n_{\text{pr}} = 1.510$ and $n_{\text{sub}} = 1.453$ are refractive indices of the photoresist and substrate at $\lambda_0 = 845$ nm respectively. Finally, knowing the calibration coefficient and the OCT intensity of the polymer-substrate interface $I_{\text{pol-sub}}$, one could derive from Equation 4.6 the refractive index of the polymer n_{pol} as

$$n_{\text{pol}} = n_{\text{sub}} \frac{1 + \sqrt{\frac{I_{\text{pol-sub}}}{k}}}{1 - \sqrt{\frac{I_{\text{pol-sub}}}{k}}}. \quad (4.8)$$

The derived curve used for the direct translation from a measured OCT intensity to the correspondent polymer refractive index is illustrated in Figure 4.9.

This approach could be utilized to calculate the polymer refractive index for cubes printed with different printing parameters, such as laser power and scanning

Figure 4.9: Translation from OCT intensity to polymer refractive index n_{pol} . The calibration curve is derived from Equation 4.7 and Equation 4.8. Adapted from [105].



velocity. Altering the printing parameters results in changes to the exposure dose, subsequently affecting the cross-linking density and polymer refractive index. The resulting polymer refractive index distribution over writing laser power and scanning velocity is presented in Figure 4.10. Each experimental value of the refractive index is obtained by measuring the OCT intensity of five identically printed cubes, calculating the refractive index using the calibration curve shown in Figure 4.9, and then averaging the results. Writing laser powers vary from the polymerization to the overexposure threshold for each scanning velocity.

As demonstrated in ex-situ studies of Nanoscribe photoresists [39], the polymer refractive index reaches its plateau at a certain value of exposure dose. This effect is associated with the saturation of the polymerization degree, resulting in the formation of a (nearly) fully polymerized structure. The deduced IP-Dip refractive index dependencies are consistent with this theory, showing the saturation value of $n_{\text{sat}} = 1.545$. The saturation value is also consistent with the previous ex-situ studies of the IP-Dip photoresist [42].

4.3.2 Polymer-photoresist Interface

Although OCT provides a fast method of measuring polymer refractive index, this approach still relies on the Fresnel equations, which assume a sharp refractive index transition between two optical media. However, if the refractive index transition is not sharp but is represented as a smooth function, this violates the conditions necessary for the Fresnel reflection equation. This violation explains the unstable temporal behavior of the polymer-photoresist interface shown in Figure 4.8b. To further explore this effect, additional temporal experiments with cubes printed with different laser powers and a scanning velocity of 30 mm/s were carried out. In addition, the time-dependent OCT intensity behavior was also studied for cubes that were developed and re-immersed in the same IP-Dip

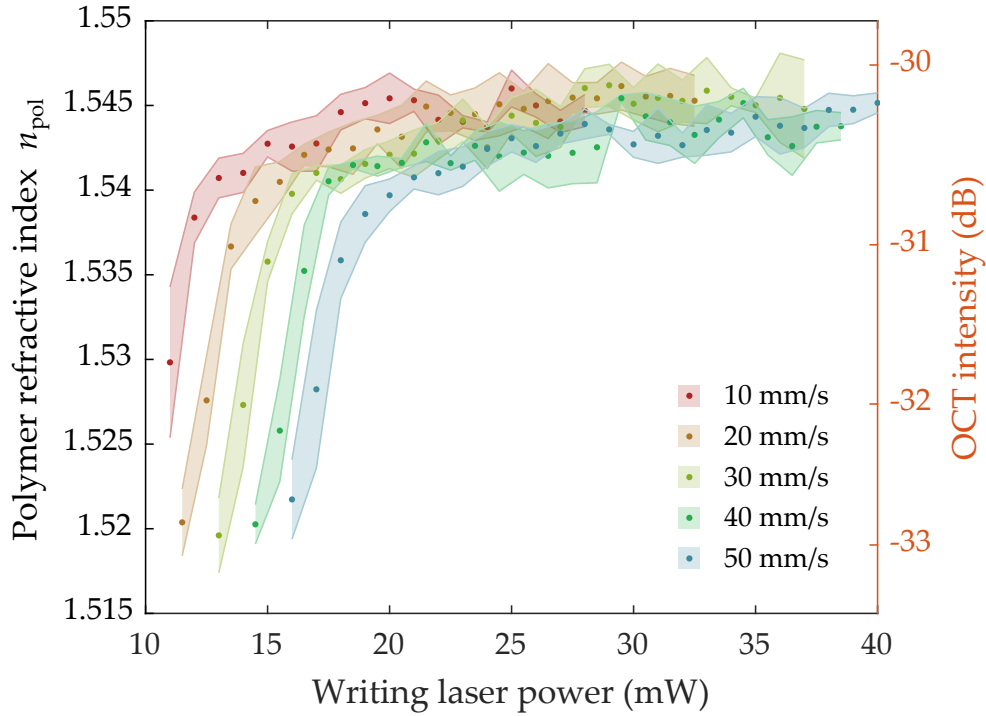


Figure 4.10: Deduced IP-Dip refractive index of cubes for different writing parameters. Refractive index values of cubes printed with different laser powers and scanning velocities. Calculations based on measurements of OCT intensities of the polymer-substrate interface (depicted on the orange vertical scale on the left) and the calibration curve from Figure 4.9. Adapted from [105].

photoresist. The resulting plots are presented in Figure 4.11.

Here, the first column corresponds to the in-situ OCT measurements of printed cubes. Subsequently, printed samples were developed in acetone (second column) or PGMEA (propylene glycol methyl ether acetate, third column), re-immersed back in IP-Dip and immediately measured in the OCT setup again. The rows correspond to the samples printed with different laser powers. Together with the polymer-photoresist interface (blue curves), stable polymer-substrate interfaces (orange dashed lines) were measured as well.

Surprisingly, the temporal behavior of the polymer-photoresist interface curves varies depending on several factors such as laser power, re-immersion, and the type of developer used. However, several trends can be observed. For instance, the behavior of acetone-developed and re-immersed samples resembles an exponential decay function, while the OCT intensity curves for PGMEA-developed and re-immersed cubes exhibit oscillations with shifting local minima as the laser power increases.

This effect is associated with the non-sharp refractive index transition, characterized by a varying transition width between the photoresist and polymer. To quantitatively estimate the transition width and transition function, one could use the transfer matrix approach to calculate reflection from a smooth refractive index transition [111]. The transfer matrix method assumes that the transition medium between the photoresist and polymer can be represented as a stack of thin homogeneous films. It calculates reflection coefficients based on the characteristic matrix of this stratified medium. The principal scheme is illustrated in Figure 4.12. The wave in this scheme propagates from the photoresist medium with a refractive index of n_{pr} and passes through thin layers of the transition medium, each with a refractive index that depends on the z -position and is defined by a transition function as $n_{\text{tr}}(z)$. The final layer corresponds to the polymer medium with the constant refractive index of n_{pol} .

The characteristic matrix for normal incidence of non-magnetic loss-free thin film with a thickness d and refractive index $n_{\text{tr}}(z)$ is expressed as [111]

$$\mathbf{M}(z) = \begin{bmatrix} \cos(k_0 n_{\text{tr}}(z)d) & -\frac{i}{n_{\text{tr}}(z)} \sin(k_0 n_{\text{tr}}(z)d) \\ -i n_{\text{tr}}(z) \sin(k_0 n_{\text{tr}}(z)d) & \cos(k_0 n_{\text{tr}}(z)d) \end{bmatrix}, \quad (4.9)$$

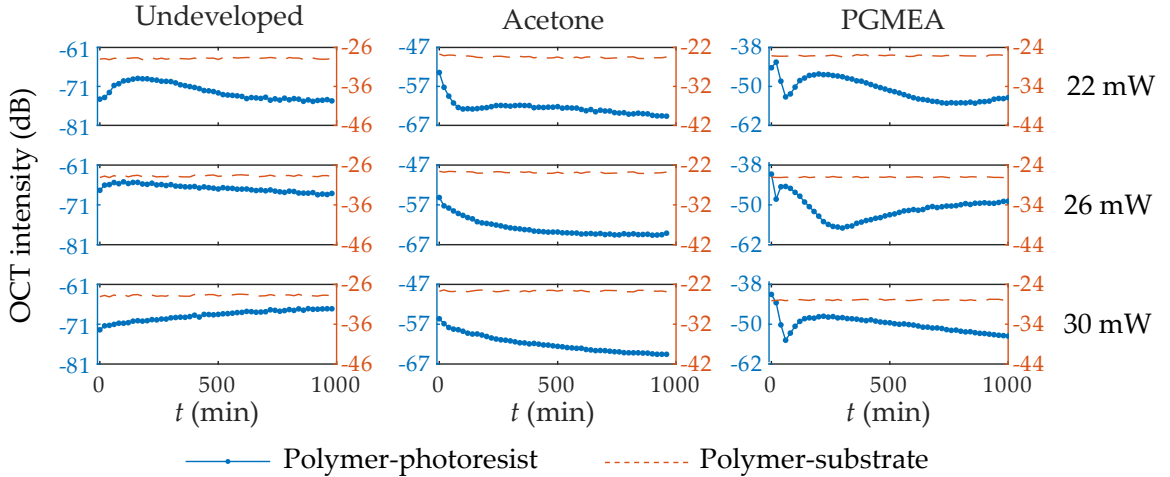


Figure 4.11: Temporal measurements of OCT intensity. Time-dependent OCT intensity measurements arranged in a 3×3 matrix. The columns of the matrix correspond to the printed cubes measured under three different conditions: printed and undeveloped samples (first column), cubes developed in acetone and then re-immersed (second column), and cubes developed in PGMEA and then re-immersed (third column). Changing-in-time measurements of the polymer-photoresist interface (blue curves) are plotted with the stable polymer-substrate interface (orange curves). Adapted from [105].

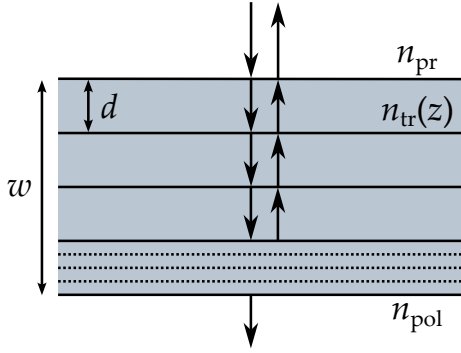


Figure 4.12: Scheme of the layered transition medium. The light passes through stratified transition medium, characterized by $n_{\text{tr}}(z)$, and is reflected at each interface within the medium. Boundary conditions are plane waves in the photoresist (n_{pr}) and in the polymer (n_{pol}).

where $k_0 = \frac{2\pi}{\lambda}$ is the free-space wavevector. The matrix for the stratified medium which is approximated as a pile of $N = w/d$ thin homogeneous films is then written as

$$\prod_{j=1}^N \mathbf{M}_j(z) = \begin{bmatrix} m_{11} & m_{12} \\ m_{21} & m_{22} \end{bmatrix}. \quad (4.10)$$

The final formula for the accumulated reflection after passing the stratified transition medium is written as

$$R = \left(\frac{(m_{11} + m_{12}n_{\text{pol}})n_{\text{pr}} - (m_{21} + m_{22}n_{\text{pol}})}{(m_{11} + m_{12}n_{\text{pol}})n_{\text{pr}} + (m_{21} + m_{22}n_{\text{pol}})} \right)^2. \quad (4.11)$$

Computationally, a MATLAB algorithm for reflection calculations [112] was used. Using the transfer matrix method, one could calculate reflection coefficients for different transition parameters and compare theoretic calculations with the experimental curves in Figure 4.11. For this purpose, the transition function that describes the dependency of n_{tr} on z was defined as

$$n_{\text{tr}}(z) = \begin{cases} n_{\text{pr}} & \text{for } z < z_0 - \frac{w}{2} \\ n_{\text{pr}} + \frac{n_{\text{pol}} - n_{\text{pr}}}{2} \times \left| \frac{z - (z_0 - w/2)}{w/2} \right|^e & \text{for } z_0 - \frac{w}{2} < z < z_0 \\ n_{\text{pol}} - \frac{n_{\text{pol}} - n_{\text{pr}}}{2} \times \left| \frac{z - (z_0 + w/2)}{w/2} \right|^e & \text{for } z_0 < z < z_0 + \frac{w}{2} \\ n_{\text{pol}} & \text{for } z > z_0 + \frac{w}{2} \end{cases}, \quad (4.12)$$

where e is the transition exponent and z_0 is the central z -position of the transition.

An example of transition refractive index curves generated by Equation 4.12 is presented in Figure 4.13a. Here and in the following calculations, z ranges from 0 to $5 \mu\text{m}$ with $z_0 = 2.5 \mu\text{m}$. The transition exponent e is used to smooth out the transition profile proportional to $\pm z^e$. For example, $e = 1$ corresponds to a linear transition.

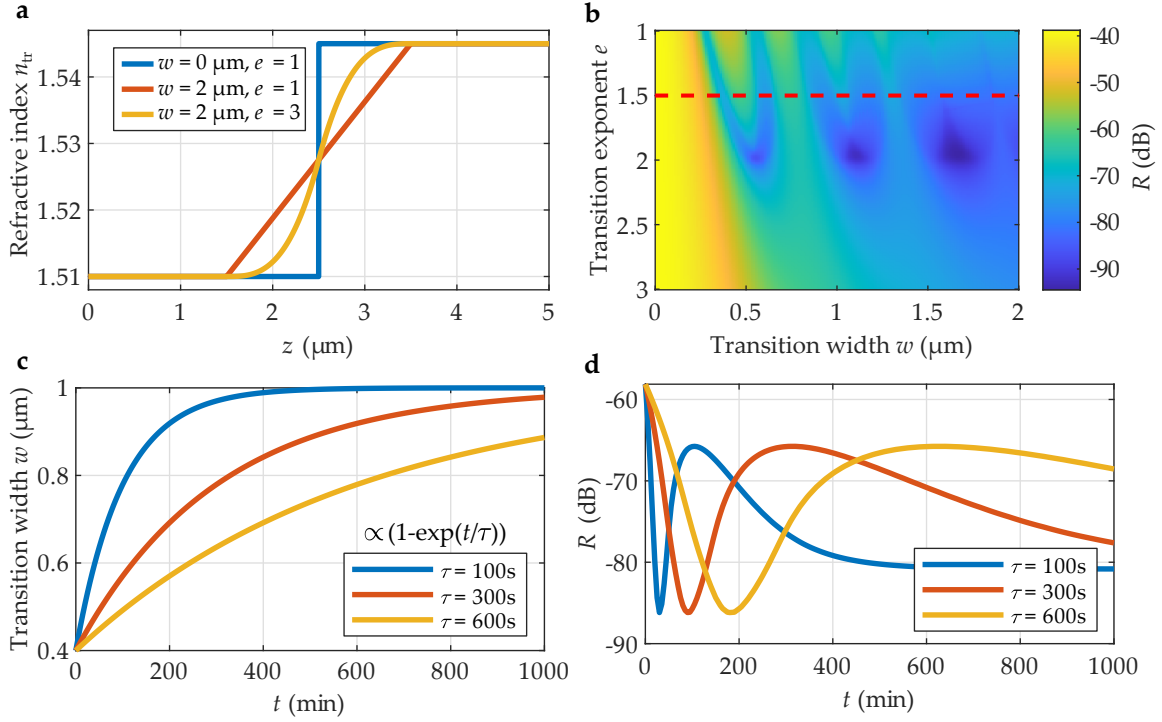


Figure 4.13: Transfer-matrix-based reflectivity calculations of the polymer-photoresist transition. **a** Example transition functions for refractive index calculated from Equation 4.12. **b** Computed distribution of reflectivity R depending on transition exponent e and transition width w . **c** Assumed time-dependent exponential behavior of transition width with different time constants. **d** Temporal reflectivity curves calculated from the transition width depicted on panel **c** and the exponent of $e = 1.5$ depicted as a red dashed line on panel **b**. The curves resemble experimental time-dependent behavior from Figure 4.11. Adapted from [105].

To properly compare the simulated results with the experiments, one should calculate the reflection coefficient R over different wavelengths since the used illumination source is far from monochromatic. Therefore, values of R were calculated for the SLD wavelengths $\lambda \in (845 - 135/2 \text{ nm}, 845 + 135/2 \text{ nm})$ with a step of 5 nm, and the final value was obtained by averaging. The obtained reflection distribution over different values of e and w is depicted in Figure 4.13b. Significantly, the distribution is non-uniform, displaying oscillating reflection as the transition width increases.

To further investigate this oscillatory behavior and compare it with experiments, time-dependent curves for transition width were simulated (Figure 4.13c). These curves were obtained by assuming the exponential increase from 0.4 to 1 μm with different exponential coefficients as depicted in Figure 4.13c. Finally, time-dependent reflection behavior was calculated from transition curves in panel **c**

and transition exponent $e = 1.5$ marked in panel **b**. The obtained reflection curves in [Figure 4.13d](#) resemble the oscillatory behavior of experimental OCT intensity in [Figure 4.11](#).

Thus, by applying the transfer matrix method, it is possible to estimate the transition width, which appears to be in the range of $1 \mu\text{m}$. A possible explanation of this effect is the diffusion of monomer molecules into the formed polymer matrix after printing. The rate of this diffusion changes depending on the used solvent after re-immersion into the photoresist, which explains different time-dependent behavior in [Figure 4.11](#). Further investigation of this effect is impossible since the precise transition function remains unknown and must be assumed.

4.3.3 In-situ Thickness Calculation

Despite the time-dependent variations in OCT intensity, the polymer-photoresist interface for the IP-Dip photoresist remains consistently detectable by OCT, even at the lowest intensity values. Thereby, this interface can always be measured, allowing for the deduction of the thickness of planar surfaces in printed microstructures in situ. For this purpose, a set of plates with different thicknesses ranging from $2 \mu\text{m}$ to $16 \mu\text{m}$, but a fixed side length of $30 \mu\text{m}$ was printed. The plates were printed together with supporting pillars with a height of $80 \mu\text{m}$ ensuring the OCT signal comes only from the polymer-photoresist interface and not from the substrate. The four of such printed plates are depicted in [Figure 4.14a](#). The example A-Scan taken from the center of the third plate (blue dot and gray line in [Figure 4.14a](#)) is depicted in [Figure 4.14b](#) as blue dots. Here, two peaks correspond to the top and bottom interfaces respectively. The absolute values of the peaks are not identical due to the smearing-out effect described in the previous subsection.

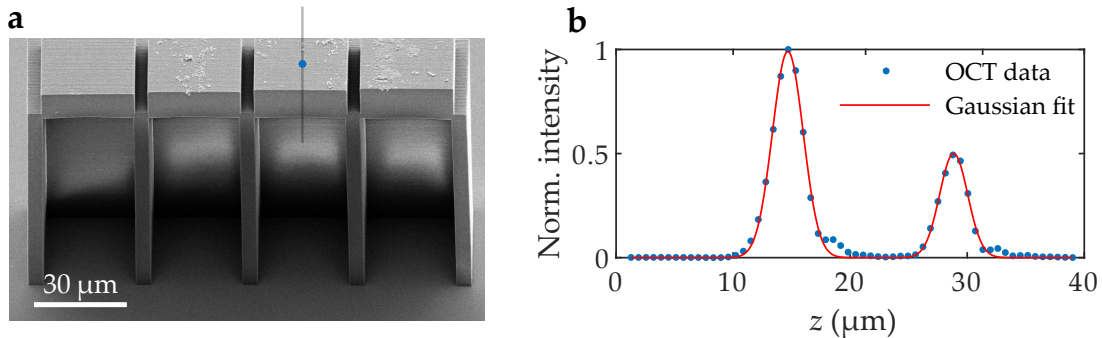
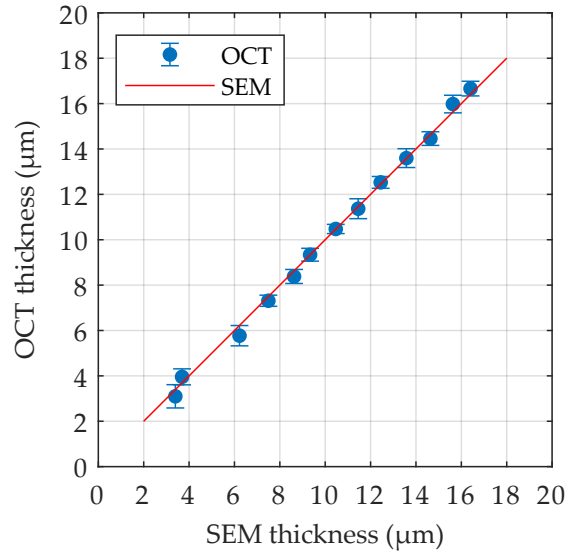


Figure 4.14: Printed plates for thickness evaluation. **a** Example transition functions for refractive index calculated from [Equation 4.12](#). **b** Computed distribution of reflectivity R depending on transition exponent e and transition width w . Adapted from [105].

Figure 4.15: Plate thickness measurements. Ex-situ SEM measurements of the developed plates are represented by the red line, while deviations of in-situ OCT measurements from these values are indicated by blue dots. Error bars are calculated as mean squared error (MSE) from the measurement area for each plate. Adapted from [105].



To measure the thickness of the plate, one should calculate the distance between the maxima of two peaks. This was accomplished by fitting the peaks with two Gaussians (red curve) and extracting the distance between them. To translate the optical path distance to real z -coordinate, the refractive index of polymerized IP-Dip, $n_{\text{pol}} = 1.545$, was used.

By employing the fitting procedure, all printed plates were measured, and their thicknesses were obtained by averaging over 600 A-scans for each plate. The comparison between in-situ thickness measurements obtained by OCT and ex-situ measurements from scanning electron microscope (SEM) data is presented in [Figure 4.15](#). The minimum resolved plate has a thickness of $3.1 \mu\text{m}$, which is close to the system's axial resolution of $2.7 \mu\text{m}$. Thinner plates were impossible to measure due to additional deviations of OCT signal arising from plate bending.

4.3.4 Shrinkage measurements

In addition to serving as an accurate in-situ thickness measurement tool, OCT can be utilized for assessing polymer shrinkage after development. For this purpose, large cuboids with a designed height of $120 \mu\text{m}$ and a side length of $50 \mu\text{m}$ were printed. To explore the influence of printing parameters, cuboids were printed with different laser powers ranging from 17.5 to 28 mW with a step of 3.5 mW and various slicing distances of 200 , 300 , and 400 nm . After evaluating the in-situ OCT height using the same procedure described in the previous subsection, the cubes were developed in acetone, and their ex-situ height was measured in air. Due to the requirement of immersion for the objective lens used, immersion oil was applied between the objective lens and the bottom part of the substrate, while the

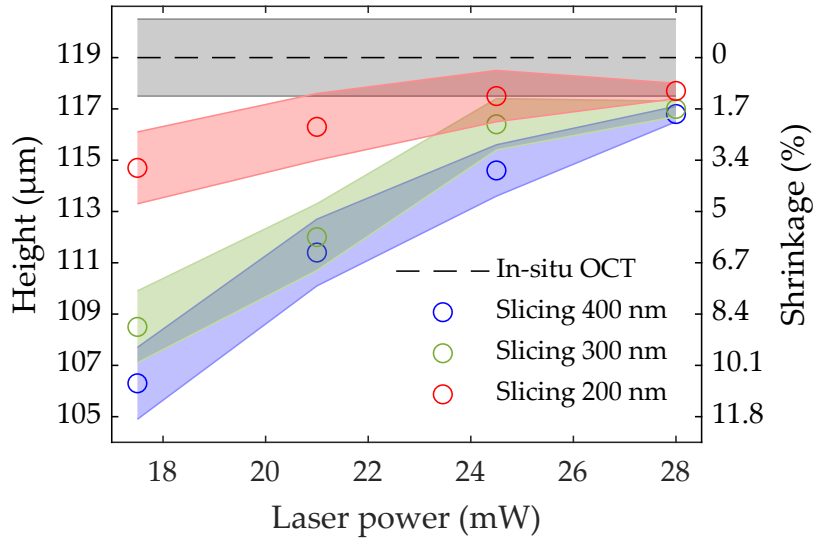


Figure 4.16: Shrinkage measurements of printed cuboids. Based on in-situ OCT measurements, all cuboids have approximately the same height of 119 μm within the gray error bar before development. After development cuboids were measured in air. Their height deviates due to shrinkage which depends on laser power and slicing. The shrinkage was calculated using Equation 2.8.

sample was positioned at the top of the substrate in air. The resulting shrinkage is measured according to Equation 2.8, and shrinkage measurements are presented in Figure 4.16. As observed from the plot, both writing parameters influence shrinkage values, reaching a minimum of 2% shrinkage. This effect is well-known for acrylate photoresists, because a higher polymerization degree, related to higher laser powers and smaller slicing distances, leads to smaller shrinkage [47]. This approach was also applied for estimating the shrinkage of unknown photoresists. Notably, OCT shrinkage measurements should be regarded as estimations rather than precise measurements, as the axial resolution of OCT is approximately 3 μm . Additionally, if the surface is no longer planar, the OCT signal drastically diminishes.

4.4 INSPECTION OF 3D-PRINTED GEOMETRIES

In-situ OCT provides valuable insights into printed microstructures based on planar interfaces. As demonstrated, it allows for measuring the polymer refractive index, assessing the diffusion of monomer into the polymer matrix, measuring thicknesses with accuracy comparable to SEM, and estimating shrinkage. However, the most crucial aspect of the in-situ tool lies in its capability for reconstructing 3D-printed geometries, extending beyond cuboids and plates with planar interfaces.

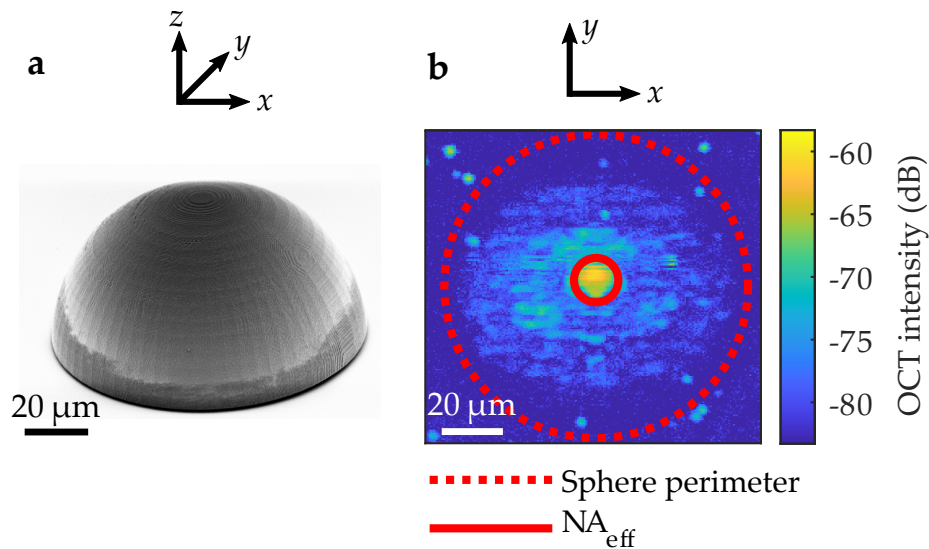


Figure 4.17: Imaging of a printed half-sphere. **a** SEM image of the half-sphere. **b** Maximum OCT intensity projection xy -map. The central yellow signal is associated with specular reflection coming from $\text{NA}_{\text{eff}} = 0.22$. The corresponding calculated area is shown in solid red. The dashed red area is a sphere perimeter. Since the structure lacks internal scattering, the area between the two circles exhibits minimal or no OCT intensity. Adapted from [105].

To validate this capability of in-situ OCT, a half-sphere with a radius of 50 μm was printed and imaged. The inspection of the printed half-sphere is depicted in Figure 4.17. As observed from the maximum intensity projection, the in-situ OCT intensity of the half sphere, the area of which is marked as a dashed red line, is almost undetectable (light blue area) with the only significant signal (yellow area) present in the center. This signal corresponds to the specular reflection out of the effective NA of the setup $\text{NA}_{\text{eff}} = 0.22$ marked as a solid red line. This observation suggests the absence of internal non-planar scattering from printed samples.

However, during printing and in-situ imaging of other geometries and using other printing strategies, it was observed that certain 3D structures could be detected. For example, all sidewalls were successfully reconstructed when imaging a cube printed with cross-directional hatching, with both slicing and hatching distances equal to 200 nm. In contrast, completely the same cube but printed with uni-directional hatching only shows the planar polymer-photoresist interface visible. Both reconstructions as well as ex-situ SEM images of both cubes are depicted in Figure 4.18. A detailed explanation of differences between cross- and uni-directional hatching strategies is given in section 2.2.

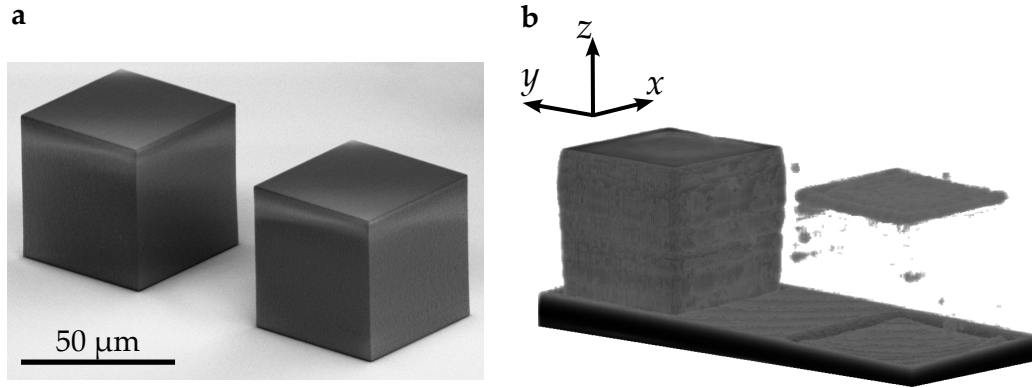


Figure 4.18: Imaging of printed cubes. **a** SEM image of two identical cubes. The only difference is cross-directional hatching for the top cube and uni-directional hatching for the bottom cube. **b** In-situ OCT reconstructions (iso-surfaces at -73 dB OCT intensity) of the two cubes showing drastic differences in OCT contrast. Axis arrows correspond to 25 μm in all directions. Adapted from [105].

Although there are no apparent differences between the two cubes in the SEM image, they exhibit completely different OCT intensities. The reason for this drastic change in 3D OCT reconstructions between two hatching directions is the additional internal scattering that occurs only in the cross-directional case. This scattering stems from inhomogeneities in the polymer refractive index between slices of printed objects. The nature of this scattering is very similar to the Bragg scattering appearing from constructive interference on periodic structures [111]. The maximum Bragg intensity is defined as the first diffraction order within the polymer with refractive index n_{pol}

$$\lambda_0 = 2n_{\text{pol}}d. \quad (4.13)$$

Here, d denotes the "grating period" or in the case of 3D-printed microstructures – the slicing distance. Thus, after calculating, $d \approx 280 \text{ nm}$ should be the slicing distance corresponding to the maximum Bragg intensity.

To further investigate the effect of Bragg scattering and OCT capability of reconstructing non-planar surfaces, the set of prisms with different slicing distances and cross-directional hatching was printed. The geometry of a prism is chosen because none of the surfaces of a prism leads to specular reflection along the optical axis. Therefore, the OCT signals of such structures are exclusively due to light scattering. Prism slicing distances were varied from 140 to 300 nm with a step of 20 nm, hatching distance was set to 200 nm for all structures. Additionally, the printing laser power was varied from 18 to 28 mW with a step of 1 mW. The resulting OCT reconstructions as well as SEM ex-situ images are illustrated in Figure 4.19. As predicted from Equation 4.13, the best reconstruction quality is observed for prisms printed with 280 nm slicing distance. However, interestingly, prisms with

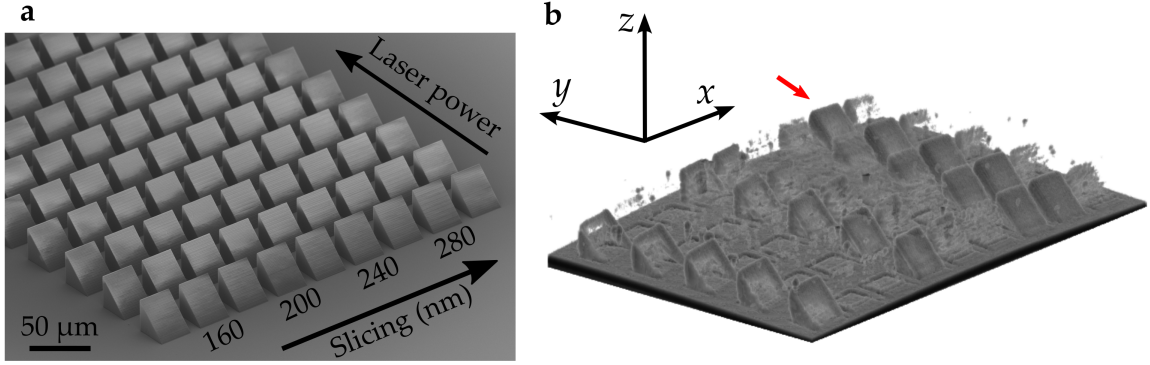


Figure 4.19: Imaging of printed prisms. **a** SEM image of the printed prism array. Slicing distances increase from left to right from 140 to 300 nm with a step of 20 nm. Printing laser power increases from bottom to top starting from 18 mW with a step of 1 mW. **b** In-situ OCT reconstruction (iso-surfaces at -64 dB OCT intensity) of the same prism array showing the difference in OCT reconstruction quality depending on the slicing distance used. Axis arrows correspond to 100 μm in all directions. The red arrow highlights the prism column with 280 nm slicing distance, which has the best reconstruction quality and related to the central Bragg wavelength as calculated from Equation 4.13. Adapted from [105].

slicing distances of 140, 200, and 260 nm are also partially reconstructed. The laser power has no apparent influence on 3D reconstructions.

The scattering signal originating from prisms printed with slicing distances other than the first-order Bragg scattering slicing distance can be attributed to two reasons. First, the Equation 4.13 considers only the central wavelength of the SLD λ_0 . However, in reality, the SLD has a bandwidth of 135 nm, which broadens the range of slicing distances d for maximum intensity. Second, the slicing distance may not be the sole factor describing the periodicity of refractive index in the z -direction. Additional refractive index inhomogeneities, such as the proximity effect, voxel size, and printing deviations of any kind, also affect the distribution of refractive index in the z -direction.

To estimate the range of these inhomogeneities, the modulated refractive index n_{mod} was simulated for further calculating the reflectivity using the transfer matrix approach. Refractive index modulations were simulated as a sum of two sine functions as

$$n_{\text{mod}} = 1.545 + 5 \cdot 10^{-4} \left(\sin(2\pi z/d) + \frac{1}{3} \sin(\pi z/d) \right), z \in [0 \mu\text{m}, 5 \mu\text{m}]. \quad (4.14)$$

Here, the first sine function with the period of d and an amplitude of 5×10^{-4} corresponds to the periodic refractive index in the z -direction and the second sine

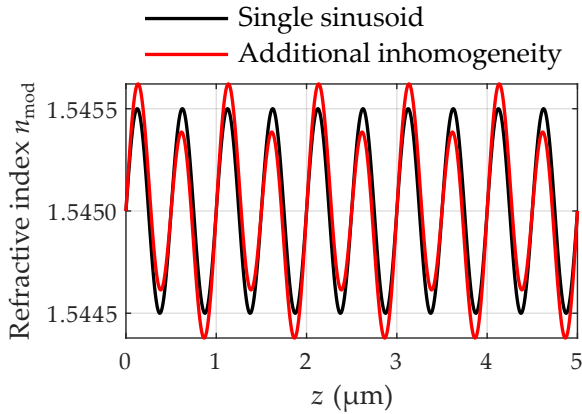


Figure 4.20: Periodic refractive index plots. Exemplary refractive index profiles calculated using Equation 4.14 with a slicing distance of $d = 500$ nm. The black curve is calculated from the first sine function in Equation 4.14 and represents a single periodic refractive index. The red curve is obtained by a sum of two sine functions and represents additional refractive index modulations. Adapted from [105].

function generates additional inhomogeneities with an amplitude on the order of 10^{-5} . The refractive index plots of a single sinusoid with a period of $d = 500$ nm (black curve) and the sum of two sinusoids with the same period (red curve) are presented in Figure 4.20.

The reflectivities of periodic refractive indices for both cases (single sinusoid and additional modulation) were calculated using a transfer matrix approach for each value of slicing distance/period from 100 nm to 700 nm with a step of 10 nm and wavelength from 780 to 910 nm with a step of 10 nm. The resulting reflectivity distributions are presented in Figure 4.21.

It is clearly seen that both cases exhibit a strong reflectivity peak at approximately 280 nm of the slicing distance/sine period. After averaging reflectivity over all wavelengths, the single sinusoid case (Figure 4.21b) has a reflectivity peak with a width of approximately 40 nm centered around 270 nm. This result explains the good reconstruction quality of prisms with a slicing distance of 260 nm. After adding modulations to the periodic refractive index, the second reflectivity peak at approximately 140 nm appears (Figure 4.21d). The secondary peak also explains the capability of OCT reconstruction for the prisms printed with a 140 nm of slicing distance.

Thus, the modulated refractive index in the z -direction is the prime reason for Bragg scattering, leading to good reconstruction quality for some of the prisms with certain slicing distances. Therefore, one could infer that any OCT signal observed might only originate from planar surfaces. The fact that one sees other surfaces indicates optical imperfections in the printed specimens. These imperfections may deteriorate the performance of the printed device, depending on the application. Hence, for printing 3D architectures with high quality, ideally, no internal OCT signal should be detected at all.

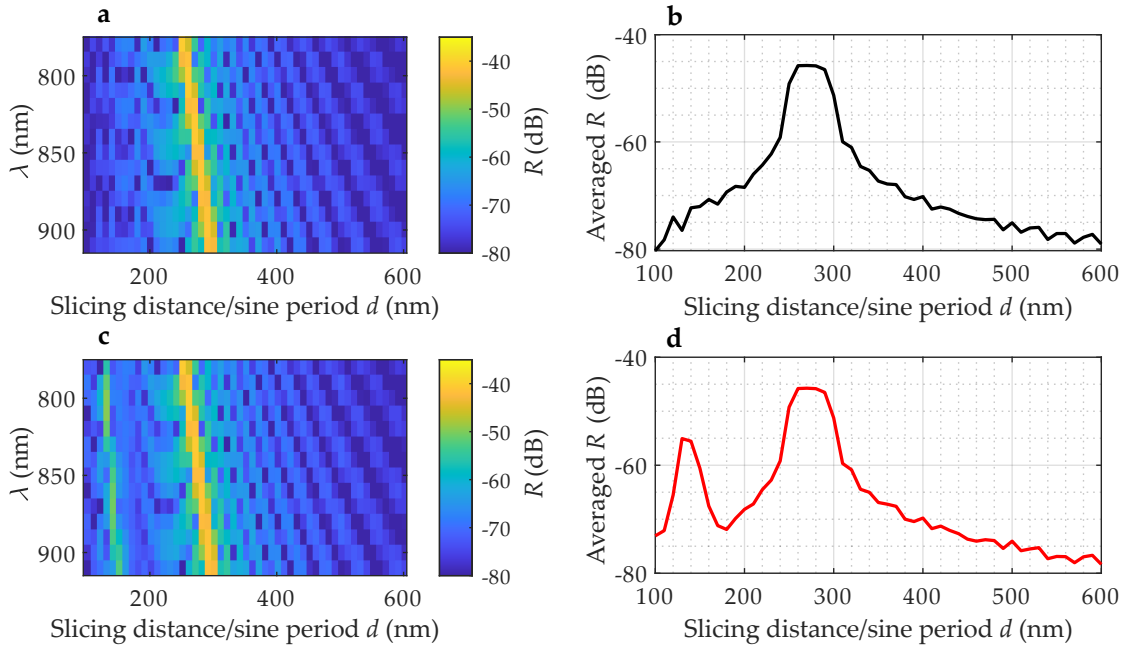


Figure 4.21: Transfer matrix calculations of Bragg scattering signal. **a** Reflectivity distribution over SLD wavelengths and slicing distance/sine period d after transfer-matrix calculations. These calculations utilize only the first sine function in Equation 4.14 for the refractive index function. **b** Wavelength-averaged reflectivity from panel **a**. **c** and **d** The same as for panels **a** and **b** but calculated for the whole refractive index function in Equation 4.14. Adapted from [105].

Finally, utilizing the effect of Bragg scattering, the 3D structures of a buckyball and benchy boat [113] with slicing of 280 nm and cross-directional hatching of 200 nm were printed and in-situ imaged using OCT. The OCT reconstructions together with ex-situ SEM images are presented in Figure 4.22. Notably, the OCT contrast appears due to periodic refractive index arising from cross-directional hatching and not from internal diffuse scattering of structures.

4.5 CONCLUSION

This chapter discussed using OCT as an in-situ characterization tool for 3D-printed microstructures. The custom-built OCT setup has the following parameters: an axial resolution of 2.7 μm and lateral resolution of 1.9 μm , 40 μs acquisition time for one A-scan (equivalent to a frame rate of 25 kHz), and 105 dB sensitivity or signal-to-noise ratio for a single experiment. The developed OCT system utilizes the typical objective lens used for 3D printing and can be directly integrated into the printing setup along the same optical axis.

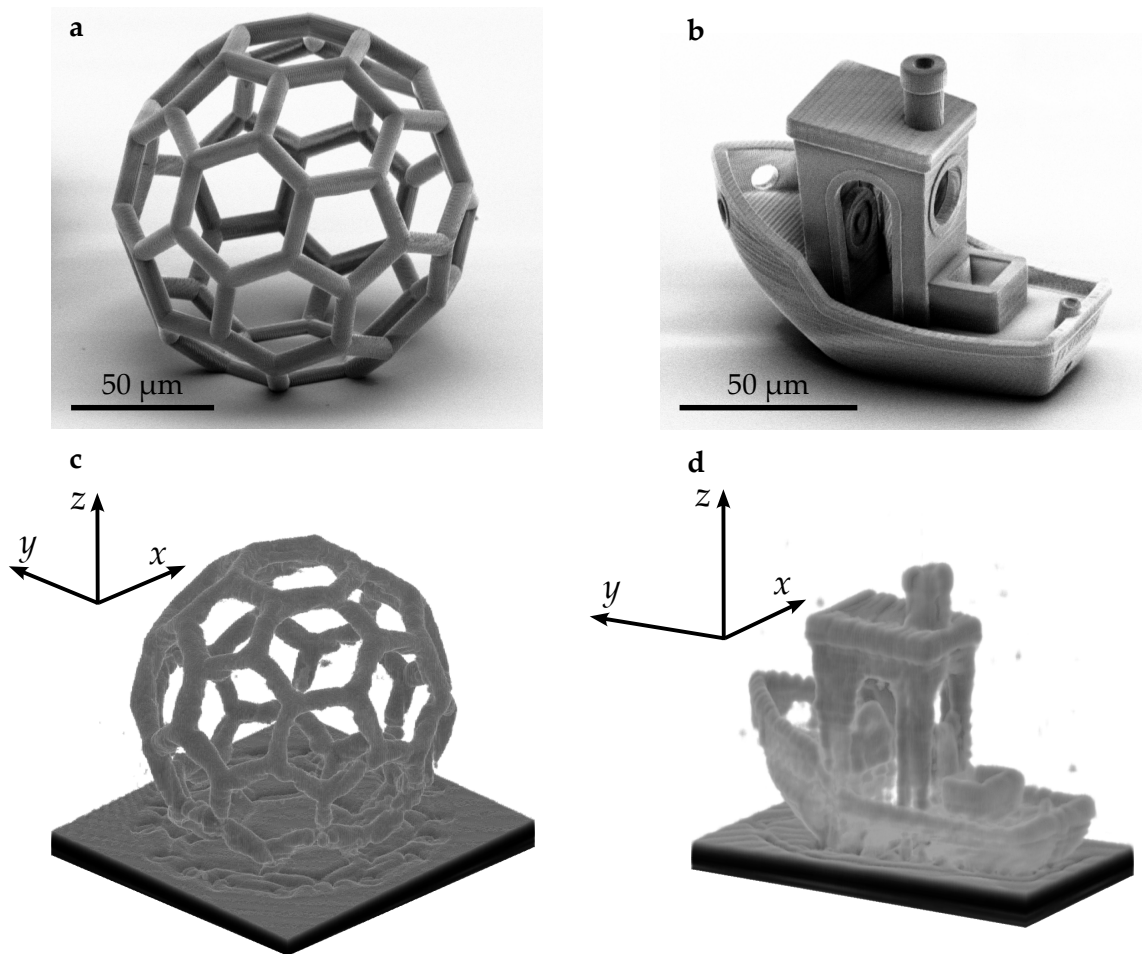
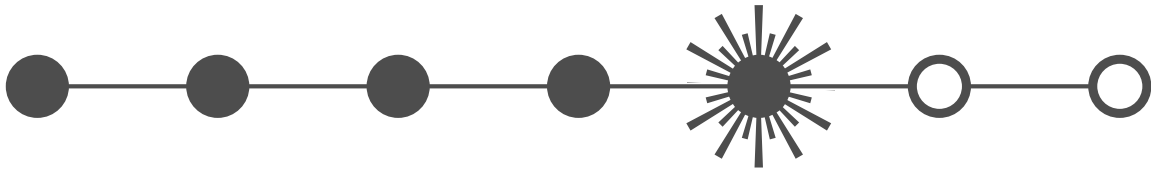


Figure 4.22: OCT reconstructions of complex geometries based on Bragg scattering. **a** and **b** Ex-situ SEM images of a printed buckyball and benchy boat. **c** and **d** In-situ OCT reconstructions of printed structures (iso-surfaces at -71 dB and -53 dB OCT intensity, respectively). Axis arrows correspond to $50\ \mu\text{m}$ for each direction. Adapted from [105].

Among the shown applications of in-situ OCT are homogeneity inspection of the photoresist volume, polymer refractive index estimation, qualitative demonstration of monomer diffusion into the polymer matrix, thickness measurement of planar surfaces, shrinkage estimation, and detecting inhomogeneities in the structure's refractive index. These applications make OCT an attractive in-situ characterization tool. However, for the primary purpose of in-situ imaging tools, specifically the general imaging of 3D-printed microstructures, OCT proves inadequate. This is because the internal scattering of the printed structures is insufficient for proper reconstruction, unless they exhibit Bragg scattering, which is associated with structural imperfections. Therefore, alternative methods of in-situ diagnostics had to be developed, as will be presented in the following chapters.

5 Chapter 5

IN-SITU QUANTITATIVE PHASE IMAGING (QPI)



This chapter presents a quantitative phase imaging apparatus integrated into a commercial laser printer. I will explain the main principle for calculating the optical path length of printed specimens using in-situ microscopic defocused images captured immediately after printing. Consequently, the refractive index and shrinkage of the printed structures will be derived, and the topography of various printed micro-optical elements will be measured and presented.

5.1 QPI INTEGRATION PRINCIPLE

5.1.1 Introduction

Phase shifts that light acquires after transmission through the printed specimen carry important information about the sample's refractive index and height. These phase shifts are associated with the sample's optical path length and are expressed as

$$\Delta\phi_{\text{in-situ}}(\mathbf{r}) = \frac{2\pi\Delta n h(\mathbf{r})}{\lambda_0}, \quad (5.1)$$

where $\mathbf{r} = (x, y)$, Δn is the refractive index difference between polymer and photoresist, $h(\mathbf{r})$ is the height distribution of the printed sample, and λ_0 is the central wavelength of the illumination source. For the sake of simplicity, the dependence of the refractive index on the spatial coordinates in Equation 5.1 was omitted, since it is assumed that the refractive index of the polymer within a printed structure is constant.

As outlined in section 3.5, these phase shifts or phase differences can be obtained by different interferometric and non-interferometric means. Particularly, one can collect focused and defocused microscopic intensity images and reconstruct the phase by solving the transport-of-intensity equation (TIE), which is written for zero-absorption samples as [86]

$$-\frac{k}{I_0(\mathbf{r})} \frac{\partial I(\mathbf{r})}{\partial z} = \nabla^2 (\Delta\phi(\mathbf{r})), \quad (5.2)$$

where $k = 2\pi n_{\text{pr}}/\lambda$, n_{pr} denotes the refractive index of photoresist, and $I_0(\mathbf{r})$ denotes the in-focus intensity. From the experimental perspective, solving the TIE requires only the recording of intensity images at different z -positions to calculate the axial intensity derivative $\frac{\partial I(\mathbf{r})}{\partial z}$. Consequently, a laser printer, which includes an optical microscope with an equipped motorized z -stage and a camera for recording bright-field intensity images (Figure 2.4), can be adapted for both printing the sample and simultaneously performing in-situ reconstruction of its phase difference, with only minor modifications to the illumination path.

5.1.2 QPI Modification of the Laser Printer

During the derivation of the TIE (Equation 3.24–Equation 3.29), it was assumed that the illumination source should be monochromatic and spatially coherent. However, in practice with optical microscopes, the requirements for both spatial and temporal coherence are not stringent. In the QPI community, a quasi-monochromatic source is considered adequate for accurate phase extraction using

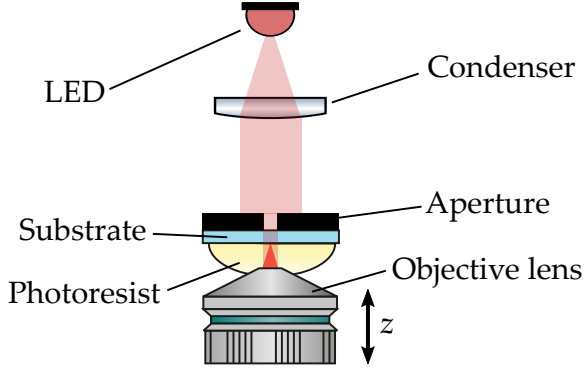


Figure 5.1: Modified illumination path for in-situ QPI. The Nanoscribe PPGT illumination path was modified with a collimator lens and an aperture to provide the spatial coherence required for proper phase imaging. The z -stage with the attached objective lens was moved to obtain defocused images.

TIE [86]. Consequently, the standard LED illumination of a laser printer (central wavelength $\lambda_0 = 630$ nm, bandwidth $\Delta\lambda = 17$ nm) meets this condition. Furthermore, it has been established that partial spatial coherence is also acceptable for TIE, without degrading the quality of phase retrieval [114]. To achieve a sufficient degree of spatial coherence, an additional circular aperture (Thorlabs P900K) with a diameter of $900 \mu\text{m}$ was placed directly onto the sample holder. Additionally, to guarantee beam parallelism, the LED light was collimated using an aspheric condenser lens. It was also found that using the condenser lens is optional, and the same illumination conditions can be achieved without using it by elevating the LED by 10-15 cm from the sample holder. The modified illumination path of the Nanoscribe PPGT printing setup, used for both printing and in-situ QPI, is depicted in Figure 5.1. The photograph of the optical microscope of the Nanoscribe PPGT printing setup, featuring the modified illumination path and the inserted aperture, is presented in Figure 5.2.

5.1.3 Phase Retrieval Algorithm

To solve the TIE and reconstruct the 2D phase difference of the printed sample, one needs to take a certain amount of defocused images, estimate the axial intensity derivative, and solve the Poisson equation in the frequency domain (Equation 3.31).

Generally, only two defocused images captured around the in-focus plane are sufficient to calculate the intensity derivative using the symmetric derivative approximation [115]

$$\frac{\partial I(\mathbf{r})}{\partial z} \approx \frac{I_{+\Delta z}(\mathbf{r}) - I_{-\Delta z}(\mathbf{r})}{2\Delta z}, \quad (5.3)$$

where $I_{-\Delta z}(\mathbf{r})$ and $I_{+\Delta z}(\mathbf{r})$ are 2D intensities of images captured below and above the in-focus plane respectively. This approximation is mathematically valid in

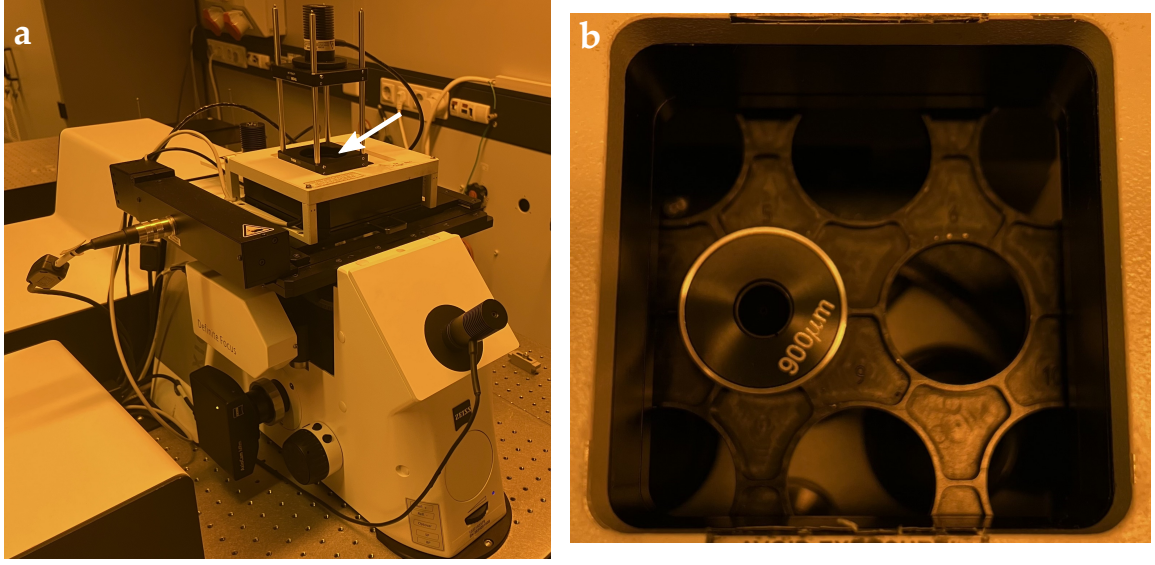


Figure 5.2: Modified illumination of the Nanoscribe PPGT. **a** The optical microscope of the printing setup. The white arrow highlights illumination modification shown in Figure 5.1. **b** The circular aperture was inserted directly onto a sample holder. The photograph is taken at the position of the white arrow in panel **a**.

the limit of small defocus distances Δz . However, experimentally, the derivative evaluation becomes unstable when the defocus distance is too small. This instability arises due to the low-frequency noise and quantitation errors in the imaging process. On the other hand, increasing the defocus distance provides a better signal-to-noise ratio, but introduces non-linearities due to the breakdown of the linear approximation.

Alternatively, one can use multiple equally spaced defocused planes to estimate the derivative more accurately. The intensity derivative can then be represented by the linear combination as [116]

$$\frac{\partial I(\mathbf{r})}{\partial z} \approx \sum_{j=-k}^k \frac{a_j I_j \Delta z(\mathbf{r})}{\Delta z}, \quad (5.4)$$

where $j = -k, \dots, 0, \dots, k$ is an image number with minus (plus) denoting images below (above) the in-focus plane, and 0 corresponds to the in-focus plane. Here, coefficients a_j can be defined differently depending on the numerical algorithm for derivative estimation. For example, Soto and Acosta [117] defined the "noise-reduction finite difference" formula with coefficients

$$a_j = \frac{3j}{k(k+1)(2k+1)}. \quad (5.5)$$

Eventually, this approach was unified by Zuo et al. [118], who demonstrated that Equation 5.4 can be interpreted through the perspective of digital filtering using

Savitzky-Golay differentiation filters (SGDFs) of varying degrees. In other words, the intensity derivative can be estimated using Equation 5.4, where coefficients a_j are SGDF polynomials with different degrees. Generally, SGDF is "an equivalent convolution solution for differentiation estimation by least-squares polynomial fitting" [118]. The phase reconstruction by using adaptive-degree SGDF is called optimal frequency selection and is implemented in three steps as described and implemented in [118]:

1. Intensity derivatives $\frac{\partial I(\mathbf{r})}{\partial z}$ are estimated using Equation 5.4, where a_j are SGDFs with different degrees.
2. The sample phase is reconstructed for every estimated intensity derivative by solving TIE (Equation 3.31).
3. The final phase is recombined from optimal frequency components of calculated phase distributions using band-pass filters for each degree.

5.1.4 Workflow

The workflow of in-situ QPI is depicted in Figure 5.3. First, the sample, for example, a half-sphere, was printed using the Nanoscribe PPGT. After that, the z -stage was moved to the in-focus plane, where the intensity contrast between the printed structure and the photoresist was minimal. The distance by which the z -stage was moved to reach the in-focus plane was equal to half the height of the printed structure plus the shift between the printing plane and the in-focus plane. Consequently, the z -stage was moved by $-60 \mu\text{m}$, and total $N = 61$ images were taken at equidistant intervals with a step size of $\Delta z = 2 \mu\text{m}$. Thus, 30 images were taken below and 30 above the in-focus plane, plus one image that corresponds to the in-focus plane itself. The exposure time of a single frame was 1.4 ms for the $25\times/\text{NA}0.8$ objective and 8 ms for the $63\times/\text{NA}1.4$ objective lens.

As a next step, the obtained image stack was used to calculate the axial intensity derivative and solve the TIE by applying the optimal frequency selection principle using MATLAB code similar to that implemented in [118]. The calculation of the final phase difference by this method takes approximately 5-30 seconds depending on the image size in the xy -direction. The entire experimental procedure requires approximately 20 seconds, with its duration constrained by the NanoWrite software, which controls both the printing and recording processes. However, faster data acquisition potentially reducing the time to less than 1 second seems feasible, assuming direct access to the printer hardware is available.

The lateral resolution of the final phase is defined by Abbe's resolution limit (or imaging pixel size), which is 225 nm for the $63\times/\text{NA}1.4$ objective and 400 nm for

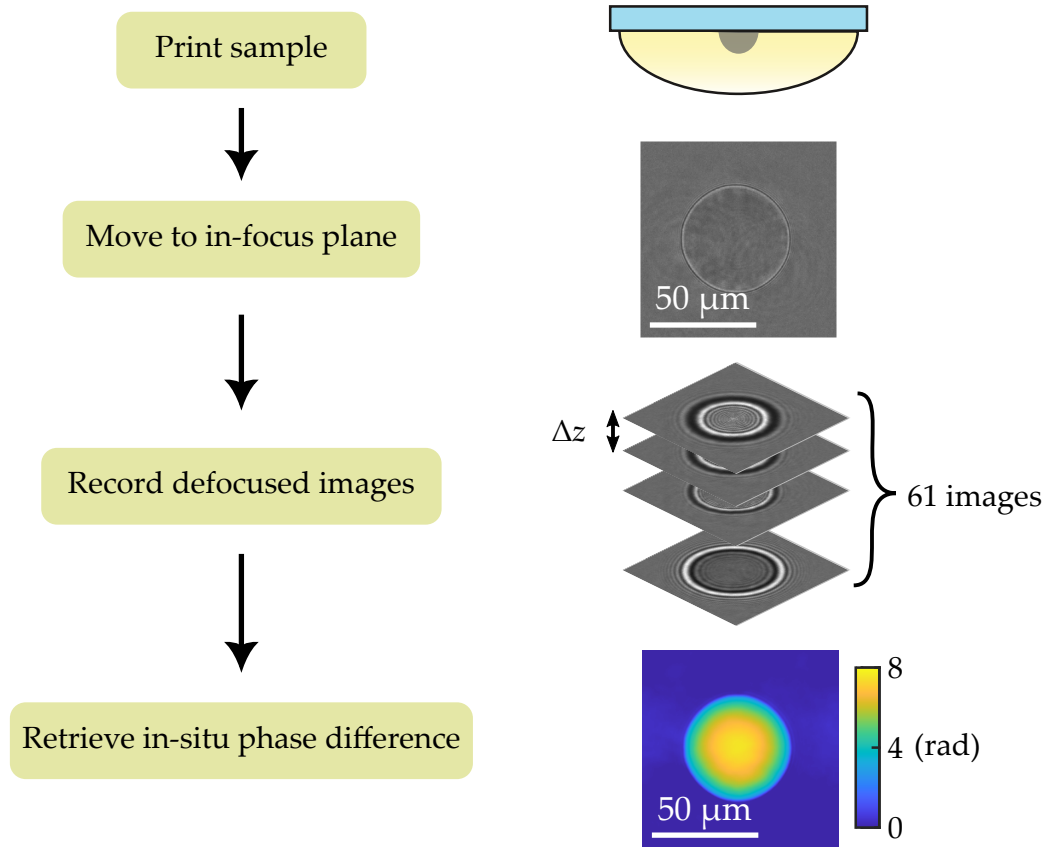


Figure 5.3: Workflow for in-situ QPI. Stages performed for in-situ QPI experiments based on the example of a printed half-sphere. The Nanoscribe PPGT setup is used for both printing and in-situ imaging.

the 25 \times /NA0.8 objective. The axial resolution of the method is defined by the phase sensitivity [86] and reaches less than 100 nm for the printed specimens.

5.2 REFRACTIVE INDEX AND SHRINKAGE DETERMINATION

By recovering the phase difference, one calculates the product of the refractive index difference and the topography of a printed structure. There are two main ways of applying QPI to extract important information about printed samples. The first approach is to calculate 2.5D structure topography $h(\mathbf{r})$ using the known refractive index difference. The second approach is to determine the refractive index difference when the structure topography is already known. The latest approach is particularly important in cases where the polymer refractive index is not known and varies with writing parameters. Therefore, one should first extract information about polymer refractive index and then apply this knowledge to measure the topography.

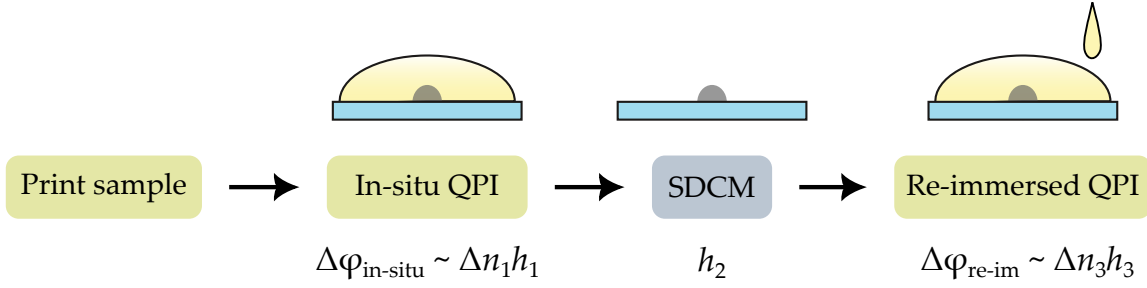


Figure 5.4: Refractive index determination procedure for printed specimens. The scheme depicts various measurement steps along with the corresponding measured quantities for each experiment. Spinning disk confocal microscope (SDCM) measurements were performed in ambient air after the development step, and re-immersion was done in the same photoresist. Yellow blocks correspond to operations performed using the Nanoscribe PPGT.

5.2.1 Determination Procedure

To define the refractive index, additional measurements had to be performed. The measurement flowchart is shown in [Figure 5.4](#). Initially, samples were printed and their in-situ phase differences $\Delta\phi_{\text{in-situ}}$ were measured using the procedure depicted in [Figure 5.3](#). Afterward, the samples were developed in PGMEA for 15 minutes followed by a rinse in isopropyl alcohol for 5 minutes. After the development procedure, their ex-situ height profiles h_2 were measured in ambient air using a spinning disk confocal microscope (SDCM, MarSurf CM expert). Finally, the samples were re-immersed in the same photoresist, and their re-immersed phase differences $\Delta\phi_{\text{re-im}}$ were measured following the same methodology as for the in-situ phase.

The printed samples have different properties at various stages: a refractive index difference of Δn_1 and height h_1 after printing and during in-situ imaging, Δn_2 and h_2 after development and during ex-situ height measurements, and Δn_3 and h_3 following re-immersion. In order to derive the refractive index difference from the optical path difference certain assumptions are required. The first assumption is the absence of changes in the refractive index difference throughout all measurements, meaning $\Delta n_1 = \Delta n_2 = \Delta n_3 = \Delta n$. This assumption is reasonable for the acrylate photoresists used in this study and is supported by the consistency between in-situ and ex-situ measured refractive indices, as detailed in [section 4.3](#). The second assumption is that the height of the developed structure remains unchanged after re-immersion, meaning $h_2(\mathbf{r}) = h_3(\mathbf{r})$.

Taking these two assumptions into account, one can finally derive the formula for

the refractive index difference

$$\Delta n = \frac{\Delta\phi_{\text{re-im}}(\mathbf{r})\lambda_0}{2\pi h_2(\mathbf{r})}. \quad (5.6)$$

Furthermore, the relative polymer shrinkage occurring after development can be calculated as a simple relation between in-situ and re-immersed phases

$$S = 1 - h_2/h_1 = 1 - \Delta\phi_{\text{re-im}}/\Delta\phi_{\text{in-situ}}. \quad (5.7)$$

5.2.2 Cuboid Array

Experimentally, the easiest way of applying the refractive index determination approach is to print and inspect specimens that have planar surfaces, for example, cuboids. Figure 5.5 demonstrates reconstructed in-situ and re-immersed phase maps as well as ex-situ SDCM measurements of a small cuboid (block) array consisting of six cuboids printed with a different laser power each. The laser power varied from 10 to 22.5 mW in steps of 2.5 mW, covering a laser power range from polymerization to overexposure thresholds. The array was printed using the Nanoscribe IP-S photoresist and the $25\times/\text{NA}0.8$ objective lens. The designed size of each cuboid was $40 \times 10 \times 3 \mu\text{m}^3$. The array was printed with a focus scanning speed of 2.5 cm/s.

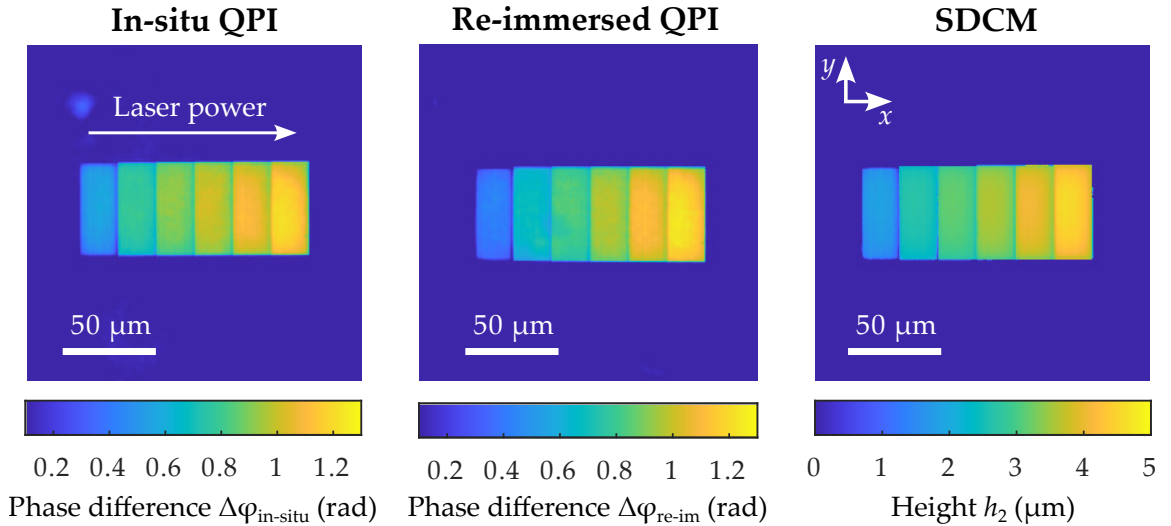


Figure 5.5: Measurements of IP-S cuboids printed with different laser powers. First two panels showcase phase differences measured in situ (left panel) and after development, followed by re-immersion in the same photoresist (middle panel). The last panel demonstrates ex-situ height topography measured by SDCM after development in air. Adapted from [119].

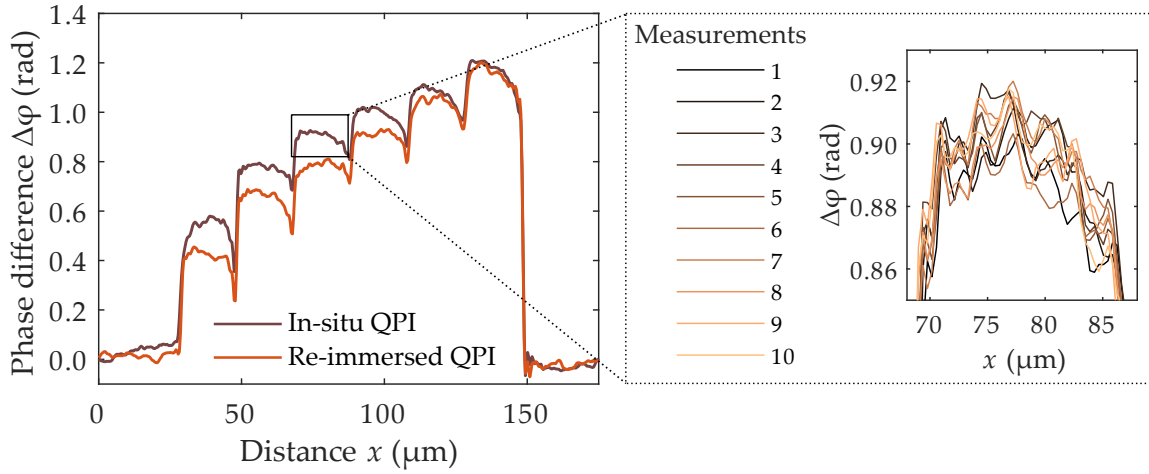


Figure 5.6: Phase difference profiles from Figure 5.5. Phase difference profiles taken along the middle of the cuboid array for in-situ QPI (brown curve) and QPI after development and re-immersion in the same photoresist (orange curve). The reproducibility test consisting of ten independent in-situ phase difference measurements of the third cuboid shown on the right. Adapted from [119].

As observed in Figure 5.5, lower laser powers result in smaller heights because the accumulation dose effect is less pronounced, which consequently reduces the phase differences. Notably, this reduction in phase differences is also associated with a decrease in the refractive index of the printed structures.

A further detailed comparison between in-situ and re-immersed reconstructed phase profiles taken along the middle of the cuboid array is presented in Figure 5.6. These profiles illustrate the differences in the phase before development (represented by the brown curve) and after development, followed by re-immersion (represented by the orange curve). The differences between the two curves are more pronounced for lower laser powers and stem from the height change due to polymer shrinkage, as derived in Equation 5.7. Additionally, the stability of the phase reconstruction was verified by measuring the phase profile of one of the blocks ten times, resulting in a relative standard deviation of less than 1%.

Finally, the refractive index of the polymer and the relative shrinkage of each cuboid can be calculated using the measured phase and height values, as detailed in Equation 5.6 and Equation 5.7. To additionally inspect the other photoresist, the same cuboids were printed from Nanoscribe IP-Dip and the $63\times/\text{NA}1.4$ objective lens. The printing laser power for this case varied from 12.5 to 20 mW with a step of 1.5 mW. The IP-Dip array was measured using the same procedure as the IP-S array. The calculated data for both photoresists are presented in Figure 5.7. To determine the polymer refractive index, the refractive index values of liquid

IP-S and IP-Dip, which are equal to $n_{\text{IP-S}} = 1.483$ [40] and $n_{\text{IP-Dip}} = 1.518$ [41] at $\lambda_0 = 630$ nm were used for calculations. The errors were determined as the MSE of the measured values across each cuboid.

The obtained refractive index values were compared with known ex-situ data from the literature. Since no data have been published on the dependency of the IP-S polymer refractive index on printing laser power, only the known value for

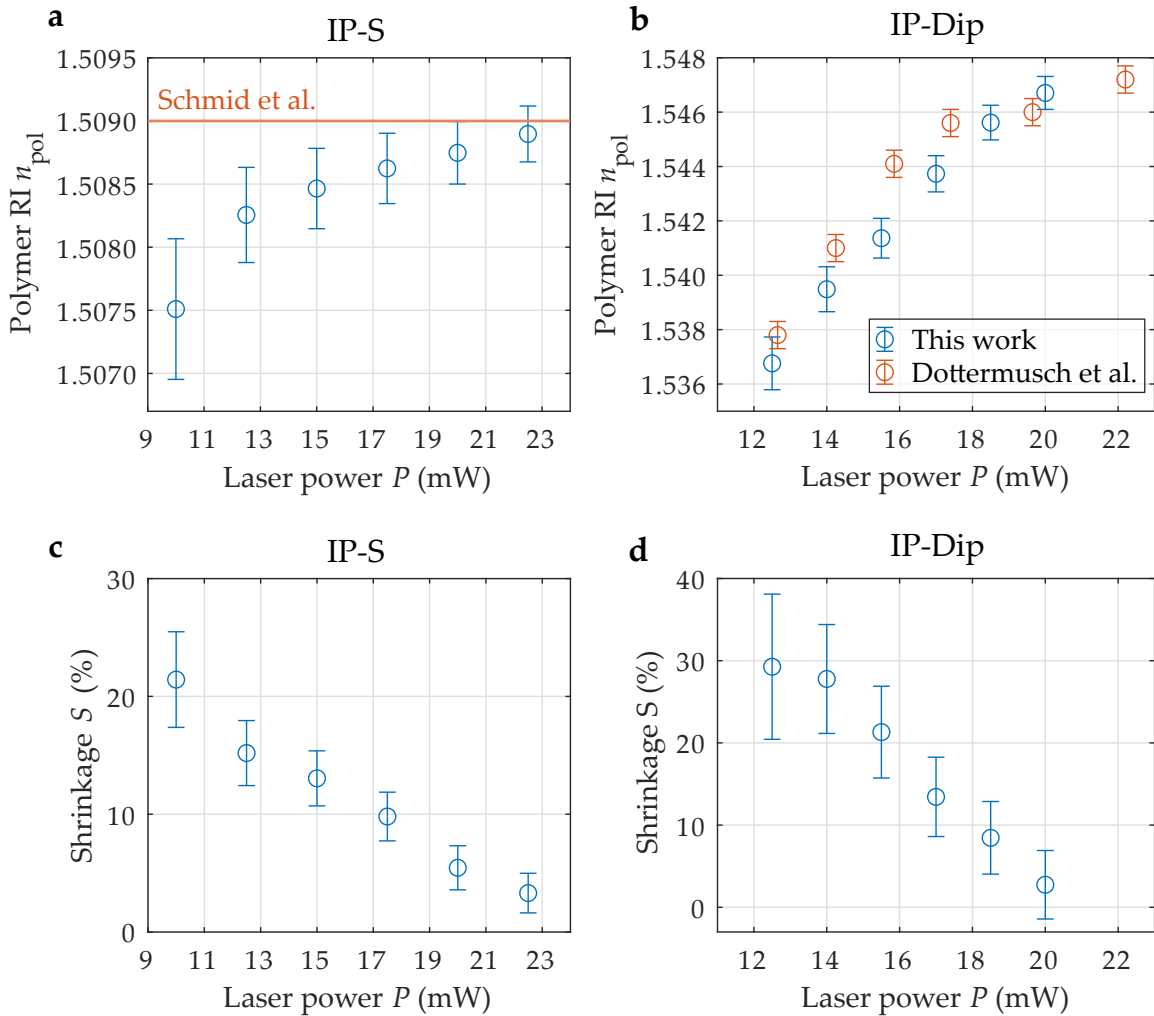


Figure 5.7: Polymer refractive index and shrinkage as functions of writing laser power for IP-Dip and IP-S. **a** Polymer refractive index (RI) calculated from Equation 5.6 for the IP-S cuboids from Figure 5.5 and the reference value for the fully polymerized volume taken from [39]. **b** Calculated polymer RI values for the IP-Dip cuboids and reference values taken from [42]. **c** Relative shrinkage calculated using Equation 5.7 for the IP-S cuboids from Figure 5.5. **d** Relative shrinkage for the IP-Dip cuboids. Error bars calculated from MSE for each cuboid. Adapted from [119].

fully polymerized IP-S, $n_{\text{IP-S}}^{\text{full}} = 1.509$, taken from [39] is plotted as an orange line in Figure 5.7a. As observed, the measured refractive index for this photoresist approaches the fully polymerized value but does not completely reach it due to overexposure at higher laser powers. For the IP-Dip data, such dependency was measured ex situ by Dottermusch et al. [42]. Their measurements were taken using a wavelength of 637 nm, which closely matches the wavelength of $\lambda_0 = 630$ nm used in this work. Therefore, the IP-Dip values measured through the QPI approach can be directly compared with the ex-situ values from the literature. The ex-situ measured IP-Dip refractive indices from [42] are represented by orange points in Figure 5.7b. It is evident that these values are in good agreement with those measured by QPI (blue points), showing an almost linear increase with increasing laser powers.

The calculated shrinkage values for both photoresists are shown in Figure 5.7c and d and are consistent with the previously reported shrinkage of Nanoscribe photoresists [47]. The QPI method of shrinkage measurement was also effectively applied for unknown photoresists [120]. In addition, shrinkage values for IP-DIP closely match the in-situ OCT shrinkage estimations for much larger cuboids (Figure 4.16). However, the QPI method for calculating shrinkage is both faster and more accurate than OCT. This is because OCT is highly sensitive to the planarity of the surfaces being measured and can fall short in accuracy when this condition is not strictly met.

5.3 TOPOGRAPHY OF PRINTED MICRO-OPTICS

After the determination of the refractive index difference, one can print many different 2.5D micro-optical structures to measure their topography/height distribution using Equation 5.1. In the following, different micro-lenses, diffractive optical elements (DOEs), and phase plates are analyzed using the in-situ QPI approach.

5.3.1 Micro-lens

A micro-lens featuring an aspheric design was printed using the IP-S photoresist and a $25\times/\text{NA}0.8$ objective lens. The lens had a radius of curvature of 1.03 mm, a conic constant of -2.30, and dimensions of $75 \times 100 \times 3.9 \mu\text{m}^3$. For the printing process, a 20 mW laser power was used, along with a focus scanning velocity of 4 cm/s, a slicing distance of 50 nm, and a hatching distance of 100 nm. QPI measurements of the lens were conducted both in situ and after development and re-immersion, in addition to ex-situ height measurements. These results are

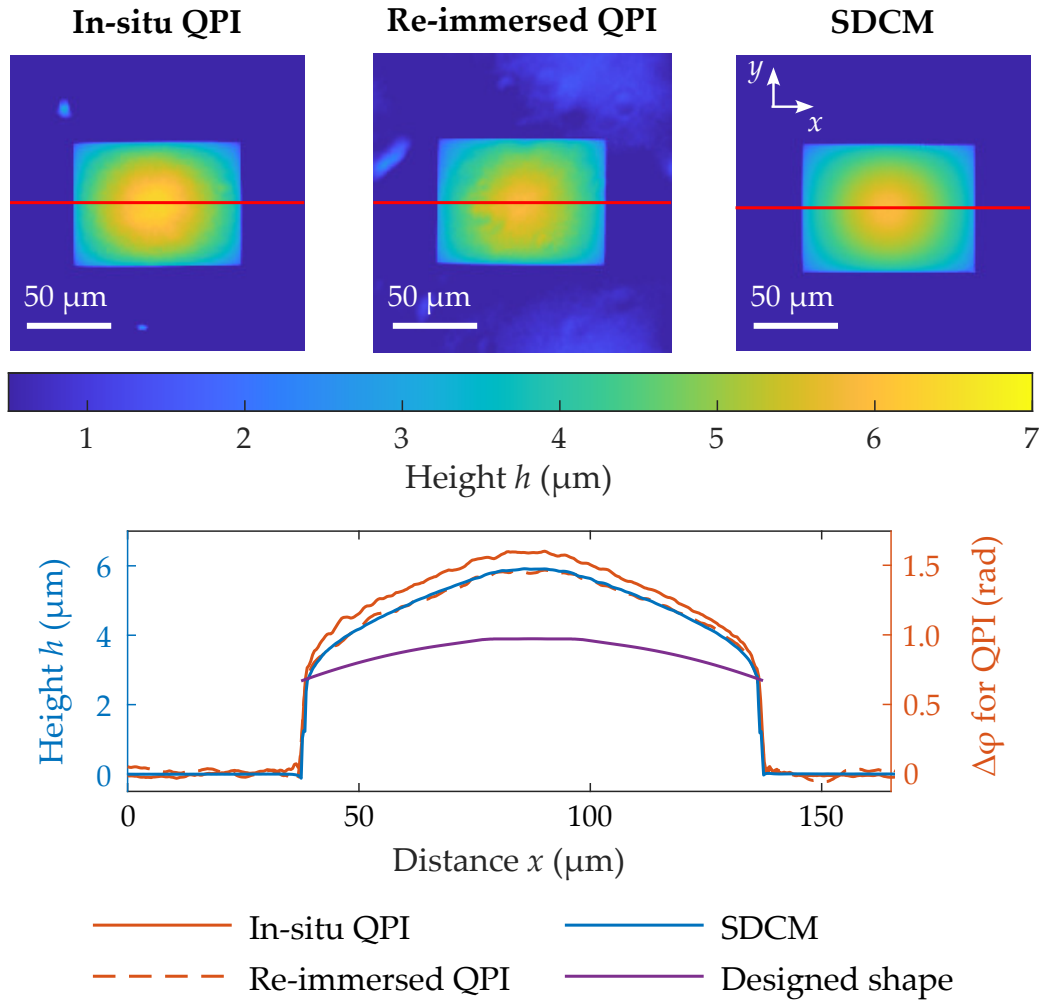


Figure 5.8: Printed micro-lens measurements. At the top: topography maps of the printed micro-lens measured in three configurations: in-situ QPI, re-immersed QPI, and SDCM direct height measurements. QPI topography maps are obtained by recalculating measured phase difference (optical path length) using the refractive index difference of $\Delta n = 0.025$. At the bottom: phase/height profiles taken along the red line. In-situ QPI (orange curve), re-immersed QPI (orange dashed curve), and SDCM (blue curve) measurements are plotted using two y -axes with one axis representing height and the other representing phase difference. Adapted from [119].

presented in Figure 5.8 and depicted as height maps using a unified color bar at the top of the figure. Phase measurements were recalculated into height using the average refractive index difference for IP-S of $\Delta n_{\text{IP-S}} = 0.025$, which were defined from Figure 5.7.

The bottom half of Figure 5.8 shows the height/phase profiles taken in the middle of the lens, indicated by a red line. These profiles are plotted using two y -axes:

the left axis, colored blue, corresponds to the measured (and recalculated) height, while the right axis, colored orange, corresponds to the measured phase differences. Analyzing the measured data, it is possible to deduce a lens shrinkage of approximately 7% by comparing the in-situ and re-immersed phase differences. It is also evident that the QPI-calculated height profile of the re-immersed sample (dashed orange curve) aligns well with the height measurements obtained by SDCM (blue curve), further confirming the validity of the imaging method. Additionally, the measured data reveal deviations between the intended and obtained shapes. This discrepancy arises because the designed height does not account for the voxel size and the proximity effect. This discrepancy can be further measured and pre-compensated in situ in the same manner as it is performed with ex-situ height measurements [55]. Another method of improving the quality of printed structures is utilizing multi-photon grayscale lithography, which adjusts the voxel height to achieve more precise printing [38].

5.3.2 *Diffraction Optical Elements*

In-situ QPI is also suitable for shape measurements of printed diffractive optical elements (DOEs). These 2.5D DOEs, fabricated by laser microprinting, can feature various designs for manipulating and splitting laser beams, tailored to specific applications and operating across different wavelengths. In the following, two DOEs that have been previously used to separate multiple focus arrays for next-generation laser printers were examined.

The first DOE was designed by Pascal Kiefer for 7×7 foci laser printing at high scanning speeds [121]. The single unit cell of this DOE was printed using the IP-S photoresist and the $25\times/\text{NA}0.8$ objective lens. The sample was printed with the following parameters: 15 mW laser power, 4 cm/s focus scanning velocity, 85 nm slicing distance, and 100 nm hatching distance. The DOE was designed to have a smooth shape, avoiding sharp height jumps between adjacent pixels within the DOE. The imaging of the unit cell was performed following the same procedure as for the micro-lens in the previous subsection and presented in the same manner in [Figure 5.9](#).

Analyzing the obtained phase/height maps and profiles, one could observe that there are almost no differences between in-situ QPI, re-immersed QPI, and SDCM measurements. The shrinkage deduced by comparing in-situ and re-immersed phase differences is less than 5%. Similar to the microlens case, the actual measured height of this DOE deviates from its designed value. This discrepancy is attributed to the height of the voxel and the pronounced proximity effect of the IP-S photoresist.

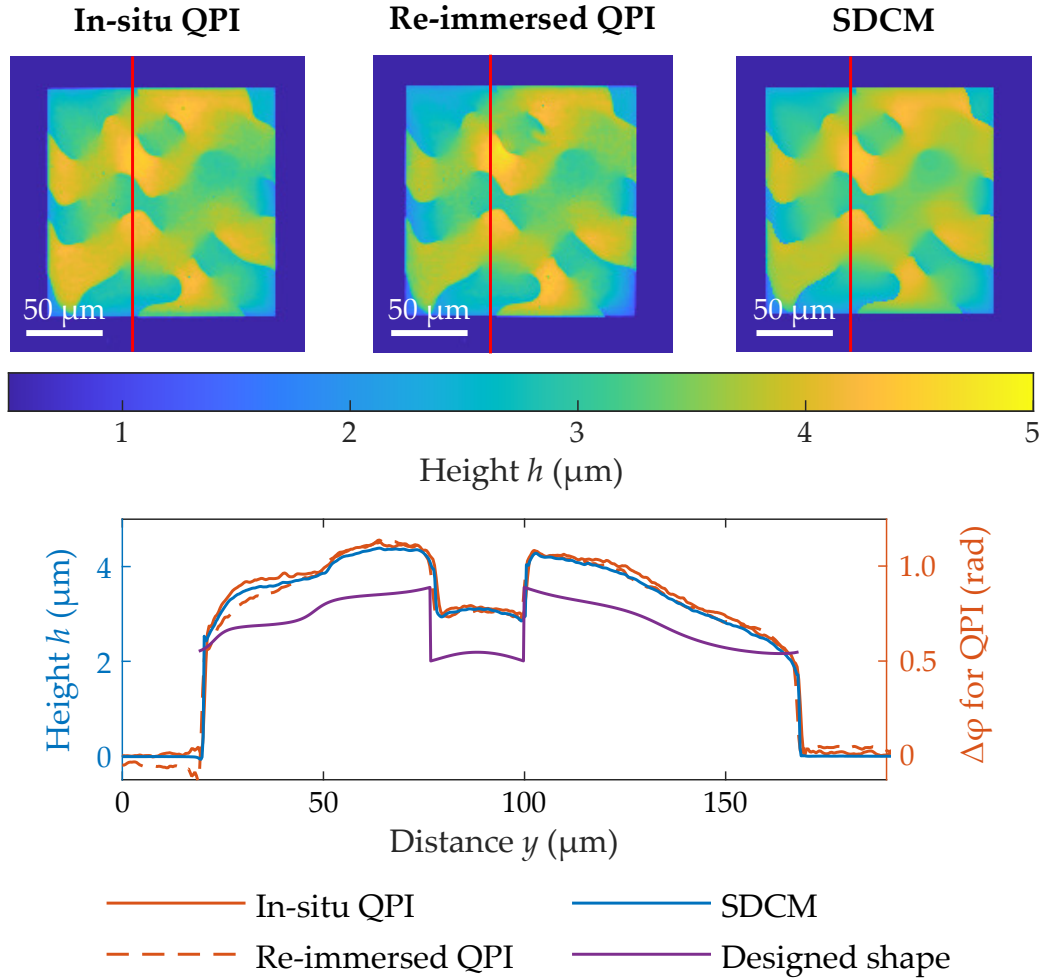


Figure 5.9: Printed IP-S DOE measurements, design from [121]. In-situ QPI, re-immersed QPI, and SDCM measurements of the IP-S DOE. Measurements follow the same interpretation as for Figure 5.8. Adapted from [119].

The second DOE was designed by Vincent Hahn and employed for splitting the laser beam into 3×3 beamlets [122]. Several DOE units were fabricated using the IP-Dip photoresist and the $63\times/\text{NA}1.4$ objective lens. The sample was printed using the following parameters: 30 mW laser power, 5 cm/s focus scanning speed, and 145 nm hatching distance. This DOE consisted of only eight different height levels and hence did not have a specific slicing distance. The measured phase/height maps and profiles of the IP-Dip DOE are depicted in Figure 5.10. The phase difference was recalculated into height using the same refractive index difference $\Delta n_{\text{IP-Dip}} = 0.025$, as used for the IP-S photoresist.

For the IP-Dip DOE, the difference between in-situ and re-immersed phase differences was also minimal as for the IP-S DOE. The relative shrinkage was less than

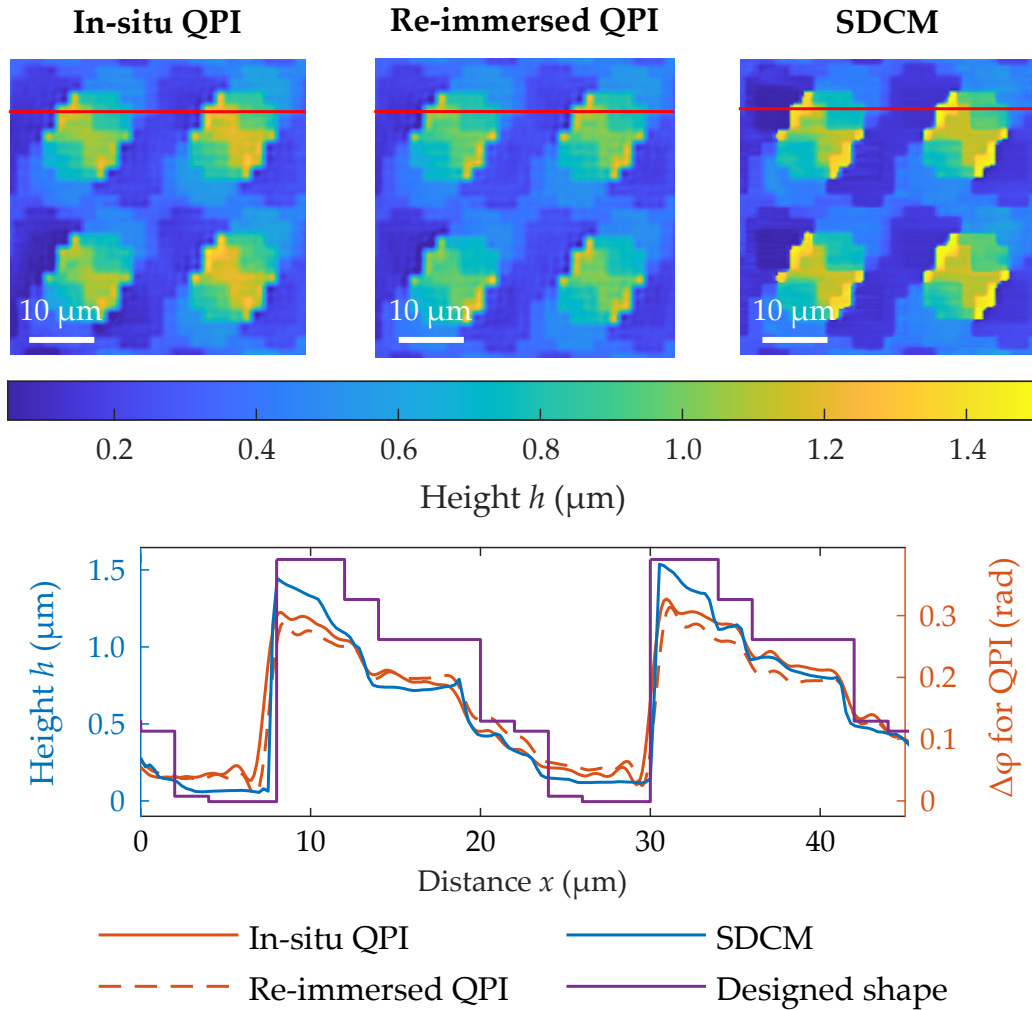


Figure 5.10: Printed IP-Dip DOE measurements, design from [122]. In-situ QPI, re-immersed QPI, and SDCM measurements of the IP-Dip DOE. Measurements follow the same interpretation as for Figure 5.8. Adapted from [119].

5% as well. Notably, the second DOE was specifically designed and optimized for printing with the Nanoscribe PPGT. Therefore, the designed shape was much more similar to the measured height values compared to the previously imaged structures. The observed discrepancies between the designed and measured heights are primarily due to printing imperfections, which can be further optimized for a better match.

5.3.3 Phase Plate

Another potential application of in-situ QPI is the phase examination of printed phase plates. These plates are particularly useful in applications such as X-ray

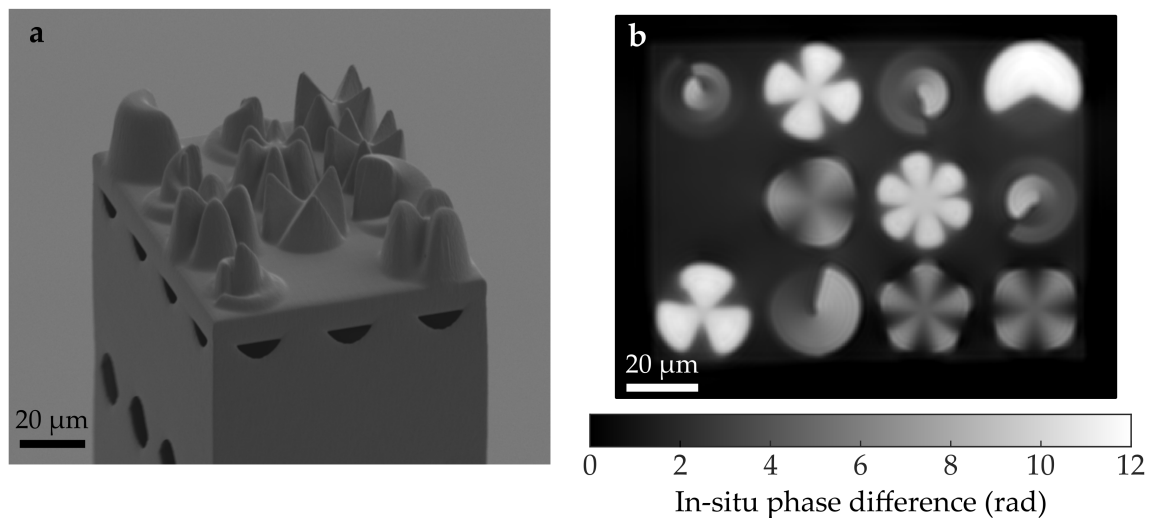


Figure 5.11: Printed phase plate measurements. **a** SEM image of the printed phase plate on the top of a lens array for X-ray multi-beam imaging. **b** In-situ QPI measurements of the separately printed phase plate. Adapted from [125].

multi-beam imaging, where they decode additional phase information in each beam [123, 124]. This helps to prevent the overlapping of signals from multiple beams at the detector, enhancing clarity and resolution in the imaging process.

An example of a printed phase plate, designed by Tang Li for 3×4 beam ptychography for 13 keV photon energy [125], is showcased in Figure 5.11a. This sample was printed using the IP-S photoresist and a $25\times/\text{NA}0.8$ objective lens. The following parameters were used for printing: 25 mW laser power, 7.5 cm/s focus scanning speed, a slicing distance of 300 nm, and a hatching distance of 200 nm. The in-situ QPI characterization of the separately printed phase plate is presented in Figure 5.11b. The QPI measurements provide valuable insights into the accumulated optical path lengths of each phase element, enabling clear distinction between all phase elements.

5.4 CONCLUSION

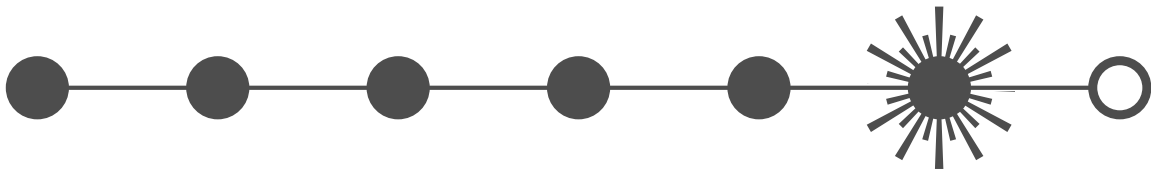
This chapter explored the application of the QPI technique, commonly used in biophotonics, for in-situ imaging of laser microprinting. This technique is fast and accurate, enabling the effective in-situ acquisition of printed shapes within seconds. However, the most significant advantage of this approach is its independence from additional setups. Obtaining the phase difference or optical path length of the printed sample by solving the TIE requires only the capture of defocused images, which can be performed by any laser printer equipped with imaging capabilities.

The proposed in-situ QPI is robust and was validated by ex-situ height measurements. The axial resolution of this method is less than 100 nm, which makes in-situ QPI an attractive tool for the in-situ correction of printed micro-optics. Additionally, one can deduce polymer refractive index and shrinkage values, provided that further ex-situ measurements are carried out. However, several limitations of this method should be noted:

1. TIE derivation (Equation 3.24-Equation 3.28) relies on the paraxial or slowly-varying phase approximation. Therefore, additional artifacts might appear if an imaged specimen has abrupt height steps or tall walls.
2. In Equation 5.1, it is assumed that the refractive index does not depend on the spatial coordinates, which can be violated for some samples. For example, the small discrepancy between the in-situ measured shape of the IP-Dip DOE and its ex-situ SDCM height (Figure 5.10) might stem from this effect.
3. TIE is solved computationally using the fast Fourier transform, as described in Equation 3.31. However, applying FFT implies the use of periodic boundary conditions, which can lead to artifacts at the boundaries if the sample is larger than the camera's field of view. To prevent this, several methods can be employed, including the use of different computational algorithms that better handle boundary conditions [126] or placing a small aperture in the microscope image plane to minimize edge effects [127].
4. When taking intensity images in situ, some deviations might occur due to variations in the medium. For instance, as detailed in Figure 4.6, small refractive index "blobs" can appear within the volume of a photoresist. These blobs introduce additional artifacts which can be observed in the in-situ phase reconstruction, such as in the printed micro-lens depicted in Figure 5.8. These artifacts must be considered when analyzing the quality and accuracy of phase reconstructions.

Finally, a significant limitation of QPI in general is its restriction to imaging only 2.5D, holeless structures. Expanding this technology to encompass full 3D imaging involves solving a complex inverse problem, which requires additional computational efforts and measurement procedures. This expansion and its challenges will be discussed in detail in the next chapter.

6 IN-SITU TOMOGRAPHIC RECONSTRUCTION VIA DEEP LEARNING



Typical tomographic reconstruction approaches require some form of scanning, either by varying the illumination direction or by rotating/moving the sample. In contrast, the tomographic reconstruction method presented in this chapter does not require any additional scanning or measurements. All images are captured during the printing process with only minimal delays for exposure time. The resulting stack of microscopic images is then processed by a specially designed and trained 3D neural network to produce a binarized refractive index reconstruction. The chapter begins with a description of the inverse optical problem, followed by a solution utilizing the deep learning approach. The core of the chapter is the presentation of experimental in-situ 3D reconstructions and their comparisons with ex-situ SEM images. It concludes with an analysis of the robustness of the proposed approach.

6.1 INVERSE PROBLEM FOR IN-SITU IMAGING

To expand QPI for 3D tomographic reconstruction, it is necessary to additionally scan the imaged specimen from multiple directions and address the inverse tomographic problem. A common method for this is optical diffraction tomography (ODT), which involves acquiring images over different illumination directions and reconstructing the 3D refractive index of the sample under the first Born or Rytov approximations in an iterative manner. The principle of ODT and its application to the imaging of 3D-printed specimens was described in [subsection 3.5.4](#). However, a major challenge with this approach is missing cone artifacts that significantly deteriorate the reconstruction quality of large samples.

In contrast to biophotonics, where QPI and ODT are the main tools for label-free non-invasive imaging, in-situ imaging during laser microprinting offers a significant advantage. It allows access to unfinished samples, providing a greater degree of freedom in acquiring as many intermediate images as needed throughout the printing process. Moreover, bright-field intensity images are routinely captured during printing to monitor any deformations that may occur in the sample. However, to perform any 3D shape reconstruction from these images, it is necessary to solve the inverse scattering problem and obtain the refractive index distribution from the intensity image stack obtained during printing.

Assuming that intensity images are acquired for each printed slice, the resulting image stack will consist of intensities influenced by two optical effects: transmission through the accumulated phase and optical defocusing. The electric field can be modeled using the well-known beam propagation method [75], which relies on small refractive index differences between a specimen and a surrounding medium, $\Delta n \ll n$, an approximation that is justified for in-situ imaging of printed structures. For the k^{th} printed slice, the electric field can be expressed through the following recursive formula [128]

$$E_k(\mathbf{r}) = T_k \cdot P_{\Delta z}(E_{k-1}(\mathbf{r})), \quad (6.1)$$

where $\mathbf{r} = (x, y)$, T_k denotes the complex transmittance of the printed slice, and $P_{\Delta z}(E_{k-1}(\mathbf{r}))$ is the field propagation operator that propagates the field from the accumulated transmission of all previous $k - 1$ slices to the slicing distance Δz . This propagation can be computed using either the Rayleigh-Sommerfeld diffraction integral or the angular propagation method [75], as will be detailed in [subsection 6.3.3](#). The transmittance T_k is related to the optical thickness or phase change $\Delta\phi_k$ of the printed slice and hence to the product of the refractive index difference Δn_k and the voxel height Δh as

$$T_k \propto e^{i\Delta\phi_k} \propto e^{i\Delta n_k \cdot \Delta h}. \quad (6.2)$$

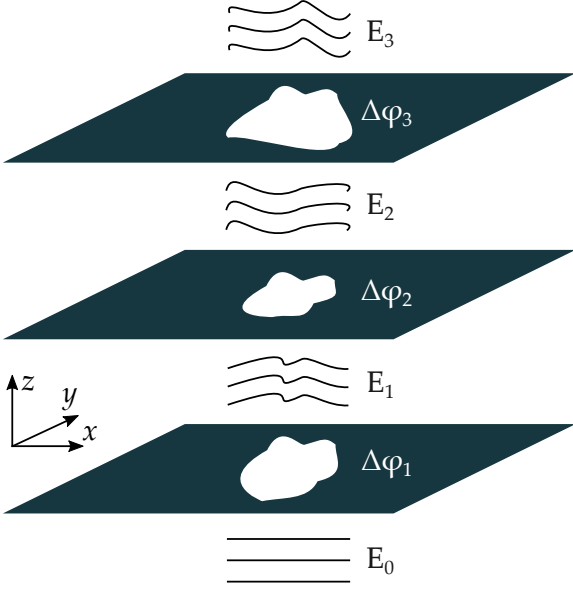


Figure 6.1: Illustration of the wavefront change during 3D laser printing. If the sample is illuminated with the plane wave with the electric field E_0 , the resulting electric field after the printing of k^{th} slice will be influenced by transmission through phase difference $\Delta\phi_k$ of the printed slice and an additional optical defocus in the z -direction. The electric field at each slice can be calculated using [Equation 6.1](#).

The resulting intensity of the current slice I_k is then calculated as the squared absolute value of the electric field

$$I_k = |E_k|^2. \quad (6.3)$$

The change in the wavefront after passing through the first three printed slices is schematically depicted in [Figure 6.1](#).

Thus, the inverse problem requires determining the refractive index difference for each slice based solely on the intensities recorded during the printing process. Notably, reconstructing binarized values of refractive index distribution, where ones represent polymer and zeros represent monomer is already enough for obtaining the shape and geometry of the printed structure.

6.2 END-TO-END DEEP LEARNING APPROACH

The formulated inverse problem, due to its inherent complexity, demands advanced computational methods for solving. Specifically, the use of absolute values to obtain intensities in [Equation 6.3](#) eliminates the essential complex information about the electric fields needed for defining optimization problems. Alternatively, an end-to-end deep learning (DL) approach can be implemented. This method includes training a deep neural network on a dataset of intensity stacks to predict the 3D (binarized) refractive index difference distribution as the output. The network should interpret complex intensity patterns for each printed slice and effectively transform them into (binarized) refractive index distributions. In standard 3D recognition tasks, U-Nets with three-dimensional convolutional layers

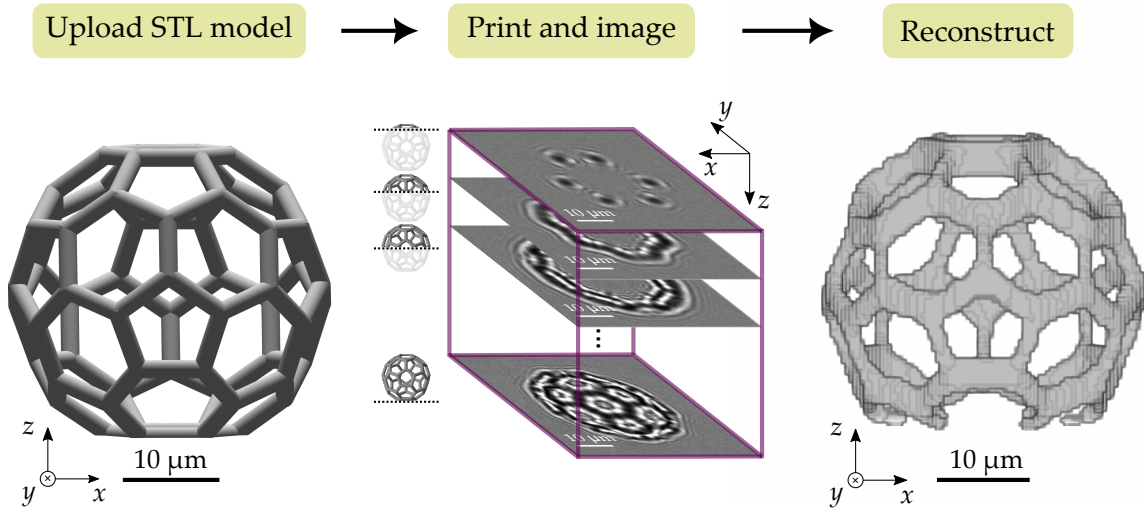


Figure 6.2: Deep learning tomographic reconstruction pipeline. A 3D stereolithography (STL) model is uploaded into the printer software, where it is transformed to coordinates for further laser printing. During printing, bright-field intensity images are taken with each slice of printed object. The obtained image stack is then used as input for deep learning end-to-end reconstruction on the example of a printed buckyball. Adapted from [136].

(3D U-Nets) [129, 130] are known for their proficiency in processing and analyzing 3D data across a variety of applications, from medical imaging [131] to materials science [132]. The architecture of a 3D U-Net features a series of convolutional layers that contract in the encoder to learn feature representations and generalize better, followed by an expansion in the decoder, which enables the network to capture essential global and local spatial information necessary for comprehensive 3D reconstruction. 3D U-Nets have been successfully implemented for end-to-end reconstruction in computer tomography [133], X-ray diffraction imaging [134], and optoacoustic tomography [135].

From the user's perspective, the end-to-end DL reconstruction approach should predict the printed 3D shape and identify any appearing deviations from the intended stereolithography (STL) model uploaded into the printer software. The DL reconstruction pipeline is illustrated in Figure 6.2. After uploading an STL model, the user prints the 3D sample while simultaneously capturing bright-field intensity images of each printing slice. These images are then compiled into a stack and used as input for the trained 3D U-Net, which reconstructs the printed sample.

From the experimental point of view, it is enough to have the defined illumination that produces a quasi-monochromatic coherent plane wave. Therefore, the same

illumination configuration, presented in [Figure 5.1](#), as used for in-situ QPI, can be utilized for image acquisition.

To effectively train a 3D U-Net for reconstructions, a substantial number of ground truth pairs are required. These pairs should consist of in-situ intensity stacks from various printed objects along with their corresponding 3D refractive index data. Experimentally obtaining these ground truth datasets is not feasible due to the lack of a robust 3D in-situ reconstruction tool. Instead, a simulation-based learning approach can be employed, where the required intensity datasets are simulated from refractive index distributions using a forward propagation model. Using this approach, one can simulate as many 3D objects as needed for effective training of the 3D U-Net. However, the primary drawback of this method is its dependency on the realism of the simulated ground truth datasets, which must closely resemble experimental conditions. The next section will elaborate on the entire process of generating realistic and comprehensive ground truth datasets, which are then utilized for training and subsequent experimental validation.

6.3 GROUND TRUTH SIMULATIONS

The process of synthesizing realistic 3D ground truth dataset pairs was split into several steps:

1. 3D object generation.
2. Refractive index assignment.
3. Intensity simulations.
4. Additional post-processing.

All datasets were designed for the Nanoscribe PPGT system with the IP-S photore-sist and the $25\times/\text{NA}0.8$ objective lens. The imaging pixel size of this configuration corresponds to $\Delta x = 0.4 \mu\text{m}$ and the standard slicing distance is $\Delta z = 0.3 \mu\text{m}$. In the following, each step of the generation procedure is described in detail.

6.3.1 3D Object Generation

Ground truth datasets must include diverse 3D printing models to account for a broad range of geometrical features and complexities found in actual printing scenarios. To address this need, the large 3D model database from Princeton, known as ModelNet40 [137], was utilized to generate different 3D objects. ModelNet40 includes 10,000 3D models divided into 40 different classes. From these, 30 classes were allocated for generating training datasets, while the remaining 10 were used for testing purposes. Originally intended for 3D recognition tasks, this database

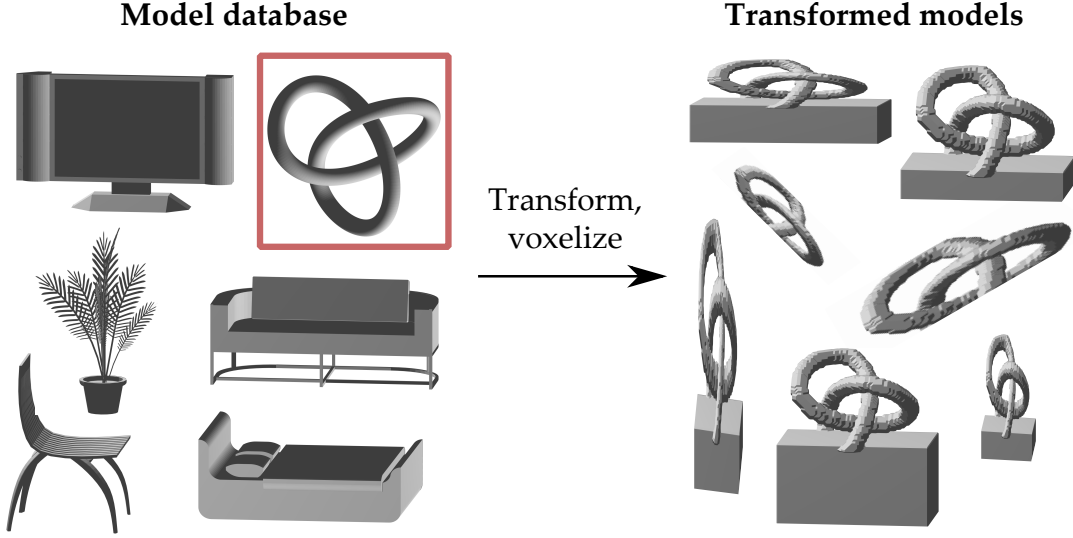


Figure 6.3: Object generation stage. Complimentary model database consisted of 3D models from ModelNet40 and additionally generated trefoil knots. Additionally, structures underwent random transformations such as rotation, rescaling, cropping, and placement on a random pedestal. Transformed models were also voxelized to $128 \times 128 \times 128$ volumes during this operation. Adapted from [136].

also serves as a comprehensive resource for generating 3D models for training in applications such as 3D shape reconstruction. Additionally, a trefoil knot model was added to the 3D model database. The trefoil knot model was defined by a parametric formula

$$x = \sin(t) + 2 \sin(2t); y = \cos(t) - 2 \cos(2t); z = -\sin(3t); t \in [0, 2\pi]. \quad (6.4)$$

To generate the final 3D model for further intensity simulations, a random sample from the complementary 3D model database was chosen (for example, trefoil knot as depicted in Figure 6.3) and randomly transformed. Random transformations included rotation, rescaling, cropping, and placement on a random pedestal. With this procedure, it was guaranteed that the generated sample was unique, and used only once for training. The number of generated samples for training will be discussed below in section 6.4. The code for random object generation was written by Tim Alletzhäusser and its pseudo-code version is presented in section A.1.

During the sample generation process, objects from the complementary model database were voxelized and transformed from their original triangulated form, consisting of vertices and faces, into a binary volume. This volume was constrained to a size smaller than $128 \times 128 \times 128$. Within this volume, the space occupied by the actual model was assigned a value of one, indicating polymerized material,

while the remaining space extending to the boundaries of the $128 \times 128 \times 128$ voxel cube was filled with zeros, indicating unpolymerized parts. Thus, the obtained volume represented 128 slices of the generated structure. Since the pixel for simulations equals $0.4 \mu\text{m}$ and the typical slicing distance used for printing is $0.3 \mu\text{m}$, the resulting simulated volume corresponded to $128 \times 128 \times 128 \times (0.4 \times 0.4 \times 0.3 \mu\text{m}^3)$, which equals to $51.2 \times 51.2 \times 38.4 \mu\text{m}^3$.

6.3.2 Refractive Index Assignment

To simulate light propagation through the generated slices, it is necessary first to assign a refractive index difference between polymerized and unpolymerized parts. For this purpose, the refractive index difference of $\Delta n = 0.026$ that corresponds to the fully polymerized IP-S photoresist [39] was chosen. As will be shown in section 6.6, even though real samples may deviate from this specific value, the deep learning-based 3D reconstruction process remains effective and reliable.

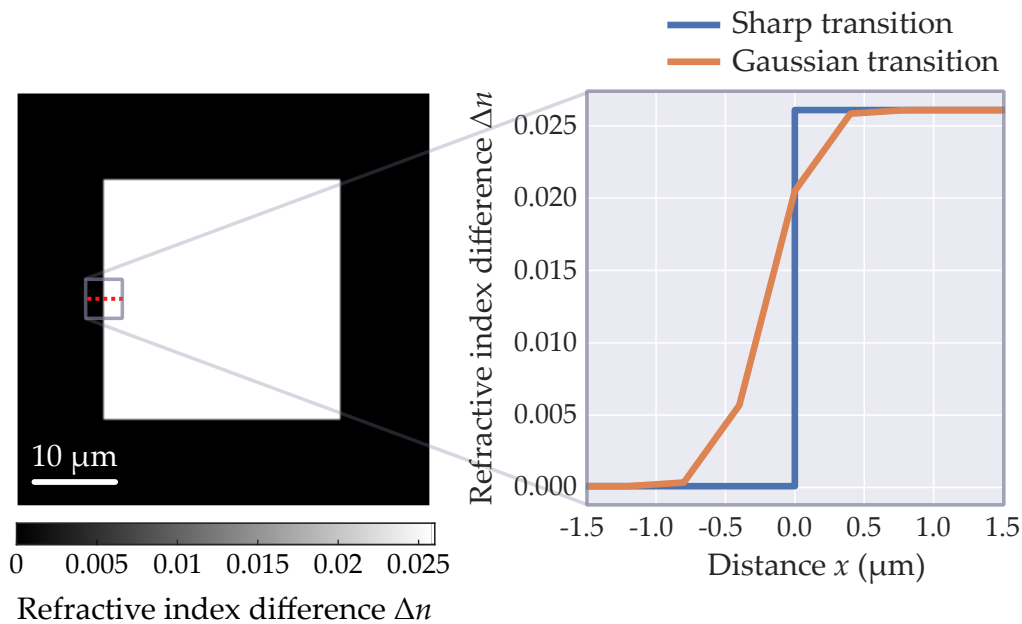


Figure 6.4: Smearing out of the refractive index transition. Exemplary rectangular xy -slice representing refractive index difference between polymer and photoresist Δn . The refractive index differences at the edges were smoothed, as depicted in the gray inset, which shows the refractive index difference profile. The blue curve represents a sharp, step-like transition between the polymer and photoresist. In contrast, the orange curve depicts a Gaussian transition with a standard deviation of $\sigma = 0.7$ pixels. Adapted from [136].

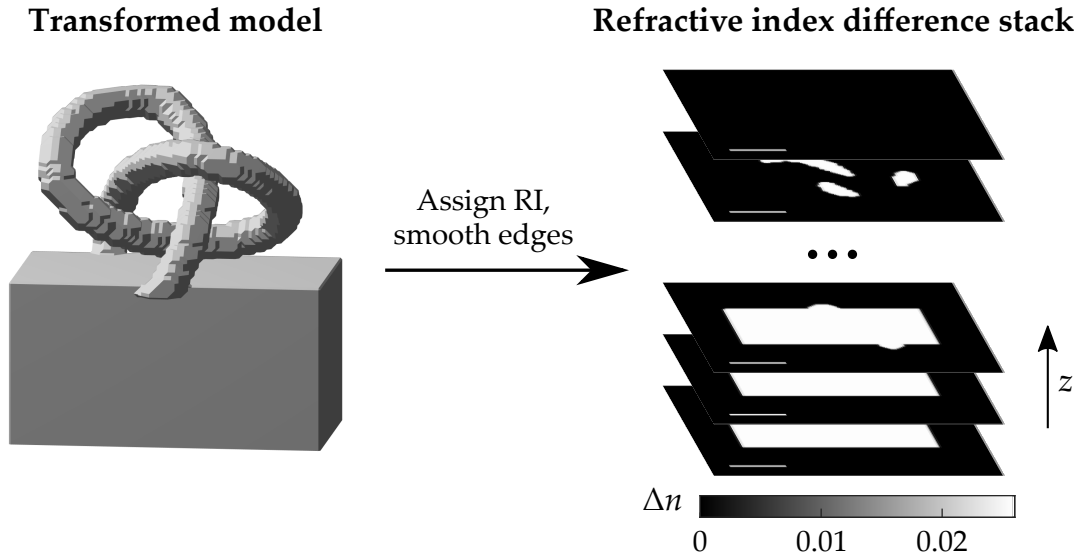


Figure 6.5: Assignment of the refractive index difference. The refractive index difference of $\Delta n = 0.026$ was assigned to the simulated 3D model using trefoil knots as an example. Additionally, the refractive index transitions between polymerized and unpolymerized parts were smoothed as shown in Figure 6.4. The scale bar equals 10 μm . Adapted from [136].

However, as revealed by OCT measurements, the refractive index transition between polymerized material and its surroundings is not abrupt but resembles a smooth function, akin to the Gaussian error function. This transition has a width on the order of 1 μm , as illustrated in Figure 4.13. This gradual change impacts how light propagation is modeled in simulations and is crucial for simulating real experimental settings. Therefore, a 2D Gaussian filter with a standard deviation of 0.7 pixels was applied to each slice of the generated volume. This Gaussian filter smoothes edges between polymer and monomer in the xy -direction. An exemplary refractive index transition graph of one slice of a rectangular object is presented in Figure 6.4. The refractive index difference slices of the generated exemplary trefoil knot structure located on a cuboid pedestal are depicted in Figure 6.5.

6.3.3 Intensity Simulations

Finally, the generated refractive index difference stack can be utilized for light propagation simulations and the computation of intensity images. The process of forward light propagation is described by the beam propagation method in Equation 6.1 – Equation 6.3. This recursive propagation is identical to the multi-slice beam propagation model (MSBPM) that is widely used in bioimaging

[97, 138, 139]. MSBPM was originally developed to simulate light transmission through biological specimens, approximated by thin slices with small differences in refractive index. The final electric field is calculated via sequential layer-to-layer propagation in the z -direction. Given that our simulated objects are already segmented into slices, the MSBPM algorithm can be readily adapted to simulate intensities for each slice of the object.

In MSBPM, the electric field at the k^{th} slice $E_k(\mathbf{r})$ is calculated using the recursive formula

$$E_k(\mathbf{r}) = T_k \cdot P_{\Delta z}(E_{k-1}(\mathbf{r})), \quad (6.5)$$

where $\mathbf{r} = (x, y)$, k ranges from 1 to 128 for the simulated volumes, T_k denotes the complex transmittance of the k^{th} slice, and $P_{\Delta z}$ is the forward propagation operator, which defocuses the previous electric field E_{k-1} by the slicing distance Δz . The complex transmittance is written as

$$T_k = \exp\left(\frac{2\pi i \Delta z \Delta n_k(\mathbf{r})}{\lambda}\right), \quad (6.6)$$

where $\lambda = 0.63 \mu\text{m}$ is the free-space central LED wavelength and $\Delta n_k(\mathbf{r})$ is the simulated refractive index difference of the current slice. The standard for laser printing slicing distance of $\Delta z = 0.3 \mu\text{m}$ is assumed for all simulations. The propagation operator is calculated according to the angular spectrum method as

$$P_{\Delta z}(x) = \mathcal{F}^{-1} \left(\mathcal{F}(x) \exp \left(2\pi j \Delta z \sqrt{\left(\frac{n_{\text{pr}}}{\lambda}\right)^2 - \mathbf{u}^2} \right) \right), \quad (6.7)$$

where \mathcal{F} and \mathcal{F}^{-1} are Fourier and inverse Fourier transforms, $n_{\text{pr}} = 1.483$ is the refractive index of the IP-S photoresist, and $\mathbf{u} = (u_x, u_y)$ denotes spatial frequency coordinates. Equation 6.5 is initialized with the plane wave boundary conditions, meaning $E_0 = \mathbf{1}_{128 \times 128}$.

Since the imaging plane is shifted by $-24 \mu\text{m}$ from the printing plane (Figure 2.5), one should account for the additional electric field defocus $P_{z_{\text{shift}}}(E_k(\mathbf{r}))$ that occurs in the printing setup. Additionally, one should account for the low-pass circular filtering $C(\mathbf{u}) = \circ(\mathbf{u}\lambda/\text{NA})$ that is introduced by the objective lens with $\text{NA} = 0.8$. This filtering means that only frequencies that satisfy the equation

$$u_x^2 + u_y^2 < \left(\frac{\text{NA}}{\lambda}\right)^2 \quad (6.8)$$

can be passed. Finally, intensities for each slice of the simulated volume were computed as

$$I_k(\mathbf{r}) = |\mathcal{F}^{-1} \left(C(\mathbf{u}) \mathcal{F} (P_{z_{\text{shift}}}(E_k(\mathbf{r}))) \right)|^2. \quad (6.9)$$

Computed intensities of the exemplary trefoil knot model stack and scheme of the computation are depicted in [Figure 6.6](#).

Despite simulating realistic intensity images, the MSBPM algorithm lacks consideration for one significant feature in practical applications. In [Equation 6.6](#), the thickness of single printed slice is the slicing distance $\Delta z = 0.3 \mu\text{m}$. In other words, MSBPM assumes that single simulated voxel has dimensions of $\Delta x \times \Delta y \times \Delta z$, which equals to $0.4 \times 0.4 \times 0.3 \mu\text{m}^3$. However, in reality, the use of the $25\times/\text{NA}0.8$ objective lens introduces an extended voxel height of approximately $2.3\text{-}2.7 \mu\text{m}$ for each printed slice. This means that one real printed slice should correspond to approximately 9 simulated slices. This discrepancy means that the forward model used in simulations must be modified to incorporate the actual voxel height introduced by the objective lens.

This modification cannot be achieved simply by substituting $9\Delta z$ for Δz in all equations, as the spacing between images (axial imaging resolution) remains equal

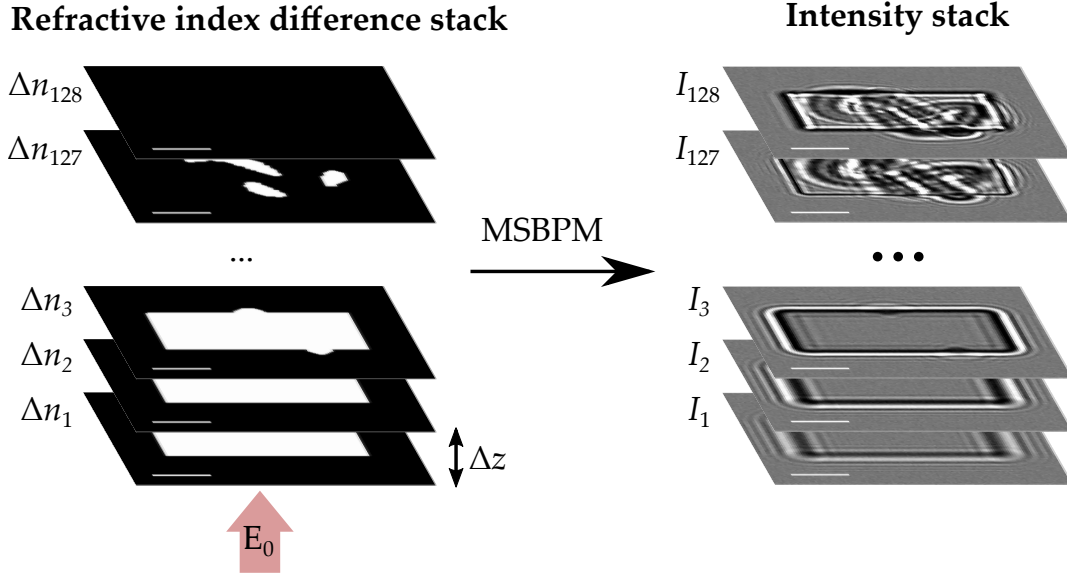


Figure 6.6: Simulation of in-situ intensities using multi-slice beam propagation model (MSBPM). Exemplary refractive index difference slices (from Δn_1 to Δn_{128}) of simulated trefoil knots were used to simulate intensities using [Equation 6.5](#) – [Equation 6.9](#). The boundary condition is the incident plane wave E_0 as depicted by a red arrow. The scale bar corresponds to $10 \mu\text{m}$. Adapted from [136].

to the slicing distance. Thus, a new algorithm had to be developed to account for the voxel height while maintaining the same axial spacing of $0.3 \mu\text{m}$. The modified MSBPM (m-MSBPM) calculates field propagation using slice stacks composed of 9 slices, each with a voxel height of $2.7 \mu\text{m}$. The m-MSBPM calculates intensities for each slice of the simulated 3D object in three steps:

1. Calculate the slice stack for the current slice of the simulated model.
2. Propagate the field using MSBPM to the end of the slice stack.
3. Defocus the field to the center of the slice stack and calculate the intensity.

A more detailed m-MSBPM algorithm is provided in the pseudo-code format in [section A.2](#). The computation algorithm was implemented using the TensorFlow library of Python [140]. It took approximately 0.5 s to calculate the whole intensity stack from a $128 \times 128 \times 128$ simulated refractive index difference volume. Examples of intensity simulations using both standard and modified MSBPM as well as experimental intensities of the printed buckyball are shown in [Figure 6.7](#). As observed from the 128th slice, the difference between the minimal and maximal intensities of the buckyball rods is significantly smaller in the standard MSBPM compared to both the m-MSBPM and the experimental intensities.

6.3.4 Post-processing

The experimental images exhibit shot noise as can be seen from the first column of [Figure 6.7](#). To simulate realistic intensities, Gaussian noise with a standard deviation of $\sigma = 0.03$ of normalized intensities was added to the m-MSBPM intensity simulations. This specific level of noise was measured during a 5 ms exposure time on a plain photoresist volume without any printed structures in the field of view, ensuring that the simulated images accurately represent the actual experimental conditions. This noise level is already presented in the simulated images in [Figure 6.7](#). The images simulated by m-MSBPM with added noise were used as inputs for the deep learning algorithm.

To simulate accurate ground truth outputs, two additional operations were performed. First, the 3D refractive index distributions were binarized into zeros and ones, representing photoresist/monomer and polymerized parts, respectively. This step was carried out to facilitate the use of binary classification deep learning algorithms, significantly simplifying the learning process. Secondly, the binarized volumes were dilated (or axially extended) to account for the voxel height of $2.7 \mu\text{m}$, meaning that each voxel of the simulated volume was extended from $1 \times 1 \times 1$ to $1 \times 1 \times 9$ or in the real space from $0.4 \times 0.4 \times 0.3 \mu\text{m}^3$ to $0.4 \times 0.4 \times 2.7 \mu\text{m}^3$.

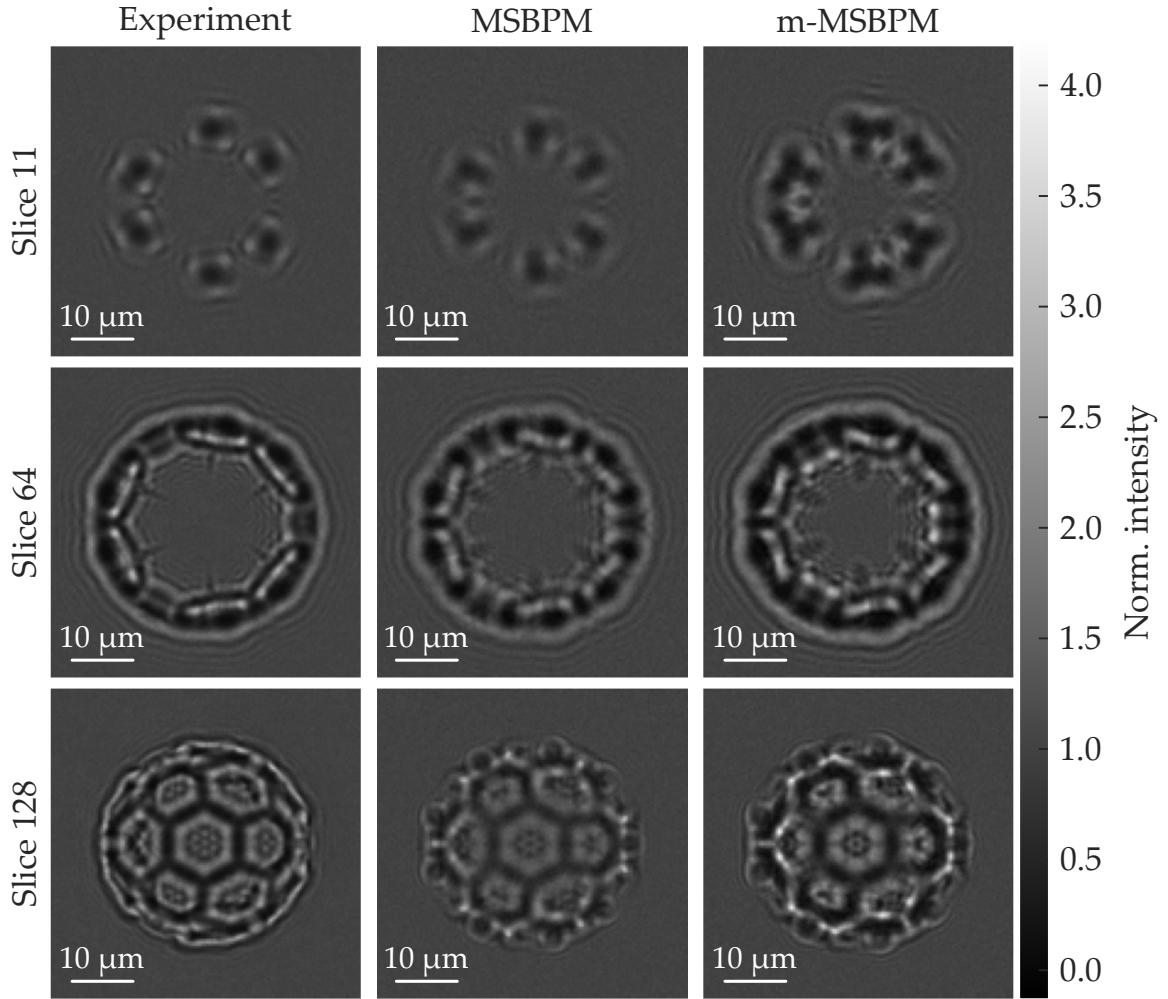


Figure 6.7: Experimental and simulated intensity images of a buckyball model. Normalized intensities for experimental intensities taken during 3D laser micro-printing (first column), simulated intensities using standard MSBPM (second column) and MSBPM modified to the voxel height of $2.7 \mu\text{m}$ (m-MSBPM, third column). The current number of printed/considered slices during printing/simulation is indicated on the left. The discrepancies between m-MSBPM and the experimental images mainly originate from the difference between the printed geometry and the STL model used for simulations. The Gaussian noise was already added to the simulated images. Adapted from [136].

6.4 3D U-NET TRAINING AND TESTING

6.4.1 Training

The simulated 3D inputs and outputs can be readily used for end-to-end training of the 3D U-Net. Given the need to simulate hundreds of thousands of 3D models

for effective training, it is impractical to pre-simulate all the ground truth datasets beforehand due to the substantial memory requirements. Therefore, a streamlined or online training approach was utilized. In this approach, models are simulated on the fly during the training process, which helps manage the computational and storage demands. This method optimizes the learning process by continuously providing fresh data, which is essential for preventing overfitting and enhancing the generalization capabilities of the neural network. The same approach for an infinite stream of training data for inverse tasks has also been utilized in the field of X-ray diffraction [141].

Thus, batches of 10 ground truth pairs were continuously simulated using a CPU (Intel Xeon Platinum 8260) and placed into a queue for subsequent training of 3D U-Net using a GPU (Nvidia RTX A6000, 48 GB of memory). For each step, one generated batch was used for training and then deleted from the memory to optimize resource utilization. A more detailed pseudo-code algorithm for batch generation is presented in [section A.1](#).

The 3D U-Net with 700,000 training parameters was programmed by Tim Alletzhusser and its architecture is presented in [section A.3](#). During training, parameters were updated via the Adam optimizer [142] with an initial learning rate of $5 \cdot 10^{-4}$. The learning rate was further decreased by a third after every thousand training steps. A weighted binary cross entropy (BCE) served as a loss function. The weighted BCE for the input batch with $128 \times 128 \times 128 \times 10$ dimensions was defined as

$$\text{BCE}_{\text{weighted}} = \frac{1}{128} \frac{1}{128} \frac{1}{128} \frac{1}{10} \sum_{i,j,k=1}^{128} \sum_{l=1}^{10} w_k \cdot \left(Y_{ijkl} \cdot \log \left(P(Y_{ijkl}) \right) + (1 - Y_{ijkl}) \cdot \log \left(1 - P(Y_{ijkl}) \right) \right), \quad (6.10)$$

where i, j, k are the summation indices for x, y, z dimensions respectively, l is the summation index for the batch dimension, Y_{ijkl} denotes the ground truth value (zero or one) for the considered voxel, and $P(Y_{ijkl})$ denotes the predicted probability of the voxel being classified as polymer (one). In this formula, w_k corresponds to the weight factor, which was defined for each z -slice as

$$w_k = 1 + 2 \frac{k - 1}{127}. \quad (6.11)$$

The weight vector was designed to assign incrementally larger weights to the furthest slices, with weights incrementally increasing from 1 for the first slice to 3 for the 128th slice. This approach prioritizes the later slices because each subsequent slice, starting from the $(k + 1)$ th slice, contains cumulative information

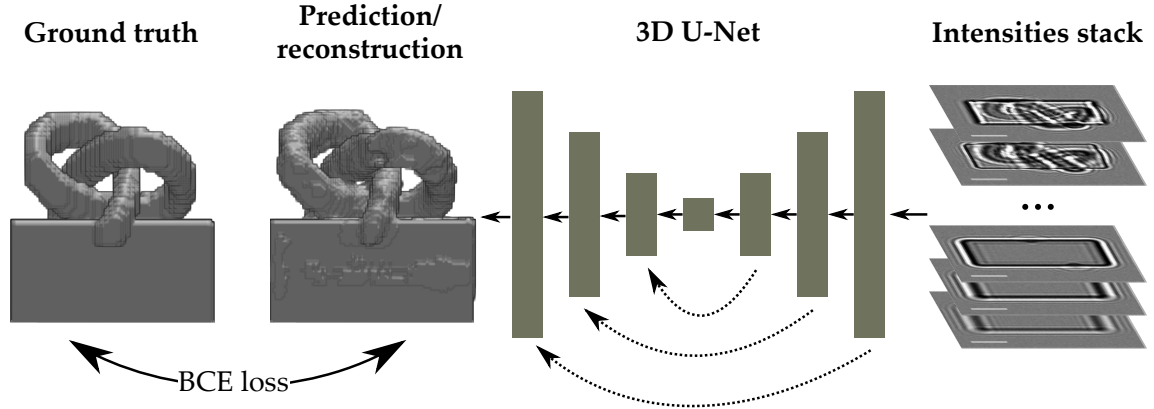


Figure 6.8: Training example of a trefoil knot structure. Computed by m-MSBPM intensity stacks were used as 3D inputs for the 3D U-Net. Generated models were binarized and dilated, and further used as ground truth training datasets. The weights of the network were updated using weighted binary cross-entropy (BCE). The final prediction/reconstruction of the exemplary trefoil knots model is shown as output from the trained U-Net. The gray color corresponds to the reconstructed polymerized parts (ones in prediction). Adapted from [136].

regarding light transmission through all preceding k slices. This weighting strategy emphasizes the importance of the later slices over the initial ones.

The training example based on the reconstruction of the trefoil knot structure, whose simulated intensity stack is shown in Figure 6.6, is depicted in Figure 6.8.

The 3D U-Net was trained over a total of 39,000 steps, during which 390,000 random 3D objects were generated and used for training. The entire training process lasted approximately 21 hours. The resulting training graph as well as a learning rate plot are presented in Figure 6.9. Notably, the training losses reached the local minimum already after approximately 15,000 training steps.

6.4.2 Testing

The trained 3D U-Net was then tested to assess its generalization capabilities and determine whether the neural network could effectively reconstruct completely unseen 3D objects. To determine the prediction performance, estimation metrics typically used for binary classification problems, such as "Precision," "Sensitivity," and "F1-score," were employed. These metrics are defined as

$$\text{Precision} = \frac{TP}{TP + FP'} \quad (6.12)$$



Figure 6.9: Training graph. The network was trained during 39,000 training steps and approximately 21 hours. The training losses are represented in blue, while the smoothed losses are depicted in orange. Below the main training graph, the graph showing the gradually decreasing learning rate is illustrated. Adapted from [136].

$$\text{Sensitivity} = \frac{TP}{TP + FN'} \quad (6.13)$$

$$\text{F1-score} = 2 \cdot \frac{\text{Precision} \cdot \text{Sensitivity}}{\text{Precision} + \text{Sensitivity}}. \quad (6.14)$$

Here, TP , FP , and FN denote true positives, false positives, and false negatives, respectively. Precision measures the proportion of true positives among all predicted positives, while sensitivity measures the proportion of true positives among all actual positives. These metrics help detect if the U-Net over- or underpredicts. Overprediction results in low precision due to many FP , while underprediction leads to low sensitivity due to many FN . The F1-score, the harmonic mean of precision and sensitivity, combines these metrics into a single performance measure.

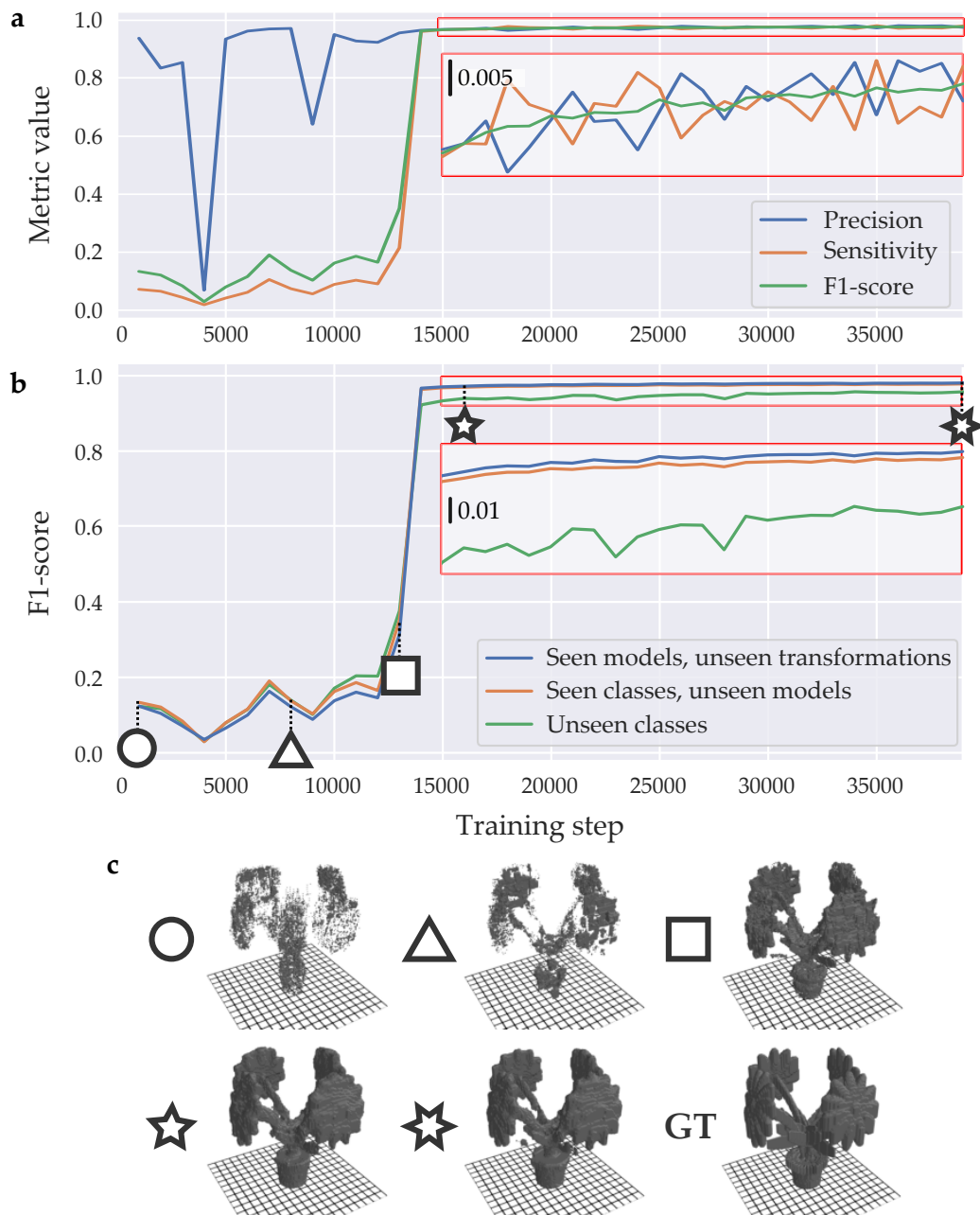


Figure 6.10: Testing graphs. **a** Evolution of Precision (blue curve), Sensitivity (orange curve), and F1-score (green curve) metrics over training steps, for a testing dataset of unseen models. **b** Evolution of F1-score for three types of testing datasets: seen models generated with random unseen transformations (blue curve), unseen models within seen classes of the ModelNet40 database (orange curve), and unseen models from unseen classes (green curve). The enlarged plateau regions for both graphs are shown in the red inset. **c** Reconstruction quality evolution of the example flower model for certain steps, depicted in the panel **b**. Adapted from [136].

A testing plot showing all metrics for a testing dataset consisting of unseen 3D models within seen classes of the ModelNet40 database is presented in [Figure 6.10a](#). As observed from this graph, the metric values fluctuate until the local minimum is reached. After this, both Precision and Sensitivity increase simultaneously with training steps, leading to a gradual improvement in the F1-score.

Additionally, the F1-score evolution was tracked for different testing datasets during training as presented in [Figure 6.10b](#). The first training set comprised randomly transformed 3D models that were used during training (blue curve). The second training set consisted of unseen 3D models within seen classes of the ModelNet40 database as they were originally distributed (orange curve). The third testing set consisted of completely unseen models from unseen classes (green curve). The reconstruction evolution based on the example flower model is depicted in panel c. As clearly seen from the testing plot, the trained U-Net generalizes well with only a small generalization gap in the F1-score of ≈ 0.02 for unseen models between unseen and seen classes. The final values of the F1-score reached for each of the three datasets are 0.98, 0.978, and 0.957 respectively. The last value is particularly significant as it demonstrates that one can accurately reconstruct a completely unseen object.

Once trained, the U-Net can perform the full reconstruction from an intensity image stack in approximately 0.1 seconds on the used hardware. This rapid processing speed makes the in-situ tomographic reconstruction method even faster than in-situ QPI, where the final 2D phase computation typically takes several seconds.

6.5 EXPERIMENTAL VALIDATION

After the training using solely simulated intensity images, the 3D U-net was validated with real in-situ microscope images taken during 3D laser microprinting.

6.5.1 Image Capture

The images were taken using the same configuration that was used for simulations: the $25\times/\text{NA}0.8$ objective lens immersed in the IP-S photoresist, the Nanoscribe PPGT camera with a pixel size of $0.4\ \mu\text{m}$, and slicing distance of $0.3\ \mu\text{m}$ for printed structures. All structures were also hatched with a $0.2\ \mu\text{m}$ hatching distance, which is less than a pixel size and therefore does not influence light propagation at the scale of simulations. The structures were printed using a laser power of 20 mW and a scanning speed of 4 cm/s. Images were captured for each slice immediately after the printing of that particular slice was completed. The exposure time was set to 5 ms. As a result, in-situ bright-field imaging was almost instantaneous,

extending the overall printing time by only a fraction of seconds.

The process of capturing the image stack required for further reconstruction with the trained U-Net can be divided into several steps:

1. Find a substrate-photoresist interface (done automatically in the Nanoscribe PPGT).
2. Collect two background images before printing has started.
3. Print the sample, consisting of $k < 128$ slices, and capture one image with each printed slice. The total number of images captured is k , and the spacing between slices is $\Delta z = 0.3 \mu\text{m}$.
4. Capture $128 - k$ additional defocused images of the printed structure, capturing one image for each $\Delta z = 0.3 \mu\text{m}$ increment. These images correspond to the empty volume over the printed structure and technically do not provide any new information about light scattering. However, they are necessary to meet the input requirements of the designed network.
5. Capture additional 12 defocused images to account for any initial layers that may have been printed within the substrate. During the image processing procedure, the image stack is cropped to 128 images back again.

Thus, the obtained image stack comprised 140 intensity images. This total includes k images of printed slices and $140 - k$ "empty" defocused images. Capturing "empty" defocused images is necessary because the network requires input volumes of $128 \times 128 \times 128$. If the printed object contains fewer than 128 slices, additional slices with empty volume are required to meet this input specification.

6.5.2 Image Processing

The obtained microscopy image stack is further processed in order to be used with the trained 3D U-Net. This was also implemented in several steps:

1. The image stack was corrected for dark counts by subtracting the mean intensity value of an image taken without illumination.
2. The image stack was then normalized by dividing each image in the stack by the corresponding pixel values in the captured background image.
3. The stack was cropped in the xy -directions by applying the cross-correlation algorithms so that the structure was properly centered.
4. The stack was cropped in the z -direction by removing the first images without diffraction patterns, ensuring the first image starts with the first visible printed slice. Additional images at the end of the stack were removed

to ensure the final stack consisted of exactly 128 images.




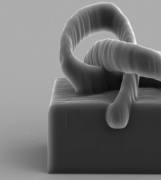


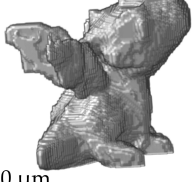
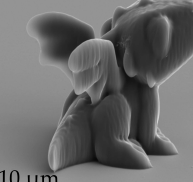

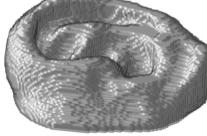
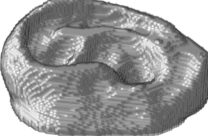
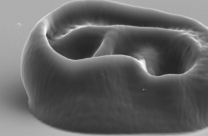
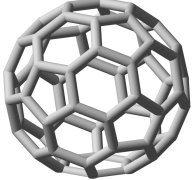
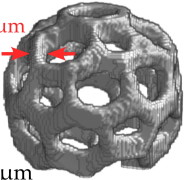
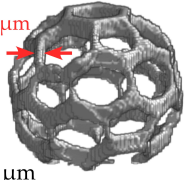
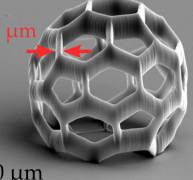
Thus, the final image stack consisted of $128 \times 128 \times 128$ volume and could be readily used for the end-to-end reconstruction using deep learning.

6.5.3 Experimental Reconstructions

The trained 3D U-Net was experimentally tested with four different 3D-printed samples. One of them, a trefoil knot sample, was directly used in the training dataset. The other three samples: a dragon, an ear, and a buckyball, were completely unseen by the network. [Figure 6.11](#) represents a comparison table between 3D STL models (first column), 3D reconstructions based on the purely simulated data (second column), and 3D experimental reconstructions (third column) from in-situ microscopic images taken during printing. Additionally, printed structures were developed in PGMEA for 20 min and were characterized ex situ by SEM (last column). It is worth mentioning that SEM images have much higher resolution than reconstructions from optical images and hence appear more detailed.

Analyzing the comparison table, all structures were reconstructed with high fidelity, showing only minimal artifacts on the scale of 1-2 pixels. This effect is particularly visible in the roughness of the cuboid structure located beneath the trefoil knots. Notably, the dragon and ear structures show almost no significant differences between experimental reconstructions, reconstructions from simulations, and SEM images. Several "island artifacts" observed in the experimental reconstruction of the dragon can be attributed to refractive index inhomogeneities within the photoresist volume, as was found by the OCT method and discussed in [section 4.2](#).

However, the trefoil knots appear generally thinner by 0.4-0.8 μm in the experimental reconstruction and SEM data compared to the reconstruction based on simulated data. This discrepancy is even more pronounced in the buckyball structure, where the rods were initially designed to have a thickness of 2.0 μm . In the in-situ experimental reconstruction, the measured rod thickness equals 1.2 μm and 1.3 μm in the SEM data. The effect of rod thinning is highlighted by red arrows in [Figure 6.11](#). This deviation likely stems from structural deformation and polymer shrinkage during printing. The observation of this effect nicely demonstrates the capability of the DL approach to accurately predict the in-situ shape deviations that might arise during printing, opening further possibilities to correct them within a single printing session.

Model	Model rendering	Reconstruction from simulation	Reconstruction from experiment	Measured electron micrograph
Trefoil knots				
Dragon*				
Ear*				
Buckyball*				

*Not included in the training dataset

Figure 6.11: Deep learning reconstructions of the binarized refractive index of 3D printed structures. Four models of trefoil knots, a dragon, an ear, and a buckyball were investigated. Only the trefoil knots model was used for training, while the other models were completely unseen. The results are arranged in a table, where the first column describes the model name, the second column consists of 3D rendering images from STL files that were used for 3D printing. The third column comprises DL prediction results from only intensity data simulated based on the STL files. The fourth column consists of DL reconstructions from in-situ microscopic images taken during laser printing. The last column corresponds to the ex-situ SEM image of developed structures. The experimental reconstructions are slightly cropped at the bottom due to printing within the substrate. The reconstructions from simulated data are cropped at the same locations to match the size of the experimental reconstructions for better comparison visibility. Adapted from [136].

6.6 STABILITY AND ROBUSTNESS

Despite obtaining accurate experimental results, the DL reconstruction approach is highly dependent on the simulation parameters used for training. Improper or inaccurate simulation parameters can degrade the quality of the final reconstructions. Among these key parameters are the absolute value of the photoresist refractive index n_{pr} and the refractive index difference between the polymerized and unpolymerized parts Δn .

The 3D U-Net was originally trained on datasets simulated using values of $n_{\text{IP-S}} = 1.483$ and $\Delta n_{\text{IP-S}} = 0.026$. However, using another photoresist, for example, IP-Dip with $n_{\text{IP-Dip}} = 1.518$ will result in different intensities distribution and hence the quality of reconstruction might deteriorate. Moreover, the Δn values might vary even within the single printing session as they depend on writing parameters, such as laser power and scanning velocity. This effect and the range of Δn variations were discussed in the context of in-situ OCT and in-situ QPI in [subsection 4.3.1](#) and [section 5.2](#), respectively. To evaluate the robustness and reconstruction ability of the trained 3D U-Net against the described variations, the network was tested with specifically simulated samples with different values of n_{pr} and Δn .

First, the trained 3D U-Net was tested against variations in n_{pr} . An exemplary trefoil knot model was used to calculate intensities simulated with $n_{\text{pr}} \in [n_{\text{IP-S}} - 0.05, n_{\text{IP-S}} + 0.05] = [1.433, 1.533]$. This range covers almost all known commercial photoresists commonly used for 3D laser microprinting, including IP-L, IP-Dip, and Ormocomp [39]. The refractive index difference was fixed at $\Delta n_{\text{IP-S}}$ in simulations. The results, which display metric values versus the absolute refractive index used for simulations, are shown in [Figure 6.12a](#). In [Figure 6.12b](#), several reconstructions from different values of refractive index n_{pr} are depicted.

Analyzing this figure, one can observe that the F1-score remains nearly constant, with only minor fluctuations on the scale of approximately 0.001. The reconstructions show barely noticeable differences across the various values of n_{pr} used for simulations. Thus, it can be concluded that the trained 3D U-Net demonstrates stability against these types of variations, and the absolute refractive index of the photoresist plays no significant role in the quality of reconstructions.

Furthermore, the same trefoil knot structure was simulated with varying values of Δn . The range of possible variations was estimated from the in-situ QPI refractive index measurements ([Figure 5.7](#)). In these measurements, the refractive index difference for the IP-S photoresist can vary from 0.024 to 0.026, and for the IP-Dip photoresist, the range is even broader, from 0.018 for the lowest laser power to 0.030 for the fully polymerized value. Therefore, the refractive index difference range for simulations was chosen to include all these values, $\Delta n \in [0.013, 0.040]$.

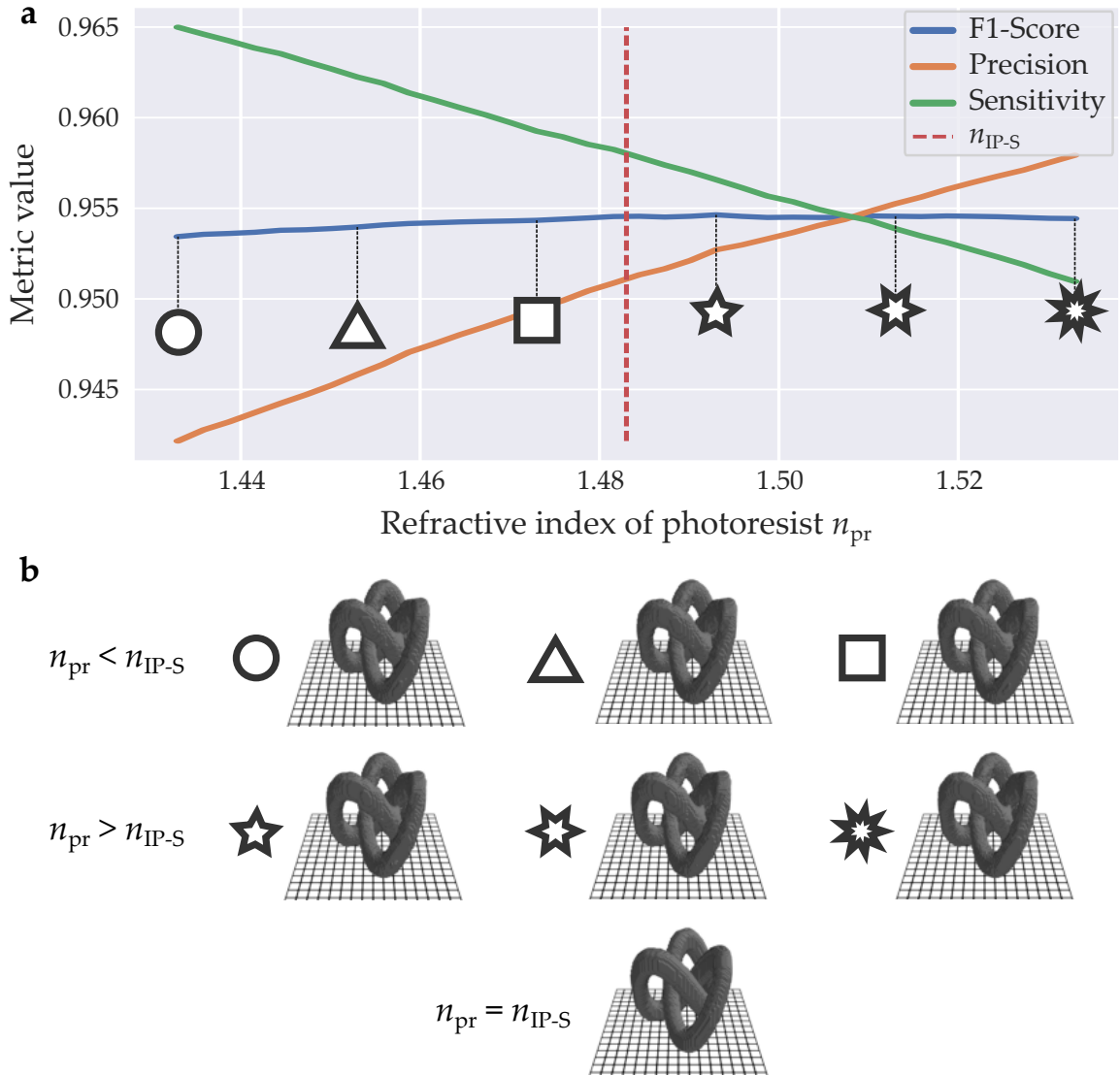


Figure 6.12: Robustness against variations in the refractive index of photoresist. **a** Metric values after reconstruction of an exemplary trefoil knot model simulated with different parameters of n_{pr} . The red dashed line corresponds to the value of $n_{pr} = n_{IP-S} = 1.483$ that was used for training. In simulations, the refractive index difference was fixed at $\Delta n_{IP-S} = 0.026$. **b** Example reconstruction results from certain values of n_{pr} . The lowest reconstruction corresponds to the ground truth model, where $n_{pr} = n_{IP-S}$. Adapted from [136].

Notably, for these simulations, the absolute value of the photoresist refractive index was fixed at $n_{IP-S} = 1.483$. The reconstruction results of the simulated structures with different values of Δn are presented in Figure 6.13.

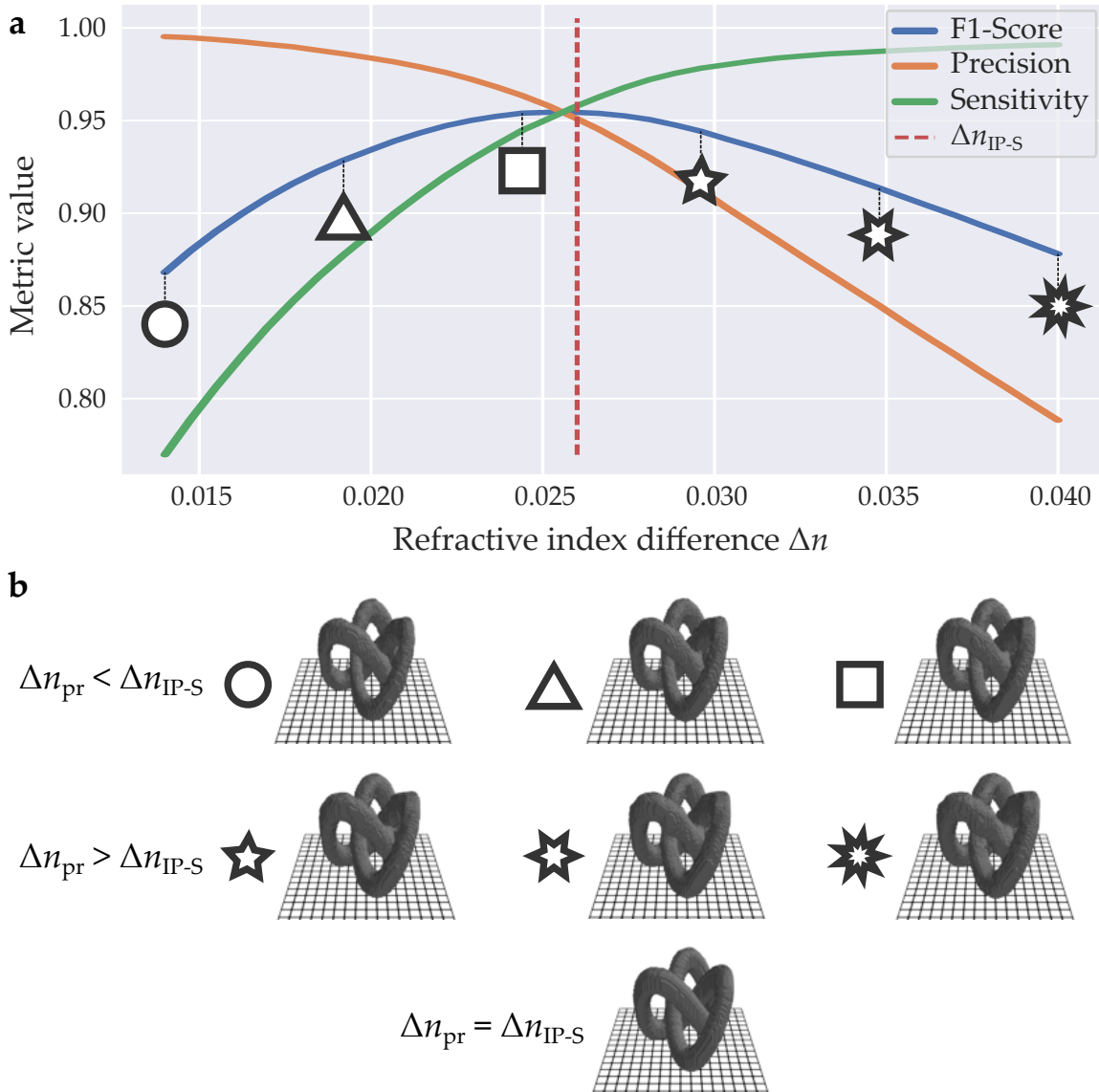


Figure 6.13: Robustness against variations in the refractive index difference. **a** Metric values after reconstruction of an exemplary trefoil knot model simulated with different parameters of Δn . The red dashed line corresponds to the value of $\Delta n_{IP-S} = 0.026$ that was used for training. In simulations, the photoresist refractive index was fixed at $n_{IP-S} = 1.483$. **b** Example reconstruction results from certain values of Δn . The lowest reconstruction corresponds to the ground truth model, where $\Delta n = \Delta n_{IP-S}$. Adapted from [136].

As seen from the metric plots, the resulting F1-score decreases more significantly, reaching a value of 0.87 for the extreme values of Δn . As indicated by the Precision and Sensitivity metrics, the network tends to under-predict volumes

if $\Delta n < \Delta n - \text{IP}_S$ and over-predict when $\Delta n > \Delta n_{\text{IP}_S}$. This effect of under- and over-prediction can also be observed in the reconstruction examples (Figure 6.13b). For instance, the reconstruction of structures with $\Delta n > \Delta n_{\text{IP}_S}$ appears thinner than the ground truth structure and, conversely, thicker for $\Delta n < \Delta n_{\text{IP}_S}$. Despite this effect, the reconstruction results are still considered feasible, with only a minor decrease in the F1-score for the standard range of commercial photoresists, where $0.02 \lesssim \Delta n \lesssim 0.03$.

Therefore, the DL method of in-situ reconstruction can be reliably applied to almost any type of commercial photoresist without the need for additional re-training. If a photoresist with significantly different values of n_{pr} is used, or if structures are fabricated with larger (or smaller) Δn , the network can be retrained to accommodate these specific refractive index ranges. However, other simulation parameters, such as the slicing distance, pixel size, voxel elongation, etc., cannot be changed since the resulting electric field and diffraction patterns will significantly differ from the simulated values. Therefore, if a different objective lens is used or the slicing distance is altered, the network must be retrained with the new values to ensure accurate reconstructions. Moreover, the z -shift related to optical misalignment inside the microscope, which introduces additional defocusing, can vary between printing setups. Accurately measuring this value and using it in the simulations (in Equation 6.9) is crucial for achieving proper reconstructions.

6.7 CONCLUSION

This chapter discussed the novel tomographic approach that reconstructs the 3D binarized refractive index from microscopic intensity images taken during 3D fabrication. This method does not require any additional scanning and utilizes only a single illumination direction. The experimental 3D reconstructions were achieved using a trained 3D U-Net model in less than one second. The single reconstruction voxel was $0.4 \times 0.4 \times 0.3 \mu\text{m}^3$. Consequently, the proposed in-situ reconstruction approach can be directly applied for real-time high-resolution monitoring of printed specimens.

The model was trained using hundreds of thousands of simulated 3D intensity datasets paired with corresponding binarized refractive index distributions. For accurate simulations, it is essential to replicate the exact printing settings and imaging configuration used in the real system, including imaging noise and non-sharp refractive index transition between polymerized and unpolymerized parts. Notably, the network was trained using a total volume of $128 \times 128 \times 128$ voxels. Scaling the network to accommodate larger volumes is possible but results in additional computational costs.

During the simulations, it was assumed that each printing voxel has a constant

height of 2.7 μm , matching the standard extension for the utilized objective lens. However, due to dose accumulation, some structures may experience a proximity effect, potentially extending the size of the printing voxels. Therefore, developing a more sophisticated forward model that includes the dose accumulation effect is a promising direction for future research to enhance the predictive accuracy of experimental results. Another potential advancement of this method involves quantitatively predicting printed refractive index values, which could significantly improve the fabrication of micro-optical elements and potentially implement the prediction of the optical performance of printed 3D micro-optics.

7

Chapter 7

CONCLUSIONS AND OUTLOOK

In the scope of this thesis, I developed and demonstrated methods for rapid and cost-effective in-situ imaging, monitoring, and reconstruction for 3D laser microprinting. Presented methods can effectively assess printed specimens during or immediately after the printing process bypassing development or any steps in between. All the methods were compared with established ex-situ imaging techniques, such as scanning electron microscopy and confocal microscopy, to validate the obtained in-situ imaging results. In the following, I provide a summary for each chapter and summarize the characteristics and parameters of the developed in-situ methods in one table.

In [chapter 2](#), I provided essential knowledge about the printing process and introduced threshold and accumulation models. I explained how dose accumulation can affect the size of the printing voxel, potentially introducing deviations to the final printed shape. I also discussed important properties of the photoresists used, such as the refractive index and the differences between polymerized and unpolymerized parts. Subsequently, I outlined the printing workflow and various strategies typically employed in 3D laser printing. Towards the end of the chapter, I presented the schematics of the printing setup that can also be utilized for in-situ bright-field microscopic imaging during printing. Finally, I introduced a z-shift that causes defocusing in all microscopic images taken, a factor that must be considered in bright-field transmission imaging.

In [chapter 3](#), I began by discussing common deviations between 3D models used as templates for printing and the resultant 3D printed samples, and described a typical method for addressing these: ex-situ shape optimization. I then introduced the concept and definition of in-situ imaging within the context of 3D laser microprinting, noting the requirement for non-invasive methods due to the photosensitivity of the photoresists used. This requirement narrowed the range of feasible imaging techniques. Subsequently, I explored possible solutions and reviewed previous attempts at in-situ imaging and reconstruction of 3D-printed samples. Among the methods discussed were optical coherence to-

mography (OCT), common bright-field microscopy, quantitative phase imaging (QPI), and optical diffraction tomography (ODT). For each method, I provided the fundamental theory and discussed its applicability to in-situ imaging and reconstruction.

In the following three chapters, I discussed the methods developed for in-situ imaging, monitoring, and reconstruction of 3D-printed samples. These methods were applied to determine the properties of printed specimens and to obtain 3D reconstructions.

In [chapter 4](#), I detailed the OCT setup developed specifically to mimic in-situ imaging configurations. The components of this setup can be seamlessly integrated into any custom-made printer. The OCT method provided crucial information about the quality of photoresists even before applying it to printed samples. For instance, the aged photoresist was found to contain numerous small blob particles associated with undissolved oligomers, whereas the fresh photoresist displayed significantly fewer of these particles. By applying OCT technology to study the planar surfaces of printed samples, I was able to measure the refractive index of the polymer and estimate the transition width between polymerized and unpolymerized parts. This observation was later utilized for precise modeling of the refractive index distribution in printed samples. Additionally, when exploring 3D geometries, I discovered that changes in the printing strategy led to variations in the 3D OCT signal. I attributed the variations in the 3D OCT signal to additional refractive index inhomogeneities that emerged during the printing process. This observation led to the conclusion that although OCT can detect these inhomogeneities, its effectiveness is limited. This indicates that OCT can only effectively reconstruct samples with such imperfections.

In [chapter 5](#), I presented the method of QPI that retrieves the in-situ optical path length (or phase difference) of printed samples. In-situ QPI was directly integrated into the Nanoscribe PPGT system. From the hardware perspective, only minor modifications were made to the illumination path of the setup. On the software side, a well-established algorithm that solves the transport-of-intensity equation was employed. This algorithm relies on defocused intensity images obtained during or after the 3D laser printing process. As a result, in-situ phase profiles were accurately measured, and topographies of various micro-optical elements were obtained. These in-situ topography maps were then compared with ex-situ spinning-disk confocal microscopy measurements, fully validating the developed in-situ QPI method. Moreover, the in-situ QPI method was employed for precise calculations of the polymer refractive index and relative shrinkage values. Dependencies of these values on printing laser power were defined for the two most commonly used photoresists: IP-Dip and IP-S.

In [chapter 6](#), I introduced a novel method for optical tomographic reconstruction

from common microscopic images captured during printing, using a trained deep learning network. This chapter began with an explanation of the inverse scattering problem in the context of the in-situ imaging configuration during 3D printing. Due to the complexity of this problem, it could only be effectively addressed using advanced computational algorithms, such as training a 3D deep learning model through an end-to-end approach. Given that this training required 3D ground truth dataset pairs, a simulation-based strategy was adopted, where the network was trained solely with simulated data. I detailed the full pipeline for generating 3D objects and creating realistic intensity datasets that were further used to train the network. After training the 3D U-Net architecture solely on these realistically simulated microscopic image datasets, the network was tested with experimental images. The obtained in-situ 3D reconstructions closely matched ex-situ SEM images and provided insights into the sample's deviations immediately after printing.

The main characteristics of the developed in-situ imaging methods are summarized in [Table 7.1](#).

	OCT	QPI	DLOR
Acquisition time	10 s	20 s*	< 1 s
Evaluation time	20 s	10 s	< 1 s
Illumination Mode	Reflection	Transmission	Transmission
Lateral resolution	2.2 μm	0.4 μm	0.4 μm
Axial resolution	2.7 μm	< 0.1 μm	0.3 μm
Additional setup	+	-	-
Signal type	3D back-scattering	2D phase	3D binarized refractive index
What can be reconstructed	Planar surfaces or 3D objects with imperfections	2.5D samples	All 3D-printed objects

*Can be reduced to <1 s when using non-native software.

Table 7.1: Comparison of the developed in-situ imaging methods. OCT method was described in [chapter 4](#), in-situ QPI was introduced in [chapter 5](#), and deep learning optical reconstruction (DLOR) was presented in [chapter 6](#).

OUTLOOK

Analyzing the developed in-situ imaging methods and the results obtained, I can conclude that all methods are fast, with the total acquisition and evaluation time being significantly less than the typical printing time. This opens up possibilities to use the developed methods for rapid on-the-fly shape estimation and optimization, potentially eliminating or significantly reducing the need for ex-situ methods in the future. However, all three methods are conceptually different, and therefore each could be suited for specific purposes and applications.

As demonstrated, in-situ OCT can accurately reconstruct 3D-printed objects with refractive index imperfections but struggles with the reconstruction of normal specimens that lack sufficient back-scattering properties. Therefore, this technology could be used to estimate the amount of such imperfections and correct them, aiming to minimize the OCT signal of the sample. Another potential application of this method is its use with photoresists that have additional scattering particles dissolved in them [143]. These additional scattering centers would significantly enhance the OCT contrast of the printed specimens. Furthermore, OCT technology could be effectively used to assess the purity of photoresists by evaluating undissolved particles in the volume.

As for in-situ QPI, although this method is used primarily for measuring 2.5D printed objects, it is fast, accurate, and can be easily integrated by anyone with a 3D laser printer simply by defining the illumination path. The axial resolution of QPI allows for the assessment of tiny shape deviations, enabling effective on-the-fly corrections. Additionally, performing QPI measurements after development and re-immersion in the same photoresist can provide valuable information about the shrinkage properties of various photoresists [120].

Perhaps the most promising in-situ imaging method is deep-learning optical reconstruction. This method requires only a trained neural network to effectively reconstruct any 3D-printed sample in situ. The primary obstacle to routine inspection using this method is the limited size of the possible reconstruction volume. The presented network is currently able to reconstruct volumes of approximately $50 \times 50 \times 40 \mu\text{m}^3$, which is relatively small compared to typical sample sizes, especially in the z -direction. Therefore, expanding the reconstruction volume, either by scaling the network or implementing a stitching procedure, is the main priority for future development. Another possible direction is the development of a more accurate prediction model that can reconstruct the refractive index quantitatively, rather than just providing binarized values. Additionally, recent studies in diffraction tomography have shown that by accounting for polarization, it is possible to reconstruct the 3D anisotropy distribution of birefringent specimens [144]. The implementation of this polarization-sensitive approach to the

developed reconstruction method is particularly attractive since printed samples exhibit birefringence attributed to induced stresses after polymerization [145].

Conceptually, this method relies solely on the accurate forward prediction, making it adaptable to other 3D printing modalities that involve fabrication from liquid transparent photoresists [146–148]. Although the primary focus of this work is in-situ imaging, I anticipate that the proposed tomographic approach could become a key component of neural lithography [149]. This could eventually allow for the prediction of ex-situ shapes by providing the neural network with knowledge about shrinkage during development. Such advancements could lead to accurate predictions of the final ex-situ shape and even the optical performance of printed micro-optics.

A

Appendix A

APPENDIX

A.1 GENERATION OF A BATCH GROUP CONSISTING OF 8 BATCHES

```
1:  $i \leftarrow 1$ 
2:  $N \leftarrow 8$ 
3:  $BatchGroupSize \leftarrow 80$ 
4:  $BatchGroupObjects \leftarrow \text{ZerosMatrix}(BatchGroupSize, 128, 128, 128, 1)$ 
5:  $BatchGroupIntensity \leftarrow \text{ZerosMatrix}(BatchGroupSize, 128, 128, 128, 1)$ 
6:  $Models \leftarrow$  Load  $N$  random models from ModelNet40 training set
7:  $Models \leftarrow \text{RandomlyRotateAndScale}(Models)$ 
8:  $ModelNetObjects \leftarrow \text{Voxelize}(Models)$ 
9: for  $j \leftarrow 1$  to  $BatchGroupSize$  do
10:   if  $\mathcal{U}(0, 1) > 0.5$  then
11:      $InputObject_{3D} \leftarrow ModelNetObjects(i \bmod N + 1)$ 
12:      $InputObject_{3D} \leftarrow \text{RandomlyResizeObject}(InputObject_{3D})$ 
13:      $i = i + 1$ 
14:   else
15:      $InputObject_{3D} \leftarrow \text{GenerateRandomTorusKnot}$ 
16:   end if
17:   if  $\mathcal{U}(0, 1) > 0.5$  then
18:      $InputObject_{3D} \leftarrow \text{RandomlyCropObject}(InputObject_{3D})$ 
19:   end if
20:   if  $\mathcal{U}(0, 1) > 0.5$  then
21:      $InputObject_{3D} \leftarrow \text{RandomPedestalUnderTheObject}(InputObject_{3D})$ 
22:   end if
23:    $(IntensityStack, OutputObject_{3D}) \leftarrow \text{ForwardModel}(InputObject_{3D})$ 
24:    $BatchGroupObjects(j) \leftarrow OutputObject_{3D}$ 
25:    $BatchGroupIntensity(j) \leftarrow IntensityStack + \text{Noise}$ 
26: end for
```

A.2 SIMULATION OF INTENSITIES USING MODIFIED MULTI-SLICE BEAM PROPAGATION MODEL (M-MSBPM)

```
1:  $n_{z\text{-voxels}} \leftarrow 9$ 
2:  $InputObject_{3D} \leftarrow$  binary object in  $128 \times 128 \times 128$  pixel matrix
3:  $InputObject_{3D} \leftarrow AssignRefractiveIndexDifference(InputObject_{3D})$ 
4:  $InputObject_{3D} \leftarrow RefractiveIndexSmearing(InputObject_{3D})$ 
5:  $InputField_{2D} \leftarrow \mathbf{1}_{128 \times 128}$   $\triangleright$  Create the incident field
6:  $FieldStack \leftarrow ZerosMatrix(128, 128, 128)$   $\triangleright$  z-, x- and y-direction
7:  $OutputObject_{3D} \leftarrow ZerosMatrix(128 + \frac{n_{z\text{-voxels}} - 1}{2}, 128, 128)$ 
8:  $PreviousSliceStack \leftarrow ZerosMatrix(n_{z\text{-voxels}}, 128, 128)$ 
9: for  $k \leftarrow 1$  to  $128$  do
10:    $Slice \leftarrow InputObject_{3D}(k)$ 
11:    $CurrentSliceStack \leftarrow$  Repeat  $Slice$   $n_{z\text{-voxels}}$  times in z-direction
12:    $DilatedSliceStack \leftarrow CurrentSliceStack || PreviousSliceStack$ 
13:    $InputField_{2D} \leftarrow ForwardPropagation(InputField_{2D}, DilatedSliceStack(1))$ 
14:    $Field_{2D} \leftarrow InputField_{2D}$ 
15:   for  $j \leftarrow 1$  to  $n_{z\text{-voxels}}$  do
16:      $Field_{2D} \leftarrow ForwardPropagation(Field_{2D}, DilatedSliceStack(j))$ 
17:   end for
18:    $Field_{2D} \leftarrow Defocus(Field_{2D}, \frac{n_{z\text{-voxels}} - 1}{2})$ 
19:    $FieldStack(k) \leftarrow Field_{2D}$ 
20:    $OutputObject_{3D}(k) \leftarrow DilatedSliceStack(1)$ 
21:    $PreviousSliceStack \leftarrow DilatedSliceStack$ 
22:    $PreviousSliceStack(n_{z\text{-voxels}}) \leftarrow \mathbf{0}_{128 \times 128}$ 
23: end for
24:  $DefocusedFieldStack \leftarrow Defocus(FieldStack, z_{\text{shift}})$ 
25:  $FilteredFieldStack \leftarrow NAfilter(DefocusedFieldStack)$ 
26:  $IntensityStack \leftarrow \text{abs}(FilteredFieldStack)^2$ 
27:  $OuputObject_{3D} \leftarrow$  Remove the first  $\frac{n_{z\text{-voxels}} - 1}{2}$  layers of  $OuputObject_{3D}$ 
28: Return ( $IntensityStack, OuputObject_{3D}$ )
```

Both [section A.1](#) and [section A.2](#) algorithms adapted from [136].

A.3 3D U-NET ARCHITECTURE

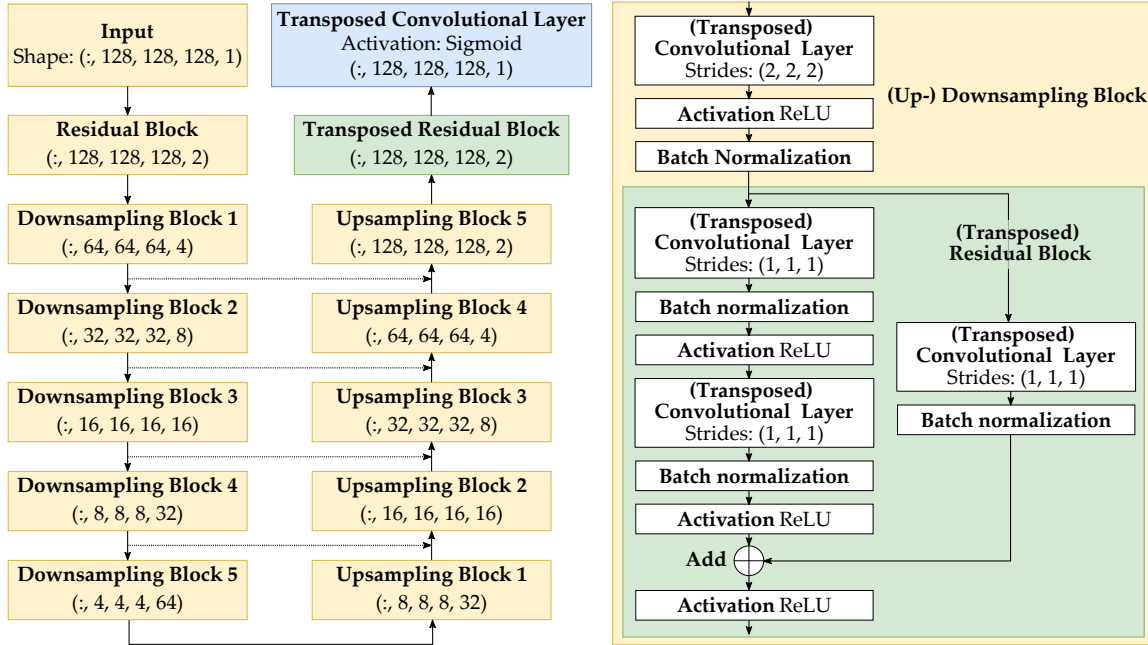


Figure A.1: The network consists of 5 downsampling blocks in the encoder and the same number of upsampling blocks in the decoder. Each downsampling block starts with a convolution of stride 2 to halve the size of the feature maps while doubling the number of filters. Each upsampling block starts with a transposed convolution of stride 2 to double the size of the feature maps while halving the number of filters. This is followed by batch normalization and activation, and then an additional residual block is added. The dashed lines between the encoder and the decoder represent skip connections. The feature maps from the encoder are concatenated with those from the decoder. Before the concatenated feature blocks reach the next decoder stage, they are passed through batch normalization and rectified linear unit (ReLU) activation. To limit the number of parameters, there is no bridge in this model. All convolutional layers have a kernel size of $3 \times 3 \times 3$, except for the last convolutional layer, which has a kernel size of $7 \times 7 \times 7$. Adapted from [136].

BIBLIOGRAPHY

- [1] M. Morrow, J. Waters, and E. Morris, “MRI for breast cancer screening, diagnosis, and treatment”, *The Lancet* **378**, 1804–1811 (2011) (cited on page 3).
- [2] M. Filippi, M. A. Rocca, O. Ciccarelli, N. De Stefano, N. Evangelou, L. Kappos, A. Rovira, J. Sastre-Garriga, M. Tintorè, J. L. Frederiksen, et al., “MRI criteria for the diagnosis of multiple sclerosis: MAGNIMS consensus guidelines”, *The Lancet Neurology* **15**, 292–303 (2016) (cited on page 3).
- [3] P. J. Withers, C. Bouman, S. Carmignato, V. Cnudde, D. Grimaldi, C. K. Hagen, E. Maire, M. Manley, A. Du Plessis, and S. R. Stock, “X-ray computed tomography”, *Nature Reviews Methods Primers* **1**, 18 (2021) (cited on page 3).
- [4] E. Tolosa, G. Wenning, and W. Poewe, “The diagnosis of Parkinson’s disease”, *The Lancet Neurology* **5**, 75–86 (2006) (cited on page 3).
- [5] E. G. Snyder, T. H. Watkins, P. A. Solomon, E. D. Thoma, R. W. Williams, G. S. Hagler, D. Shelow, D. A. Hindin, V. J. Kilaru, and P. W. Preuss, “The changing paradigm of air pollution monitoring”, *Environmental Science & Technology* **47**, 11369–11377 (2013) (cited on page 3).
- [6] L. Morawska, P. K. Thai, X. Liu, A. Asumadu-Sakyi, G. Ayoko, A. Bartonova, A. Bedini, F. Chai, B. Christensen, M. Dunbabin, et al., “Applications of low-cost sensing technologies for air quality monitoring and exposure assessment: How far have they gone?”, *Environment International* **116**, 286–299 (2018) (cited on page 3).
- [7] P. J. Vikesland, “Nanosensors for water quality monitoring”, *Nature Nanotechnology* **13**, 651–660 (2018) (cited on page 3).
- [8] D. Floreano and R. J. Wood, “Science, technology and the future of small autonomous drones”, *Nature* **521**, 460–466 (2015) (cited on page 3).
- [9] L. Mennel, J. Symonowicz, S. Wachter, D. K. Polyushkin, A. J. Molina-Mendoza, and T. Mueller, “Ultrafast machine vision with 2D material neural network image sensors”, *Nature* **579**, 62–66 (2020) (cited on page 3).

- [10] J. Rapp, J. Tachella, Y. Altmann, S. McLaughlin, and V. K. Goyal, "Advances in single-photon lidar for autonomous vehicles: Working principles, challenges, and recent advances", *IEEE Signal Processing Magazine* **37**, 62–71 (2020) (cited on page 3).
- [11] S. K. Everton, M. Hirsch, P. Stravroulakis, R. K. Leach, and A. T. Clare, "Review of in-situ process monitoring and in-situ metrology for metal additive manufacturing", *Materials & Design* **95**, 431–445 (2016) (cited on page 3).
- [12] J. N. Zalameda, E. R. Burke, R. A. Hafley, and C. S. Domack, "System and method for in-situ characterization and inspection of additive manufacturing deposits using transient infrared thermography", U.S. pat. 11027332B2 (2021) (cited on page 4).
- [13] Z. Mahmoudi, M. Sedighi, A. Jafari, S. Naghieh, E. Stefanek, M. Akbari, and H. Savoji, "In situ 3D bioprinting: A promising technique in advanced biofabrication strategies", *Bioprinting* **31**, e00260 (2023) (cited on page 4).
- [14] A. Urciuolo, I. Poli, L. Brandolino, P. Raffa, V. Scattolini, C. Laterza, G. G. Giobbe, E. Zambaiti, G. Selmin, M. Magnussen, et al., "Intravital three-dimensional bioprinting", *Nature Biomedical Engineering* **4**, 901–915 (2020) (cited on page 4).
- [15] T. Baldacchini, *Three-Dimensional Microfabrication Using Two-photon Polymerization: Fundamentals, Technology, and Applications* (William Andrew, 2015) (cited on pages 4, 8).
- [16] J. G. Fujimoto, C. Pitris, S. A. Boppart, and M. E. Brezinski, "Optical coherence tomography: an emerging technology for biomedical imaging and optical biopsy", *Neoplasia* **2**, 9–25 (2000) (cited on page 4).
- [17] Y. Park, C. Depeursinge, and G. Popescu, "Quantitative phase imaging in biomedicine", *Nature Photonics* **12**, 578–589 (2018) (cited on page 4).
- [18] J.-F. Xing, X.-Z. Dong, W.-Q. Chen, X.-M. Duan, N. Takeyasu, T. Tanaka, and S. Kawata, "Improving spatial resolution of two-photon microfabrication by using photoinitiator with high initiating efficiency", *Applied Physics Letters* **90** (2007) (cited on page 8).
- [19] J. H. Strickler and W. W. Webb, "Two-photon excitation in laser scanning fluorescence microscopy", in *CAN-AM Eastern'90*, Vol. 1398 (SPIE, 1991), pp. 107–118 (cited on page 8).
- [20] S. Maruo, O. Nakamura, and S. Kawata, "Three-dimensional microfabrication with two-photon-absorbed photopolymerization", *Optics Letters* **22**, 132–134 (1997) (cited on page 8).

-
- [21] T. Gissibl, S. Thiele, A. Herkommer, and H. Giessen, "Two-photon direct laser writing of ultracompact multi-lens objectives", *Nature Photonics* **10**, 554–560 (2016) (cited on page 8).
- [22] S. Thiele, K. Arzenbacher, T. Gissibl, H. Giessen, and A. M. Herkommer, "3D-printed eagle eye: Compound microlens system for foveated imaging", *Science Advances* **3**, e1602655 (2017) (cited on page 8).
- [23] B. Xu, W. Wei, P. Tang, J. Shao, X. Zhao, B. Chen, S. Dong, and C. Wu, "A Multi-foci Sparse-Aperture Metalens", *Advanced Science*, 2309648 (2024) (cited on page 8).
- [24] F. Seiboth, A. Kubec, A. Schropp, S. Niese, P. Gawlitza, J. Garrevoet, V. Galbierz, S. Achilles, S. Patjens, M. E. Stuckelberger, et al., "Rapid aberration correction for diffractive X-ray optics by additive manufacturing", *Optics Express* **30**, 31519–31529 (2022) (cited on page 8).
- [25] M. Jiang, S. Song, Y. Li, X. Zeng, L. Zhu, M. Zhang, S. Wang, X. Li, and Y. Cao, "3D high precision laser printing of a flat nanofocalizer for sub-wavelength light spot array", *Optics Letters* **46**, 356–359 (2021) (cited on page 8).
- [26] H. Wang, Y. Liu, Q. Ruan, H. Liu, R. J. Ng, Y. S. Tan, H. Wang, Y. Li, C.-W. Qiu, and J. K. Yang, "Off-Axis holography with uniform illumination via 3D printed diffractive optical elements", *Advanced Optical Materials* **7**, 1900068 (2019) (cited on page 8).
- [27] S. Tottori, L. Zhang, F. Qiu, K. K. Krawczyk, A. Franco-Obregón, and B. J. Nelson, "Magnetic helical micromachines: fabrication, controlled swimming, and cargo transport", *Advanced Materials* **24**, 811–816 (2012) (cited on page 8).
- [28] S. R. Dabbagh, M. R. Sarabi, M. T. Birtek, S. Seyfi, M. Sitti, and S. Tasoglu, "3D-printed microrobots from design to translation", *Nature Communications* **13**, 5875 (2022) (cited on page 8).
- [29] N. Lindenmann, G. Balthasar, D. Hillerkuss, R. Schmogrow, M. Jordan, J. Leuthold, W. Freude, and C. Koos, "Photonic wire bonding: a novel concept for chip-scale interconnects", *Optics Express* **20**, 17667–17677 (2012) (cited on page 8).
- [30] M. Blaicher, M. R. Billah, J. Kemal, T. Hoose, P. Marin-Palomo, A. Hofmann, Y. Kutuvantavida, C. Kieninger, P.-I. Dietrich, M. Laueremann, S. Wolf, U. Troppenz, M. Moehrle, F. Merget, S. Skacel, J. Witzens, S. Randel, W. Freude, and C. Koos, "Hybrid multi-chip assembly of optical communication engines by in situ 3D nano-lithography", *Light: Science & Applications* **9**, 71 (2020) (cited on page 8).

- [31] M. Hippler, K. Weißenbruch, K. Richler, E. D. Lemma, M. Nakahata, B. Richter, C. Barner-Kowollik, Y. Takashima, A. Harada, E. Blasco, et al., “Mechanical stimulation of single cells by reversible host-guest interactions in 3D microscaffolds”, *Science Advances* **6**, eabc2648 (2020) (cited on page 8).
- [32] F. Colombo, M. Taale, F. Taheri, M. Villiou, T. Debatin, G. Dulatahu, P. Kollenz, M. Schmidt, C. Schlagheck, J. Wittbrodt, et al., “Two-Photon Laser Printing to Mechanically Stimulate Multicellular Systems in 3D”, *Advanced Functional Materials*, 2303601 (2024) (cited on page 8).
- [33] T. Frenzel, “On 3D Chiral Mechanical Metamaterials”, PhD thesis (Karlsruher Institut für Technologie (KIT), 2020) (cited on pages 9, 16).
- [34] J. Fischer and M. Wegener, “Three-dimensional optical laser lithography beyond the diffraction limit”, *Laser & Photonics Reviews* **7**, 22–44 (2013) (cited on pages 9, 13).
- [35] P. Kiefer, V. Hahn, M. Nardi, L. Yang, E. Blasco, C. Barner-Kowollik, and M. Wegener, “Sensitive photoresists for rapid multiphoton 3D laser micro- and nanoprinting”, *Advanced Optical Materials* **8**, 2000895 (2020) (cited on pages 10, 12, 13).
- [36] S. Wang, Y. Yu, H. Liu, K. T. Lim, B. M. Srinivasan, Y. W. Zhang, and J. K. Yang, “Sub-10-nm suspended nano-web formation by direct laser writing”, *Nano Futures* **2**, 025006 (2018) (cited on page 12).
- [37] P. Somers, A. Münchinger, S. Maruo, C. Moser, X. Xu, and M. Wegener, “The physics of 3D printing with light”, *Nature Reviews Physics* **6**, 99–113 (2024) (cited on page 12).
- [38] S. Rodríguez, “Redefining microfabrication of high-precision optics: how two-photon grayscale lithography improves quality and throughput of printing microparts”, *PhotonicsViews* **17**, 36–39 (2020) (cited on pages 13, 77).
- [39] M. Schmid, D. Ludescher, and H. Giessen, “Optical properties of photoresists for femtosecond 3D printing: refractive index, extinction, luminescence-dose dependence, aging, heat treatment and comparison between 1-photon and 2-photon exposure”, *Optical Materials Express* **9**, 4564–4577 (2019) (cited on pages 13, 14, 21, 22, 50, 74, 75, 89, 103).
- [40] *IP-S Tables – Nanoscribe NanoGuide*, <https://support.nanoscribe.com/hc/en-gb/articles/360009156133-IP-S-Tables> (cited on pages 14, 74).
- [41] *IP-Dip Tables – Nanoscribe NanoGuide*, <https://support.nanoscribe.com/hc/en-gb/articles/360009156293-IP-Dip-Tables> (cited on pages 14, 74).

-
- [42] S. Dottermusch, D. Busko, M. Langenhorst, U. W. Paetzold, and B. S. Richards, “Exposure-dependent refractive index of Nanoscribe IP-Dip photoresist layers”, *Optics Letters* **44**, 29–32 (2019) (cited on pages [14](#), [50](#), [74](#), [75](#)).
- [43] J. Bauer, A. Guell Izard, Y. Zhang, T. Baldacchini, and L. Valdevit, “Programmable mechanical properties of two-photon polymerized materials: from nanowires to bulk”, *Advanced Materials Technologies* **4**, 1900146 (2019) (cited on page [14](#)).
- [44] C. F. Kern, “On the Hall effect in three-dimensional metamaterials”, PhD thesis (Karlsruher Institut für Technologie (KIT), 2019), 162 pp. (cited on page [14](#)).
- [45] Q. Sun, K. Ueno, and H. Misawa, “In situ investigation of the shrinkage of photopolymerized micro/nanostructures: the effect of the drying process”, *Optics Letters* **37**, 710–712 (2012) (cited on page [14](#)).
- [46] L. Jiang, W. Xiong, Y. Zhou, Y. Liu, X. Huang, D. Li, T. Baldacchini, L. Jiang, and Y. Lu, “Performance comparison of acrylic and thiol-acrylic resins in two-photon polymerization”, *Optics Express* **24**, 13687–13701 (2016) (cited on page [14](#)).
- [47] J. Bauer, A. G. Izard, Y. Zhang, T. Baldacchini, and L. Valdevit, “Thermal post-curing as an efficient strategy to eliminate process parameter sensitivity in the mechanical properties of two-photon polymerized materials”, *Optics Express* **28**, 20362–20371 (2020) (cited on pages [14](#), [57](#), [75](#)).
- [48] V. Hahn, T. Messer, N. M. Bojanowski, E. R. Curticean, I. Wacker, R. R. Schröder, E. Blasco, and M. Wegener, “Two-step absorption instead of two-photon absorption in 3D nanoprinting”, *Nature Photonics* **15**, 932–938 (2021) (cited on page [15](#)).
- [49] *Nanoscribe GmbH*, [nanoscribe.de](https://www.nanoscribe.de) (cited on page [16](#)).
- [50] E. Sedghamiz, M. Liu, and W. Wenzel, “Challenges and limits of mechanical stability in 3D direct laser writing”, *Nature Communications* **13**, 2115 (2022) (cited on page [20](#)).
- [51] S. Klein, P. Ruchka, T. Klumpp, N. Bartels, T. Steinle, and H. Giessen, “Effects of high-power laser radiation on polymers for 3D printing micro-optics”, *Optical Materials Express* **13**, 3653–3666 (2023) (cited on page [20](#)).
- [52] M. Ziemczonok, A. Kuś, P. Wasylczyk, and M. Kujawińska, “3D-printed biological cell phantom for testing 3D quantitative phase imaging systems”, *Scientific Reports* **9**, 1–9 (2019) (cited on page [21](#)).

- [53] S. K. Saha, J. S. Oakdale, J. A. Cuadra, C. Divin, J. Ye, J.-B. Forien, L. B. Bayu Aji, J. Biener, and W. L. Smith, "Radiopaque Resists for Two-Photon Lithography To Enable Submicron 3D Imaging of Polymer Parts via X-ray Computed Tomography", *ACS Applied Materials & Interfaces* **10**, 1164–1172 (2018) (cited on page 21).
- [54] F. Mayer, S. Richter, P. Hübner, T. Jabbour, and M. Wegener, "3D Fluorescence-Based Security Features by 3D Laser Lithography", *Advanced Materials Technologies* **2**, 1700212 (2017) (cited on page 21).
- [55] J. Weinacker, S. Kalt, P. Kiefer, P. Rietz, and M. Wegener, "On Iterative Pre-Compensation of 3D Laser-Printed Micro-Optical Components Using Confocal-Optical Microscopy", *Advanced Functional Materials*, 2309356 (2023) (cited on pages 21, 77).
- [56] K. R. Safronov, V. O. Bessonov, D. V. Akhremenkov, M. A. Sirotin, M. N. Romodina, E. V. Lyubin, I. V. Soboleva, and A. A. Fedyanin, "Miniature Otto Prism Coupler for Integrated Photonics", *Laser & Photonics Reviews*, 2100542 (2022) (cited on page 21).
- [57] R. Guo, S. Xiao, X. Zhai, J. Li, A. Xia, and W. Huang, "Micro lens fabrication by means of femtosecond two photon photopolymerization", *Optics Express* **14**, 810–816 (2006) (cited on page 21).
- [58] D. Huang, E. A. Swanson, C. P. Lin, J. S. Schuman, W. G. Stinson, W. Chang, M. R. Hee, T. Flotte, K. Gregory, C. A. Puliafito, et al., "Optical coherence tomography", *Science* **254**, 1178–1181 (1991) (cited on page 22).
- [59] J. G. Fujimoto, M. E. Brezinski, G. J. Tearney, S. A. Boppart, B. Bouma, M. R. Hee, J. F. Southern, and E. A. Swanson, "Optical biopsy and imaging using optical coherence tomography", *Nature Medicine* **1**, 970–972 (1995) (cited on page 22).
- [60] W. Drexler and J. G. Fujimoto, "State-of-the-art retinal optical coherence tomography", *Progress in Retinal and Eye Research* **27**, 45–88 (2008) (cited on page 22).
- [61] W. Drexler, U. Morgner, R. K. Ghanta, F. X. Kärtner, J. S. Schuman, and J. G. Fujimoto, "Ultrahigh-resolution ophthalmic optical coherence tomography", *Nature Medicine* **7**, 502–507 (2001) (cited on page 22).
- [62] G. J. Jaffe and J. Caprioli, "Optical coherence tomography to detect and manage retinal disease and glaucoma", *American Journal of Ophthalmology* **137**, 156–169 (2004) (cited on page 22).
- [63] B. Tan, Z. Hosseinaee, L. Han, O. Kralj, L. Sorbara, and K. Bizheva, "250 kHz, 1.5 μm resolution SD-OCT for in-vivo cellular imaging of the human cornea", *Biomedical Optics Express* **9**, 6569–6583 (2018) (cited on page 22).

-
- [64] S. Yang, L. Wang, Q. Chen, and M. Xu, "In situ process monitoring and automated multi-parameter evaluation using optical coherence tomography during extrusion-based bioprinting", *Additive Manufacturing* **47**, 102251 (2021) (cited on page 22).
- [65] J. W. Tashman, D. J. Shiwerski, B. Coffin, A. Ruesch, F. Lanni, J. M. Kainertorfer, and A. W. Feinberg, "In situ volumetric imaging and analysis of FRESH 3D bioprinted constructs using optical coherence tomography", *Biofabrication* **15**, 014102 (2022) (cited on page 22).
- [66] G. Guan, M. Hirsch, Z. H. Lu, D. T. Childs, S. J. Matcher, R. Goodridge, K. M. Groom, and A. T. Clare, "Evaluation of selective laser sintering processes by optical coherence tomography", *Materials & Design* **88**, 837–846 (2015) (cited on page 22).
- [67] M. R. Gardner, A. Lewis, J. Park, A. B. McElroy, A. D. Estrada, S. Fish, J. J. Beaman Jr, and T. E. Milner, "In situ process monitoring in selective laser sintering using optical coherence tomography", *Optical Engineering* **57**, 041407 (2018) (cited on page 22).
- [68] P. J. DePond, G. Guss, S. Ly, N. P. Calta, D. Deane, S. Khairallah, and M. J. Matthews, "In situ measurements of layer roughness during laser powder bed fusion additive manufacturing using low coherence scanning interferometry", *Materials & Design* **154**, 347–359 (2018) (cited on page 22).
- [69] B. Dong and B. Pan, "Visualizing curing process inside polymers", *Applied Physics Letters* **116**, 054103 (2020) (cited on page 22).
- [70] W. Drexler and J. G. Fujimoto, *Optical Coherence Tomography: Technology and Applications* (Springer, 2015) (cited on pages 23, 25, 43).
- [71] M. Muller, *Introduction to confocal fluorescence microscopy*, Vol. 69 (SPIE press, 2006) (cited on page 23).
- [72] J. A. Izatt, M. R. Hee, G. M. Owen, E. A. Swanson, and J. G. Fujimoto, "Optical coherence microscopy in scattering media", *Optics Letters* **19**, 590–592 (1994) (cited on page 23).
- [73] S. Zheng, Y. Bai, Z. Xu, P. Liu, and G. Ni, "Optical coherence tomography for three-dimensional imaging in the biomedical field: a review", *Frontiers in Physics* **9**, 744346 (2021) (cited on page 24).
- [74] G. Popescu, *Quantitative Phase Imaging of Cells and Tissues* (McGraw-Hill, 2011) (cited on pages 29, 31, 32).
- [75] J. W. Goodman, *Introduction to Fourier optics* (Roberts and Company publishers, 2005) (cited on pages 29, 84).

- [76] Y. E. Begantsova, R. Zvagelsky, E. V. Baranov, D. A. Chubich, Y. V. Chechet, D. A. Kolymagin, A. V. Pisarenko, A. G. Vitukhnovsky, and S. A. Chesnokov, "Imidazole-containing photoinitiators for fabrication of sub-micron structures by 3D two-photon polymerization", *European Polymer Journal* **145**, 110209 (2021) (cited on page 29).
- [77] X. Y. Lee, S. K. Saha, S. Sarkar, and B. Giera, "Automated detection of part quality during two-photon lithography via deep learning", *Additive Manufacturing* **36**, 101444 (2020) (cited on page 30).
- [78] F. Zernike, "How I discovered phase contrast", *Science* **121**, 345–349 (1955) (cited on pages 30, 31).
- [79] D. Gabor, "Holography, 1948-1971", *Science* **177**, 299–313 (1972) (cited on pages 30, 31).
- [80] E. N. Leith and J. Upatnieks, "Reconstructed wavefronts and communication theory", *Journal of the Optical Society of America* **52**, 1123–1130 (1962) (cited on page 31).
- [81] E. Cuche, F. Bevilacqua, and C. Depeursinge, "Digital holography for quantitative phase-contrast imaging", *Optics Letters* **24**, 291–293 (1999) (cited on page 31).
- [82] X. Porte, N. U. Dinc, J. Moughames, G. Panusa, C. Juliano, M. Kadic, C. Moser, D. Brunner, and D. Psaltis, "Direct (3+1)D laser writing of graded-index optical elements", *Optica* **8**, 1281–1287 (2021) (cited on page 33).
- [83] G. Lai and T. Yatagai, "Generalized phase-shifting interferometry", *Journal of the Optical Society of America A* **8**, 822–827 (1991) (cited on page 33).
- [84] D. Hogenboom, C. A. DiMarzio, T. J. Gaudette, A. J. Devaney, and S. C. Lindberg, "Three-dimensional images generated by quadrature interferometry", *Optics Letters* **23**, 783–785 (1998) (cited on page 33).
- [85] G. Popescu, L. P. Deflores, J. C. Vaughan, K. Badizadegan, H. Iwai, R. R. Dasari, and M. S. Feld, "Fourier phase microscopy for investigation of biological structures and dynamics", *Optics Letters* **29**, 2503–2505 (2004) (cited on page 33).
- [86] C. Zuo, J. Li, J. Sun, Y. Fan, J. Zhang, L. Lu, R. Zhang, B. Wang, L. Huang, and Q. Chen, "Transport of intensity equation: a tutorial", *Optics and Lasers in Engineering* **135**, 106187 (2020) (cited on pages 33, 34, 66, 67, 70).
- [87] M. R. Teague, "Irradiance moments: their propagation and use for unique retrieval of phase", *Journal of the Optical Society of America* **72**, 1199–1209 (1982) (cited on page 33).
- [88] N. Streibl, "Phase imaging by the transport equation of intensity", *Optics Communications* **49**, 6–10 (1984) (cited on page 33).

-
- [89] M. R. Teague, "Deterministic phase retrieval: a Green's function solution", *Journal of the Optical Society of America* **73**, 1434–1441 (1983) (cited on page 33).
- [90] T. E. Gureyev and K. A. Nugent, "Rapid quantitative phase imaging using the transport of intensity equation", *Optics Communications* **133**, 339–346 (1997) (cited on page 34).
- [91] Z. Jingshan, R. A. Claus, J. Dauwels, L. Tian, and L. Waller, "Transport of intensity phase imaging by intensity spectrum fitting of exponentially spaced defocus planes", *Optics Express* **22**, 10661–10674 (2014) (cited on page 35).
- [92] K. G. Phillips, C. R. Velasco, J. Li, A. Kolatkar, M. Lutten, K. Bethel, B. Duggan, P. Kuhn, and O. J. McCarty, "Optical quantification of cellular mass, volume, and density of circulating tumor cells identified in an ovarian cancer patient", *Frontiers in Oncology* **2**, 72 (2012) (cited on page 35).
- [93] C. Zuo, Q. Chen, W. Qu, and A. Asundi, "High-speed transport-of-intensity phase microscopy with an electrically tunable lens", *Optics Express* **21**, 24060–24075 (2013) (cited on page 35).
- [94] C. Zuo, Q. Chen, H. Li, W. Qu, and A. Asundi, "Boundary-artifact-free phase retrieval with the transport of intensity equation II: applications to microlens characterization", *Optics Express* **22**, 18310–18324 (2014) (cited on page 35).
- [95] M. H. Jenkins, J. M. Long, and T. K. Gaylord, "Multifilter phase imaging with partially coherent light", *Applied Optics* **53**, D29–D39 (2014) (cited on page 35).
- [96] E. Wolf, "Three-dimensional structure determination of semi-transparent objects from holographic data", *Optics Communications* **1**, 153–156 (1969) (cited on page 35).
- [97] U. S. Kamilov, I. N. Papadopoulos, M. H. Shoreh, A. Goy, C. Vonesch, M. Unser, and D. Psaltis, "Optical tomographic image reconstruction based on beam propagation and sparse regularization", *IEEE Transactions on Computational Imaging* **2**, 59–70 (2016) (cited on pages 35, 91).
- [98] D. Jin, R. Zhou, Z. Yaqoob, and P. T. So, "Tomographic phase microscopy: principles and applications in bioimaging", *Journal of the Optical Society of America B* **34**, B64–B77 (2017) (cited on page 35).
- [99] Y. Sung, N. Lue, B. Hamza, J. Martel, D. Irimia, R. R. Dasari, W. Choi, Z. Yaqoob, and P. So, "Three-dimensional holographic refractive-index measurement of continuously flowing cells in a microfluidic channel", *Physical Review Applied* **1**, 014002 (2014) (cited on page 36).

- [100] J. Yoon, K. Kim, H. Park, C. Choi, S. Jang, and Y. Park, "Label-free characterization of white blood cells by measuring 3D refractive index maps", *Biomedical Optics Express* **6**, 3865–3875 (2015) (cited on page 36).
- [101] Y. He, Q. Shao, S.-C. Chen, and R. Zhou, "Characterization of two-photon photopolymerization fabrication using high-speed optical diffraction tomography", *Additive Manufacturing* **60**, 103293 (2022) (cited on pages 36, 37).
- [102] J. Lim, K. Lee, K. H. Jin, S. Shin, S. Lee, Y. Park, and J. C. Ye, "Comparative study of iterative reconstruction algorithms for missing cone problems in optical diffraction tomography", *Optics Express* **23**, 16933–16948 (2015) (cited on page 36).
- [103] M. Ziemczonok, A. Kuś, and M. Kujawińska, "Optical diffraction tomography meets metrology—measurement accuracy on cellular and subcellular level", *Measurement* **195**, 111106 (2022) (cited on page 36).
- [104] S. Bianchi, F. Brasili, F. Saglimbeni, B. Cortese, and R. Di Leonardo, "Optical diffraction tomography of 3D microstructures using a low coherence source", *Optics Express* **30**, 22321–22332 (2022) (cited on page 36).
- [105] R. Zvagelsky, F. Mayer, D. Beutel, C. Rockstuhl, G. Gomard, and M. Wegener, "Towards in-situ diagnostics of multi-photon 3D laser printing using optical coherence tomography", *Light: Advanced Manufacturing* **3**, 466–480 (2022) (cited on pages 41, 45–52, 54–56, 58–63).
- [106] D. Hillmann, T. Bonin, C. Lühns, G. Franke, M. Hagen-Eggert, P. Koch, and G. Hüttmann, "Common approach for compensation of axial motion artifacts in swept-source OCT and dispersion in Fourier-domain OCT", *Optics Express* **20**, 6761–6776 (2012) (cited on page 43).
- [107] M. Wojtkowski, V. J. Srinivasan, T. H. Ko, J. G. Fujimoto, A. Kowalczyk, and J. S. Duker, "Ultrahigh-resolution, high-speed, Fourier domain optical coherence tomography and methods for dispersion compensation", *Optics Express* **12**, 2404–2422 (2004) (cited on page 44).
- [108] A. Agrawal, T. J. Pfefer, P. D. Woolliams, P. H. Tomlins, and G. Nehmetallah, "Methods to assess sensitivity of optical coherence tomography systems", *Biomedical Optics Express* **8**, 902–917 (2017) (cited on page 45).
- [109] I. H. Malitson, "Interspecimen comparison of the refractive index of fused silica", *Journal of the Optical Society of America* **55**, 1205–1209 (1965) (cited on page 46).
- [110] J. B. Mueller, J. Fischer, Y. J. Mange, T. Nann, and M. Wegener, "In-situ local temperature measurement during three-dimensional direct laser writing", *Applied Physics Letters* **103**, 123107 (2013) (cited on page 46).

-
- [111] M. Born and E. Wolf, *Principles of optics: electromagnetic theory of propagation, interference and diffraction of light* (Elsevier, 2013) (cited on pages 52, 59).
- [112] *jreftran - A layered thin film transmission and reflection coefficient calculator*, <https://www.mathworks.com/matlabcentral/fileexchange/50923-jreftran-a-layered-thin-film/-transmission-and-reflection-coefficient/-calculator> (cited on page 53).
- [113] *3D-benchy*, <https://www.3dbenchy.com/> (cited on page 62).
- [114] C. Bellair, C. Curl, B. Allman, P. Harris, A. Roberts, L. Delbridge, and K. Nugent, “Quantitative phase amplitude microscopy IV: imaging thick specimens”, *Journal of Microscopy* **214**, 62–69 (2004) (cited on page 67).
- [115] M. Beleggia, M. Schofield, V. Volkov, and Y. Zhu, “On the transport of intensity technique for phase retrieval”, *Ultramicroscopy* **102**, 37–49 (2004) (cited on page 67).
- [116] L. Waller, L. Tian, and G. Barbastathis, “Transport of intensity phase-amplitude imaging with higher order intensity derivatives”, *Optics Express* **18**, 12552–12561 (2010) (cited on page 68).
- [117] M. Soto and E. Acosta, “Improved phase imaging from intensity measurements in multiple planes”, *Applied Optics* **46**, 7978–7981 (2007) (cited on page 68).
- [118] C. Zuo, Q. Chen, Y. Yu, and A. Asundi, “Transport-of-intensity phase imaging using Savitzky-Golay differentiation filter-theory and applications”, *Optics Express* **21**, 5346–5362 (2013) (cited on pages 68, 69).
- [119] R. Zvagelsky, P. Kiefer, J. Weinacker, and M. Wegener, “In-situ Quantitative Phase Imaging during Multi-photon Laser Printing”, *ACS Photonics* **10**, 2901–2908 (2023) (cited on pages 72–74, 76, 78, 79).
- [120] S. Braun, R. Zvagelsky, T. Messer, M. Holsten, P. Kollenz, O. Tverskoy, A. De la Cruz Garcia, C. Selhuber-Unkel, M. Mastalerz, F. Rominger, J. Freudenberg, M. Wegener, and U. Bunz, “Vinylcyclopropane Polymerization by 3D Laser Nanoprinting: Low Shrinkage Resins with Low Cytotoxicity”, *Macromolecules* (under review) (cited on pages 75, 112).
- [121] P. Kiefer, V. Hahn, S. Kalt, Q. Sun, Y. M. Eggeler, and M. Wegener, “A multi-photon (7×7)-focus 3D laser printer based on a 3D-printed diffractive optical element and a 3D-printed multi-lens array”, *Light: Advanced Manufacturing* **4**, 28–41 (2024) (cited on pages 77, 78).
- [122] V. Hahn, P. Kiefer, T. Frenzel, J. Qu, E. Blasco, C. Barner-Kowollik, and M. Wegener, “Rapid assembly of small materials building blocks (voxels) into large functional 3D metamaterials”, *Advanced Functional Materials* **30**, 1907795 (2020) (cited on pages 78, 79).

- [123] F. Seiboth, M. Kahnt, M. Lyubomirskiy, M. Seyrich, F. Wittwer, T. Ullsperger, S. Nolte, D. Batey, C. Rau, and C. G. Schroer, "Refractive hard x-ray vortex phase plates", *Optics Letters* **44**, 4622–4625 (2019) (cited on page 80).
- [124] M. Lyubomirskiy, F. Wittwer, M. Kahnt, F. Koch, A. Kubec, K. V. Falch, J. Garrevoet, M. Seyrich, C. David, and C. G. Schroer, "Multi-beam X-ray ptychography using coded probes for rapid non-destructive high resolution imaging of extended samples", *Scientific Reports* **12**, 6203 (2022) (cited on page 80).
- [125] T. Li, M. Kahnt, T. L. Sheppard, R. Yang, K. V. Falch, R. Zvagelsky, P. Villanueva-Perez, M. Wegener, and M. Lyubomirskiy, "X-ray multibeam ptychography at up to 20 keV: nano-lithography enhances X-ray nano-imaging", *Advanced Science*, 2310075 (2024) (cited on page 80).
- [126] C. Zuo, Q. Chen, and A. Asundi, "Boundary-artifact-free phase retrieval with the transport of intensity equation: fast solution with use of discrete cosine transform", *Optics Express* **22**, 9220–9244 (2014) (cited on page 81).
- [127] J. Zhang, Q. Chen, J. Sun, L. Tian, and C. Zuo, "On a universal solution to the transport-of-intensity equation", *Optics Letters* **45**, 3649–3652 (2020) (cited on page 81).
- [128] L. Tian and L. Waller, "3D intensity and phase imaging from light field measurements in an LED array microscope", *Optica* **2**, 104–111 (2015) (cited on page 84).
- [129] O. Ronneberger, P. Fischer, and T. Brox, "U-net: Convolutional networks for biomedical image segmentation", in *Medical image computing and computer-assisted intervention–MICCAI 2015: 18th international conference, Munich, Germany, October 5–9, 2015, proceedings, part III* 18 (Springer, 2015), pp. 234–241 (cited on page 86).
- [130] Ö. Çiçek, A. Abdulkadir, S. S. Lienkamp, T. Brox, and O. Ronneberger, "3D U-Net: learning dense volumetric segmentation from sparse annotation", in *Medical Image Computing and Computer-Assisted Intervention–MICCAI 2016: 19th International Conference, Athens, Greece, October 17–21, 2016, Proceedings, Part II* 19 (Springer, 2016), pp. 424–432 (cited on page 86).
- [131] N. Siddique, S. Paheding, C. P. Elkin, and V. Devabhaktuni, "U-net and its variants for medical image segmentation: A review of theory and applications", *IEEE Access* **9**, 82031–82057 (2021) (cited on page 86).
- [132] O. Furat, M. Wang, M. Neumann, L. Petrich, M. Weber, C. E. Krill III, and V. Schmidt, "Machine learning techniques for the segmentation of tomographic image data of functional materials", *Frontiers in Materials* **6**, 145 (2019) (cited on page 86).

-
- [133] Y. Kasten, D. Doktofsky, and I. Kovler, “End-to-end convolutional neural network for 3D reconstruction of knee bones from bi-planar X-ray images”, in Machine Learning for Medical Image Reconstruction: Third International Workshop, MLMIR 2020, Held in Conjunction with MICCAI 2020, Lima, Peru, October 8, 2020, Proceedings 3 (Springer, 2020), pp. 123–133 (cited on page 86).
- [134] L. Wu, S. Yoo, A. F. Suzana, T. A. Assefa, J. Diao, R. J. Harder, W. Cha, and I. K. Robinson, “Three-dimensional coherent x-ray diffraction imaging via deep convolutional neural networks”, npj Computational Materials 7, 175 (2021) (cited on page 86).
- [135] C. Dehner, G. Zahnd, V. Ntziachristos, and D. Jüstel, “A deep neural network for real-time optoacoustic image reconstruction with adjustable speed of sound”, Nature Machine Intelligence 5, 1130–1141 (2023) (cited on page 86).
- [136] R. Zvagelsky, T. Alletzhaeusser, S. Kalt, and M. Wegener, “In-situ optical tomographic reconstruction during 3D laser microprinting using deep learning”, Nature Communications (under review) (cited on pages 86, 88–90, 92, 94, 96–98, 102, 104, 105, 116, 117).
- [137] Z. Wu, S. Song, A. Khosla, F. Yu, L. Zhang, X. Tang, and J. Xiao, “3d shapenets: A deep representation for volumetric shapes”, in Proceedings of the IEEE conference on computer vision and pattern recognition (2015), pp. 1912–1920 (cited on page 87).
- [138] S. Chowdhury, M. Chen, R. Eckert, D. Ren, F. Wu, N. Repina, and L. Waller, “High-resolution 3D refractive index microscopy of multiple-scattering samples from intensity images”, Optica 6, 1211–1219 (2019) (cited on page 91).
- [139] K. C. Zhou and R. Horstmeyer, “Diffraction tomography with a deep image prior”, Optics Express 28, 12872–12896 (2020) (cited on page 91).
- [140] *TensorFlow*, <https://www.tensorflow.org/> (cited on page 93).
- [141] H. Schopmans, P. Reiser, and P. Friederich, “Neural networks trained on synthetically generated crystals can extract structural information from ICSD powder X-ray diffractograms”, Digital Discovery 2, 1414–1424 (2023) (cited on page 95).
- [142] D. P. Kingma and J. Ba, “Adam: A method for stochastic optimization”, arXiv preprint arXiv:1412.6980 (2014) (cited on page 95).
- [143] A. C. Lamont, M. A. Restaino, A. T. Alsharhan, Z. Liu, D. X. Hammer, R. D. Sochol, and A. Agrawal, “Direct laser writing of a titanium dioxide-laden retinal cone phantom for adaptive optics-optical coherence tomography”, Optical Materials Express 10, 2757–2767 (2020) (cited on page 112).

- [144] S. Song, J. Kim, T. Moon, B. Seong, W. Kim, C.-H. Yoo, J.-K. Choi, and C. Joo, “Polarization-sensitive intensity diffraction tomography”, *Light: Science & Applications* **12**, 124 (2023) (cited on page 112).
- [145] M. Schmid and H. Giessen, “Stress-induced birefringence in 3D direct laser written micro-optics”, *Optics Letters* **47**, 5789–5792 (2022) (cited on page 113).
- [146] J. R. Tumbleston, D. Shirvanyants, N. Ermoshkin, R. Januszewicz, A. R. Johnson, D. Kelly, K. Chen, R. Pinschmidt, J. P. Rolland, A. Ermoshkin, et al., “Continuous liquid interface production of 3D objects”, *Science* **347**, 1349–1352 (2015) (cited on page 113).
- [147] V. Hahn, P. Rietz, F. Hermann, P. Müller, C. Barner-Kowollik, T. Schlöder, W. Wenzel, E. Blasco, and M. Wegener, “Light-sheet 3D microprinting via two-colour two-step absorption”, *Nature Photonics* **16**, 784–791 (2022) (cited on page 113).
- [148] A. Orth, D. Webber, Y. Zhang, K. L. Sampson, H. W. de Haan, T. Lacelle, R. Lam, D. Solis, S. Dayanandan, T. Waddell, et al., “Deconvolution volumetric additive manufacturing”, *Nature Communications* **14**, 4412 (2023) (cited on page 113).
- [149] C. Zheng, G. Zhao, and P. So, “Close the Design-to-Manufacturing Gap in Computational Optics with a ‘Real2Sim’ Learned Two-Photon Neural Lithography Simulator”, in *SIGGRAPH Asia 2023 Conference Papers* (2023), pp. 1–9 (cited on page 113).

ACKNOWLEDGMENTS

The completion of this doctoral thesis marks a significant chapter in my life, one filled with both challenges and achievements. Throughout this journey, I have been fortunate to receive support, guidance, and encouragement from many wonderful people. I would like to take this opportunity to thank everyone who has helped me during my doctoral studies.

First and foremost, I would like to thank Prof. Dr. Martin Wegener, who provided me with the opportunity to complete this doctoral thesis. His supervision and support were invaluable at every stage of my research.

I extend special thanks to Frederik Mayer, who helped me in the onboarding process and provided indispensable support at the beginning of my doctoral journey. He assisted me with everything from relocation formalities and apartment searches to assistance with the design, simulation, assembly, and experiments of the in-situ OCT setup.

Towards the end of my doctoral thesis, Tim Alletzhäusser significantly contributed to our deep learning project. His substantial programming work on the in-situ deep learning reconstruction approach has brought us the positive results we were hoping for. It was a pleasure to mentor him during his Master's degree, and I am confident that Tim will achieve new heights in his further research. I also appreciate his proofreading of the deep learning section of this work.

I also acknowledge Pascal Kiefer for his help in proofreading this thesis. Additionally, I am grateful for his assistance in measuring the printed structures using a spinning-disk confocal microscope and for providing his DOE design for in-situ QPI. I also thank Sebastian Kalt and Tobias Messer, who always made time to image my samples using SEM.

During my Ph.D. studies, I was part of two graduate schools: the Karlsruhe School of Optics and Photonics (KSOP) and the Cluster of Excellence 3D Matter Made to Order (3DMM2O). Their summer schools, seminars, and conferences facilitated networking and enhanced my knowledge of optics and photonics.

I also want to thank Guillaume Gomard from Zeiss AG, who offered a great collaboration, provided valuable advice, and initiated our joint OCT patent. I also acknowledge Prof. Dr. Pascal Friederich from the Institute of Nanotechnology at

ACKNOWLEDGMENTS

KIT for advice and assistance in machine learning approaches.

Moreover, I received invaluable assistance from the secretary of the Institute of Applied Physics at KIT: Petra Bauer, Ursula Mösle, and Gloria Zanda. I am especially grateful to Petra Bauer for handling all my administrative issues. I also acknowledge Johann Westhauser for his help with purchase orders and technical assistance in the lab, and Michael Hippe for his support of all computer and IT-related problems.

I would also like to express my gratitude to the other members of our group with whom I had the pleasure of collaborating over the past three and a half years. I greatly value the friendly atmosphere and I always knew that I could find someone to discuss any of my problems.

Finally, I express my infinite gratitude to my family and my girlfriend Polina. Their unwavering support and love were a constant source of strength and motivation.

